Journal of Engineering

Structural Integrity: Ideas, Innovations, and Initiatives

Lead Guest Editor: Karthikeyan Sathasivam
Guest Editors: A. Prabhakarn and Mayakrishnan Gopiraman

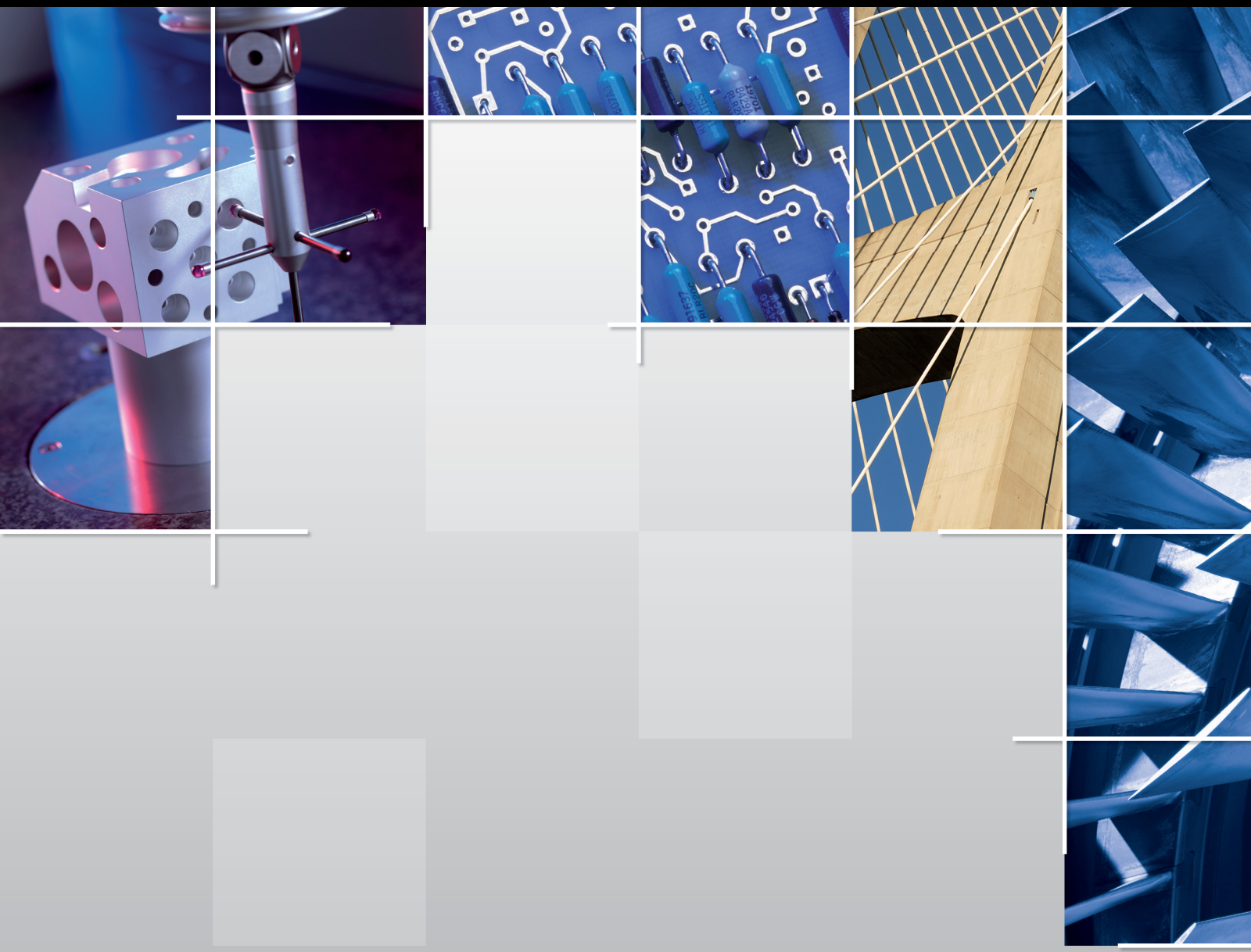

Structural Integrity: Ideas, Innovations, and Initiatives

Journal of Engineering

Structural Integrity: Ideas, Innovations, and Initiatives

Lead Guest Editor: Karthikeyan Sathasivam
Guest Editors: A. Prabhakarn and Mayakrishnan Gopiraman

Industrial Engineering

Mechanical Engineering

Contents

Hindawi
Journal of Engineering
Volume 2023, Article ID 5274325, 4 pages
https://doi.org/10.1155/2023/5274325

Research Article

Emissions and Performance of Diesel Engines Correlated with Biodiesel Properties

Raviteja Surakasi,[1] **Yenda Srinivasa Rao**,[2] **Sd. Abdul Kalam**,[3] **and Naziya Begum**[4]

[1]*Department of Mechanical Engineering, Lendi Institute of Engineering and Technology, Jonnada, Vizianagaram, Andhra Pradesh 535005, India*
[2]*Department of Mechanical Engineering, Swamy Vivekananda Engineering College, Bobbili, Andhra Pradesh 535558, India*
[3]*Department of Mechanical Engineering, PVP Siddhartha Institute of Technology, Kanuru, Vijayawada, Andhra Pradesh 520007, India*
[4]*Department of Chemistry, College of Natural and Computational Science, Debre Berhan University, Debre Berhan 445, Ethiopia*

Correspondence should be addressed to Naziya Begum; drnaziyabegum15@dbu.edu.et

Received 1 August 2022; Revised 17 September 2022; Accepted 6 April 2023; Published 17 April 2023

Academic Editor: Karthikeyan Sathasivam

It has been demonstrated that B20 biodiesel can be used in diesel engines without modifying their specifications. It is still being developed to reduce dependence on diesel fuel by developing biodiesel with a higher percentage of palm oil. Alcohol is added to biodiesel to reduce problems with fuel injection due to its high viscosity. In this study, the biodiesel properties of diesel-palm cooking oil-methanol/ethanol/butanol blends are investigated in relation to diesel engine performance and potential exhaust emissions. The percentages of palm cooking oil used were 30%, 40%, 50%, 60%, 70%, 80%, and 85%. A 15% concentration of methanol, ethanol, and butanol alcohol was used. According to chemical and physical tests, biodiesel with a higher palm oil content had poorer properties. A biodiesel blend that combines diesel, palm oil, and methanol can perform almost as well as diesel fuel in terms of exhaust emissions and engine performance.

1. Introduction

The use of fuel oil in India has passed the peak of the balance between production and consumption. The tendency of this high fuel demand is reflected in the increase in the volume of motorised vehicles and the volume of fuel oil imports shown in the volume of motorised vehicles by 62% and an increase in fuel imports by 26% in 2022. Biodiesel is an alternative fuel sourced from vegetable oils or animal fats that are produced through esterification/transesterification processes [1]. B20 biodiesel is implemented as the main fuel for diesel engines. The use of biodiesel fuel results in lower engine performance than diesel fuel despite more environmentally friendly engine emissions [2]. The higher the palm oil content, the lower the engine torque and power. This is due to the low calorific value and high viscosity of palm oil compared to those of diesel fuel [3]. The decline in performance of biodiesel-fuelled diesel engines can be improved by adding alcohol to the fuel [4]. In addition, the addition of alcohols such as methanol, ethanol, and butanol also has a positive impact on reducing carbon monoxide (CO) and hydrocarbon (HC) emissions and fuel consumption produced by diesel engines [5]. The low viscosity properties, high oxygen content, and high cetane number in alcohol are the main factors for lower diesel engine exhaust emissions than when using biodiesel fuel. Therefore, in line with the programme to reduce fossil fuel dependence, this study observed diesel fuel blended with palm cooking oil and methanol or ethanol or butanol alcohol additives to improve biodiesel properties [6]. A biodiesel blend consisting of diesel-palm cooking oil-alcohol, methanol, ethanol, and butanol was investigated through its physical and chemical

properties. Furthermore, the tendency of biodiesel properties was correlated with diesel engine performance and exhaust emissions.

2. Research Methods

Palm cooking oil was obtained from a commercial shop in Chennai city. Meanwhile, methanol, ethanol, and butanol alcohols were obtained from a chemical store. In the process of making biodiesel formulation, the diesel fuel-palm cooking oil-alcohol (methanol/ethanol/butanol) were mixed according to the measurements shown in Table 1. Observations were made on the physical and chemical properties of biodiesel such as viscosity, calorific value, flash point, and density. In the process, the biodiesel testing method was carried out, as shown in Table 2. The physical and chemical properties of biodiesel B30, B40, B50, B60, B70, B80, and B100 were evaluated for quality properties. To find out the tendencies described by the physical and chemical test results, graphs were made.

Table 1: Biodiesel property testing methods.

S. no.	Type of examination	Method
1	Kinematic viscosity at 40°C	ASTM D 445-062
2	Calorific value	ASTM D 5865-133
3	Flash point	ASTM D 93-074
4	Specific gravity	ASTM D 1298-12

Table 2: Biodiesel formulation.

S.No.	Biodiesel volume	Biodiesel volume (ml)		
		Solar	Palm cooking oil	Alcohol
1	B30 = P	700	300	0
2	B30A = Q	550	300	150
3	B40A = R	450	400	150
4	B50A = S	350	500	150
5	B60A = T	250	600	150
6	B70A = U	150	700	150
7	B80A = V	50	800	150
8	B100A = W	0	850	150

3. Results and Discussion

3.1. Viscosity of Biodiesel. Viscosity is used as a parameter to measure fuel quality. The higher the viscosity of biodiesel, the more viscous the fuel and the more difficult it is to mix with air, making the fuel injection process difficult [7]. Figure 1 shows the viscosity of biodiesel with varying volumes. In general, biodiesel blended with alcohol produces higher viscosity than 30% biodiesel without alcohol (B30). The viscosity of biodiesel with ethanol alcohol blends was higher than that of biodiesel methanol and biodiesel butanol blends. Meanwhile, the viscosity of biodiesel with methanol alcohol blends was lower than that of biodiesel ethanol and biodiesel butanol blends. The highest viscosity was obtained in fuel with 85% palm cooking oil and 15% ethanol or B100A. The lowest viscosity was obtained in the fuel with 30% palm cooking oil and 15% butanol or B30A. Biodiesel fuel with high viscosity properties is detrimental to the fuel injection process [8]. The use of ethanol alcohol blends in biodiesel compared to methanol or butanol alcohol blends could produce high emissions and high fuel consumption.

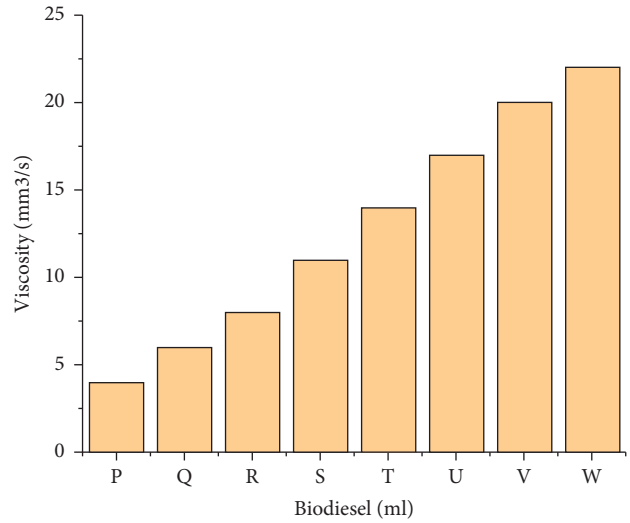

Figure 1: The viscosity of biodiesel with varying volumes.

3.2. Calorific Value of Biodiesel. The calorific value of fuel indicates the amount of energy produced during the combustion process [9]. The amount is influenced by the composition of the fuel. Figure 2 shows the trend of the decreasing calorific value of biodiesel with alcohol blends compared to that of biodiesel without alcohol. The higher the palm cooking oil content, the lower the calorific value. In this case, the lowest calorific value belongs to the fuel with 85% palm cooking oil and 15% ethanol alcohol blends (B100A). The calorific value of biodiesel with butanol alcohol blends appears to be higher than that of biodiesel with ethanol or methanol alcohol blends. In this case, the highest calorific value belongs to the fuel with 30% palm cooking oil and 15% butanol alcohol blends [10]. The lowest calorific value belongs to the biodiesel with ethanol alcohol blends. The use of fuel with a high calorific value will improve engine performance. This is due to the large amount of calorific energy produced so that the quality of the combustion process is better. Therefore, biodiesel with butanol alcohol blends has the potential for better combustion quality and emissions than biodiesel with methanol or ethanol alcohol blends.

3.3. Flash Point of Biodiesel. The flash point of a fuel is an indicator that the fuel can burn when it comes into contact with heat or fire. The lower the flash point, the more flammable the fuel [11]. Fuel flammability affects the rate of combustion, thereby accelerating the increase in combustion chamber temperature and maximising the combustion process. This benefits the working power of the engine. However, an excessive increase in the combustion chamber temperature triggers the formation of NOx emissions. Figure 3 shows the flash point test results with varying

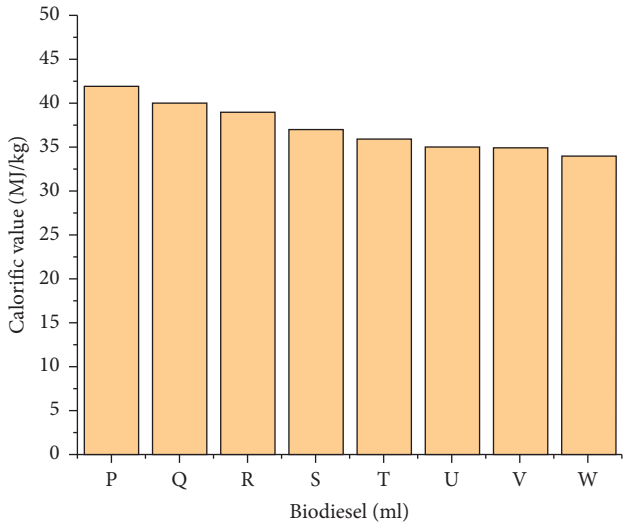

Figure 2: The trend of decreasing calorific values of biodiesel.

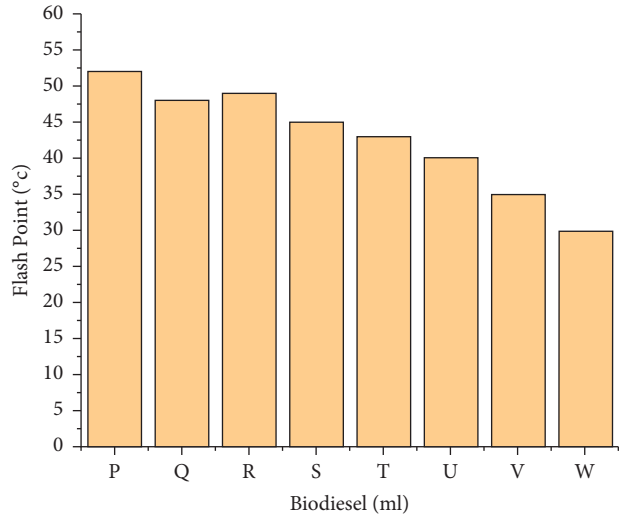

Figure 3: The flash point test results with varying biodiesel volumes.

biodiesel volumes. In general, biodiesel with alcohol blends has a higher flash point than 30% biodiesel fuel without alcohol blends. The flash point of biodiesel with methanol alcohol blends is lower than that of biodiesel with ethanol or butanol alcohol blends. Therefore, biodiesel with methanol alcohol blends has the potential to produce higher engine performance and emissions than biodiesel with ethanol or butanol alcohol blends.

3.4. Biodiesel Density. The density of biodiesel is very important to determine the quality of the fuel combustion process. The higher the fuel density, the better the fuel quality, which supports the perfect combustion process [12]. The higher the fuel density, the higher the fuel consumption. Figure 4 presents the density of the fuel with varying palm cooking oil content. Biodiesel has a higher density when it contains more palm cooking oil. The density of biodiesel

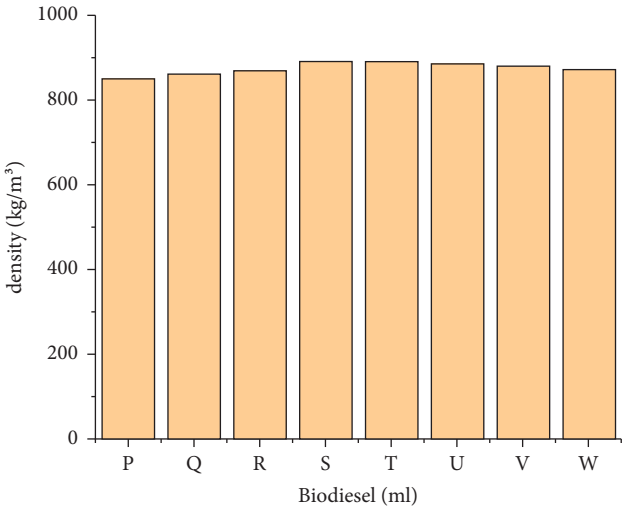

Figure 4: The density of the fuel with varying biodiesel volumes.

with methanol alcohol blends is lower than that of biodiesel with ethanol or butanol alcohol blends. However, the increase in the biodiesel density value is not significant between methanol alcohol-blended biodiesel and ethanol/butanol alcohol-blended biodiesel density.

4. Conclusion

The diesel-palm cooking oil-methanol blend biodiesel fuel has the highest flash point, lowest viscosity, high calorific value, and low density compared to diesel-palm cooking oil-ethanol or butanol blends. The diesel-palm cooking oil-methanol blend biodiesel has the potential to produce better performance and emissions than diesel-palm cooking oil-ethanol or butanol blends.

Data Availability

The data used to support the findings of this study are included in the article.

Conflicts of Interest

The authors declare that they have no conflicts of interest regarding the publication of this paper.

References

[1] O. M. Ali, R. Mamat, N. R. Abdullah, and A. A. Abdullah, "Effects of blending ethanol with palm oil methyl esters on low temperature flow properties and fuel characteristics," *International Journal of Advanced Science and Technology*, vol. 59, pp. 85–96, 2013.

[2] L. G. Anderson, "Effects of using renewable fuels on vehicle emissions," *Renewable and Sustainable Energy Reviews*, vol. 47, pp. 162–172, 2015.

[3] J. M. Bergthorson and M. J. Thomson, "A review of the combustion and emissions properties of advanced transportation biofuels and their impact on existing and future engines," *Renewable and Sustainable Energy Reviews*, vol. 42, pp. 1393–1417, 2015.

[4] A. Calam, H. Solmaz, A. Uyumaz, S. Polat, E. Yilmaz, and Y. Içingür, "Investigation of usability of the fusel oil in a single cylinder spark ignition engine," *Journal of the Energy Institute*, vol. 88, 2014.

[5] W. N. M. Wan Ghazali, R. Mamat, H. Masjuki, and G. Najafi, "Effects of biodiesel from different feedstocks on engine performance and emissions: a review," *Renewable and Sustainable Energy Reviews*, vol. 51, pp. 585–602, 2015.

[6] A. Goswami, S. Vashist, and A. Nayyar, "Effect of Compression Ratio on the Performance Characteristics of Spark Ignition Engine Fueled with Alternative Fuels: A Review," in *Proceedings of the SAE 2015 World Congress and Exhibition*, Detroit, Michigan, 2015.

[7] C. Ji, C. Liang, Y. Zhu, X. Liu, and B. Gao, "Investigation on idle performance of a spark ignited ethanol engine with dimethyl ether addition," *Fuel Processing Technology*, vol. 94, no. 1, pp. 94–100, 2012.

[8] S. Li, W. Li, M. Xu, X. Wang, H. Li, and Q. Lu, "The experimental study on nitrogen oxides and SO2 emission for oxy-fuel circulation fluidized bed combustion with high oxygen concentration," *Fuel*, vol. 146, pp. 81–87, 2015.

[9] B. M. Masum, H. H. Masjuki, M. A. Kalam, I. M. Rizwanul Fattah, S. M. Palash, and M. J. Abedin, "Effect of ethanol–gasoline blend on NOx emission in SI engine," *Renewable and Sustainable Energy Reviews*, vol. 24, pp. 209–222, 2013.

[10] S. S. Reham, H. H. Masjuki, M. A. Kalam, I. Shancita, I. M. Rizwanul Fattah, and A. M. Ruhul, "Study on stability, fuel properties, engine combustion, performance and emission characteristics of biofuel emulsion," *Renewable and Sustainable Energy Reviews*, vol. 52, pp. 1566–1579, 2015.

[11] H. Solmaz, "Combustion, performance and emission characteristics of fusel oil in a spark ignition engine," *Fuel Processing Technology*, vol. 133, pp. 20–28, 2015.

[12] E. Vanzela, W. C. Nadaleti, R. A. Bariccatti et al., "Physicochemical properties of ethanol with the addition of biodiesel for use in Otto cycle internal combustion engines: results and revision," *Renewable and Sustainable Energy Reviews*, vol. 74, pp. 1181–1188, 2017.

Hindawi
Journal of Engineering
Volume 2023, Article ID 2420903, 13 pages
https://doi.org/10.1155/2023/2420903

Research Article

Plug Valve Surface Defects Identification through Nondestructive Testing and Fuzzy Deep-Learning Algorithm for Metal Porosity and Surface Evaluation

V. Jacintha,[1] **S. Karthikeyan**,[1] **and P. Sivaprakasam**[2]

[1]*Department of Electronics & Communications Engineering, Sathyabama Institute of Science & Technology, Chennai, India*
[2]*Department of Mechanical Engineering, College of Electrical and Mechanical Engineering, Addis Ababa Science and Technology University, Addis Ababa, Ethiopia*

Correspondence should be addressed to P. Sivaprakasam; shiva@aastu.edu.et

Received 7 July 2022; Revised 24 July 2022; Accepted 26 July 2022; Published 27 March 2023

Academic Editor: Karthikeyan Sathasivam

This paper addresses the detection and identification of flaws in Plug valves. The Plug valve thermal image is acquired using a Fluke thermal camera [TiS20]. Thermal images of the Plug valve are used for the identification of flaws such as Crack, Porosity, Corrosion, and Internal defects. The thermal images detect the surface flaws and never subsurface flaws in Plug valves. The subsurface flaws detection is a challenging problem in valve inspection. In this paper, the thermal images obtained after the dye penetrates the surface valve detect the surface flaws more efficiently after applying the Fuzzy Deep Learning Algorithms. DyePenetrating Test (DPT) combined with Infrared Thermography is proposed to identify heat flux changes and flaws in the faulty metal surface of Plug valves. In DPT, thinned paint is employed on the metal surface that displays metal porosity and even fine cracks. After DPT, thermal images of the Plug valve are processed through the Fuzzy Deep Learning Algorithm to evaluate flaws. The Fuzzy Algorithm is utilized prior to Deep Learning to simplify and speed up the classification task. The flaws are identified using Slicing operation and the following parametric quantities such as Accuracy, Mathew's Correlation Coefficient (MCC), Local Self-Similarity Descriptor (LSS), Precision/Recall, *F*-measure, and Jaccard Index. The parametric quantities depict corresponding variations with regard to surface coarseness and metal flaws. The DPT and Fuzzy Deep Learning Algorithm identify metal defects with 80.67% accuracy.

1. Introduction

The American Petroleum Institute (API) criterion encompasses inspection, examinations, and pressure test for metal-to-metal seated Plug valves. The manufacturer and purchaser perform the inspections. The inspection may include a pressure test conducted in manufacturer's plant. During assembling of Plug valve components, inspection is done through Nondestructive Testing (NDT). The valve manufacturer initially performs a Dye-penetrating examination. Furthermore, liquid penetrant testing is performed according to American Society of Mechanical Engineers (ASME) *B* 16.34 standards. Moreover, Pressure test is accomplished with any external pressure due to seat leakage. Moreover, when an end-clamping fixture is used, it does not affect the seat leakage of the Plug valve. For lubricating Plug valves, high-pressure closure test is compulsory while low-pressure closure test is an option. Furthermore, Backseat test is required for Plug valves and a High-pressure pneumatic shell test is very important for Plug valve inspection. The pressure during testing will be 110% of maximal permissible pressure at 100 F (38°C). The test fluid used for a high-pressure test can be air, inert gas, kerosene, water, or noncorrosive liquid with a viscosity lesser than that of water. The test fluid temperature range shall be within 41 F (5°C) to 122 F (50°C). For low-pressure test, the test fluid can be air or inert gas. These test fluids detect any leakage in the valve. Water utilized for any test may comprise of water-soluble oil or rust inhibitor. A wetting agent may also be included in water. Plug valves are generally made of cast iron or stainless

steel, and for these materials water having a chloride capacity within 100 parts/million (ppm) can be utilized. For Shell tests and Backseat tests, a visually detectable leakage is not permitted from any part of the valve. For valves with adjustable steam seals, the manufacturer must look for steam seals, which are capable of retaining pressure of at least 100 F (38°C) valve grading free from visible leakage. For valves, with nonadjustable steam seals, a visually noticeable leakage throughout the shell test is not permitted. If the test fluid is liquid, there shall be no seeable proof of droplets or wetting of the outside surface of the valve. If the test fluid is air/inert gas, no leakage will be revealed by the detection procedure. For both low-pressure and high-pressure closure tests, it is not permitted to have any visual evidence of leakage as well as any structural damage anywhere in the Plug valve. Recently, quality inspection of material has been automated for increasing productivity with a quality-finished product. The automation process reduces the manual inspection because of sleek design and functionality of automated machines. The automated machines for material quality inspection perform better than manual inspection. The automation processes detect faults in a material more accurately and classify their quality level. The main advantages of automated inspection over manual processing are 24/7 operation, high speed, continuous monitoring with remote access through sensors, and working with different kinds of materials. The component in an automated inspection system consists of control circuits, sensors, image acquisition system, and image-processing algorithms for zero defects in the production unit. The automation process of inspection starts with an image acquisition of the material under inspection through machine-vision cameras. The machine-vision camera captures the images of materials, transmits them to the computer for image analysis, and decides the quality based on image-processing algorithms. Three parameters that need to be taken into account while setting the camera and lens during image acquisition are the viewing angle, depth of field, and target area [1]. The image-processing algorithms is used for detect flaws in the Plug valve material. The Plug valve needs critical inspection during the manufacturing process to avoid repairs and failures. The critical inspection prevents external and internal leakage in oil and gas applications. Figure 1 shows the line diagram of a Plug valve. In oil and gas applications, surface defects will grow exponentially because of cavitations, high velocities, high-pressure drops, throttling, and solids/slurries. The root cause of all these problems mentioned is solved through an automatic inspection system over the valve surface. However, the existing automatic inspection system is performed with machine-vision cameras or ultrasonic surface crack detection. The vision-based quality inspection systems analyze the surface of a Plug valve without injection of the test fluid. The ultrasonic surface crack detection testing also cannot analyze the surface during test pressure and test leakage. The solution for surface analysis in a Plug valve is performed with ultrasonic surface crack detection and Dye-Penetrating test. The Plug valve surface testing of the test fluid under pressure through thermal vision automatic inspection system identifies the various defects on the inner surface of Plug valves. Infrared Thermography renders enhanced solutions for online identification of Internal defects [2]. The various defects on the surface, such as Cracks, Porosity, Internal defects, and Corrosion, are identified before and after the test fluid inspection is completed. These flaws are the cause for initial fatigue crack initiation (FCI) and should be reduced to enhance the fatigue life of a weld joint [3]. The investigation strongly detected the location and type of flaws [4].

Figure 1: Plug valve with inverted plug type design.

The surface valve defects identified through the thermal images before and after the fluid test analyze the surface temperature during high pressure. It is necessary to acquire thermal images over the inner and outer surfaces of the Plug valve and study surface characteristics in terms of Cracks, Porosity, and Internal defects. Porosity defects can be easily eliminated in the presence of vacuum [5]. Furthermore, images acquired after certain duration of time are used to check the corrosion on surface, once the complete testing of valves is finished. These acquired thermal images under different faults are trained using Deep Learning algorithms after images are processed through Fuzzy Cluster algorithms. The applicability and novelty of the proposed work are given in Table 1.

2. Literature Survey

2.1. Inferences from Literature Survey. From the review of literature till now, the various faults are identified using a high-speed camera, signal processing and soft computing algorithms such as wavelet transform, genetic algorithm, and neural network. However, these tests were conducted only in offline mode, i.e., the materials were tested without test fluids, especially in valves. Plug valves being the most frequently utilized valves are primarily used in oil and gas industries, and require multiple inspections on the surface of the valve. In the existing system, the Plug valve is examined using the Dye-Penetrating test, Ultrasonic test, and Fluid test. These testing methods are performed independently in offline mode. Using Nondestructive Testing (Dye-Penetrating Test), we can identify the surface defects such as Cracks. To identify the subsurface defects such as Porosity and Internal defects, we utilize Ultrasonic Nondestructive Testing. Using Nondestructive Testing, we can only detect

Table 1: Applicability and novelty of the proposed work.

Technique	Applicability	Remarks
Machine learning [6]	Difficulty for real-time application	Nonavailability of real-time datasets for implementation. Learning process is slow, with issues in reusing, integrating, and debugging the models.
Neural network [7]	Not applicable	The training time is quiet long. There are chances for misclassification to occur.
Deep learning	Applicable	Automated feature extraction and classification. Training time is less with no misclassifications. Works effectively on real-time plug valve images.

the Plug valve defects; however for defect classification, we require a combination of the Fuzzy Slicing Algorithm and the Deep Learning Architecture. A novel method of combining these methods is required to improve the accuracy in testing with low cost and reduce the time in a single test. The various research work related defect detection is presented in Table 2.

3. Materials and Methods

The Plug valves classify as Lubricated and nonlubricated design along with varied port openings, single and multiple port plugs. The Plug valve is used under great pressure and extreme temperature. The Plug valves are prone to defects such as Cracks, Porosity defects, Internal defects, and Corrosion. Among these flaws, Cracks are the major problem, which is to be identified at the early stage, or otherwise it would lead to rework and consume more time. Miniature Crack is a line on the surface of the valve and later causes fragments, which lead to a serious damage. These miniature cracks are not able to be visualized through human eye and become visible only after certain duration once the Plug valve undergoes heavy testing. The major cause of these cracks because of tension in the Plug valve becomes greater than the metal strength. When the heavy pressure works on Plug valves, the stress develops and it accumulates. The Porosity occurs over the welded regions in the Plug valve. This porosity forms due to trapped or shielding gases and pressure on welded specimen is produced. The gases are engulfed in the liquefied specimen and later expelled on the welded metal after solidification. If the porosity is in the form of round holes then it is called as spherical porosity, but when the holes are stretched the flaws are called as wormholes or piping. Corrosion occurs in the Plug valve metals after reacting with the ambient temperature and atmosphere. The corrosion occurs due to electrochemical oxidation because of the Plug valve metal surface reacting with oxygen or sulfate present in the atmospheric gases. The Internal cracks occur in the Plug valve in the inner surface of the welding regions. The two types of welding metal cracks are Root cracking and heat-affected-zone (HAZ) cracking (under bead cracking). Weld metal cracks are flaws that occur within the liquefied metal. HAZ cracks are flaws that occur when the weld solidifies at a very fast rate, which makes the base material to be very fragile, thereby resulting in internal cracks. Gas porosity types such as Pinholes, Subsurface Blow holes, and open holes are used. Pinholes alias porosities are below 2 mm hole size and present in molds of upper surface. Subsurface blowholes' size is of more than 2 mm in diameter, which occurs inside the cast and seeable only after prolonged usage of the valve. The open holes occur during casting and the surfaces hence are easy to detect. Cracks in valves classify into two types such as hot cracks and cold cracks. The hot cracks happen because of crystallization procedure in the weld joint. Cold cracks form after welding, when the weld happens to cool down. The solids or slurries of abrasive nature gradually wear down from the Plug valve surface. The cavity flaws caused when the pressure inside the valve falls drastically below the vapor pressure lead to vapor bubbles. When the pressure is low in valves, these bubbles burst causing dents onto the metal surfaces which gradually wear down the valve body, resulting in an abnormal noise during operation, and which reduce the flow rates in the valves.

3.1. Detection of Plug Valve Defects through Thermal Images. Plug valve defects are detected through thermal images acquired during the testing conditions such as Pressure test and Dye-penetrating method. Figure 2 shows the block diagram of Nondestructive Testing of a Plug valve through thermal imaging. Thermal images are acquired from a Plug valve for defect identification using Fluke thermal camera (Model No: TiS20). The thermal camera consists of a 5 hrs battery life. The camera works on Passive Infrared Thermography principle and never requires an external energy source. Infrared thermography camera detects infrared radiation emitted from an object and converts it into temperature for thermal image. The optics of the thermograph enables the rays to concentrate on the thermal detector and produces an image directly proportional to the radiation. The thermal camera needs less maintenance and is easy to operate. The thermal images are acquired for defects' detection from the images taken before and after, Pressure test and Dye-Penetrating test. Pressure test: In a Plug valve, the test fluid is liquid; the valve must be necessarily free from entrapped air throughout the test. Furthermore, safety coatings on the valve surface should be strictly avoided before pressure test, since they cover the surface defects. Dye-Penetrating inspection (DPI) works on the principle of Capillary action. In a DPI method, thin liquid sinks into a clear and dry surface and goes into the flaws and thereby makes flaws clearly visible. For the DPI method, the items such as cleaner, penetrant, and developer are required. Initially, the inner surface of a Plug valve is cleaned and impurities removed for applying the penetrant and developer. Next, the penetrant is sprayed over the inner surface of the Plug valve using a brush. The penetrant, which is surplus

Table 2: Recent research work related to defect detections.

Author/Year	Problem	Solution
Ye and Toyama [6]	To analyze the efficiency of various deep learning architectures.	A total of 7000 real-time images are evaluated. A total of 17 flaws are detected.
Ajmi et al. [8]	Defect detection and classification on small weld X-ray image datasets.	Data augmentation and deep learning techniques utilized for obtaining best results.
Mery [7]	To automate the process of defect detection in aluminum castings.	Convolution neural network (CNN) model utilized for effective detection of defects
Daniel et al. [1]	Internal defects in pipes (0 to 2 inches).	Vertical insertion camera.
Xiao et al. [9]	To detect weld bead width and depth of penetration defects in welds.	Coaxial infrared pyrometer
Schaunberger et al. [10]	To identify weld seam defects such as pores, tapers, and regressions (copper)	Defect detected from temperature curves.
Gao et al. [11]	Process stability and weld formation (laser welding)	Analysis with a high-speed camera.
Lei et al. [12]	Influence of thermal effect on droplet transfer (cold metal transfer (CMT) laser welding)	Analysis with a high-speed camera and brightness curves
Huang et al. [13]	Welding defect identification (laser welding)	The defect identification through electrical signals of laser plasma and plasma flumes acquired by a high-speed camera
Gao et al. [14]	To identify invisible weld defects	Magneto-optical imaging system and grayscale curves
Hamade and Baydoun [4]	To identify wormhole defects in welded lap joints.	X-ray computed tomography (CT) scan and Otsu segmentation
Zhang et al. [2]	To detect weld seam penetration defects	Multiangle image acquisition and convolution neural network (CNN)
Jiang et al. [5]	To identify porosity defects at ambient pressures.	High-speed camera. No defects under vacuum
Xie et al. [15]	To detect metal rust	High-speed images and Acoustic emission signal of pulsed laser
Zhou et al. [16]	To identify surface pit, spatter, softening in heat-affected zone (HAZ), oxide, and porosity	Addition of Sn foil
Choi et al. [17]	To detect lack of fusion (LOF), gas pores	Laser metal deposition technique and fatigue test to check efficiency.
Bacioiu et al. [18]	To monitor tungsten inert gas welding	High dynamic range camera and Fully convolution neural networks and convolution neural networks (FCN & CNN).
Shah and Liu [19]	To identify interfacial cracks, solidification cracks, surface defects, and oxides	Ultrasonic waves in resistance spot welding (URSW)
Nacereddine et al. [20]	To detect cracks, porosity, lack of penetration (LOP), and solid inclusion	Classification in radiographic images.
Francis et al. [21]	To analyze the potential of vacuum laser welding for thicker areas of nuclear parts.	Achieves the required weld quality equivalent to the electronbeam welding (EBW).
Zhang et al. [22]	Comprehensive insights of laser welding process.	Multiple optical sensor systems
Xu et al. [23]	To identify Keyhole-induced porosity	Three-dimensional transient model
Chaoudhuri et al. [3]	To identify Inherent flaws and fatigue cracks	Stress analysis and micro-computed tomography (CT)
Son et al. [24]	To examine the strength that exists between a material deposited and its substrate.	High bonding strength verified through Shear tests.
Reisgen et al. [25]	To detect porosity defects	)Nonvacuum electron beam welding (NV-EBW)
Millon et al. [26]	To identify the lack of fusion (LOF) or porosity defects	Laser ultrasonic signals.
Wu et al. [27]	Expulsion identification	Welding force signal
Xie et al. [28]	Heat-affected zone (HAZ) Cracks(liquidation and strain age cracks)	Postweld hot isostatic pressing
Qian et al. [29]	To identify high residual stress	Spontaneous magnetic signals
Kim et al. [30]	To detect welding defects in underground curled pipelines	Magnetic flux leakage (MFL) sensor signals
Hongmin and Wang [31]	To identify tiny weld bead flaws (cracks, pores, lack of fusion (LOF), cavities)	Closed magnetic reluctance signals
Zhang et al. [32]	To detect flaws in power disk laser welding	Spectrometer signals
Li and Lu [33]	To fetch a novel alloy for Biomedical utilization with the apt Young's modulus	Powder metallurgy procedure is employed.
Proposed system	To identify porosity, crack, internal defects, and corrosion	Thermal images and fuzzy deep learning algorithm

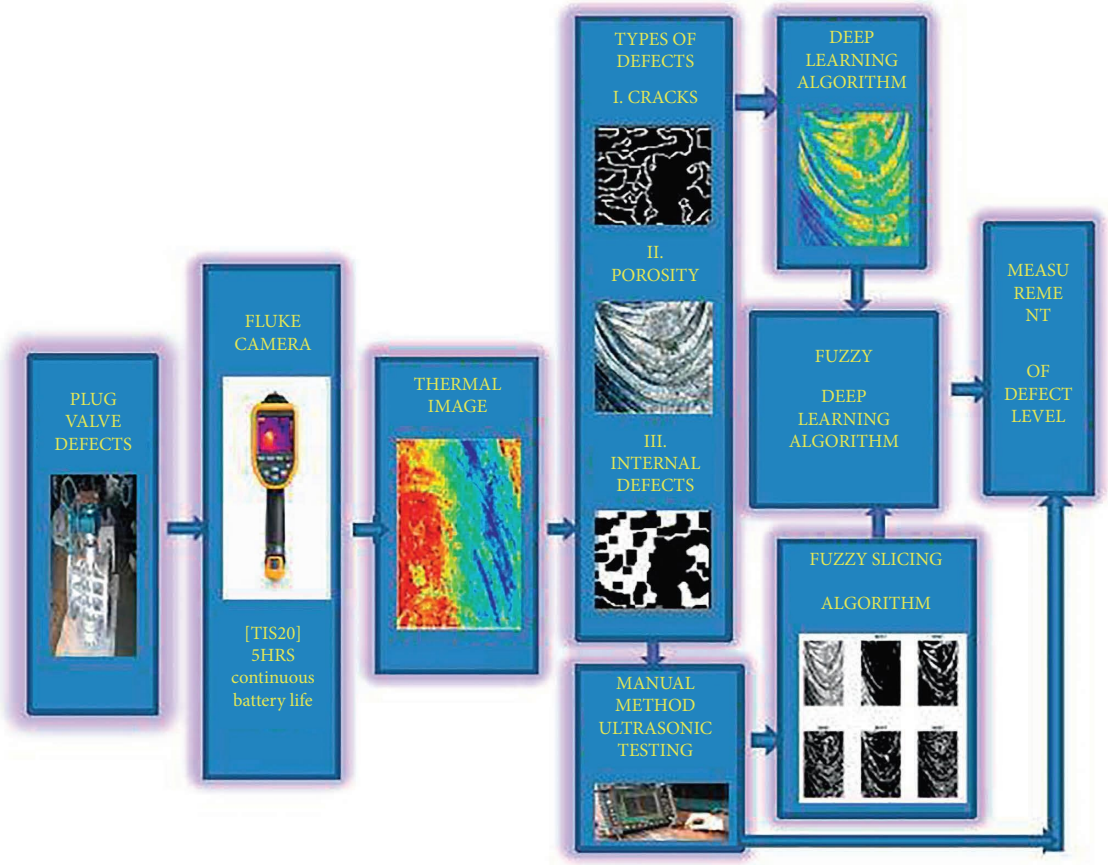

Figure 2: Block diagram of the proposed system.

over the Plug valve surface, is removed using cotton. Next, the developer is applied to make the flaws visible to naked eye. Furthermore, after visible inspection thermal images are obtained from the valves to detect the invisible flow using the proposed algorithm.

3.2. Ultrasonic Inspection. The Ultrasonic testing is performed through a SUB280 model instrument. The instrument consists of the following sections, Ultrasonic sensor and secure power supply unit with power barrier, signal barrier, RS485/RS232 converter, and Leak supervising software. The instrument checks the surface of the Plug valve for leakage using Acoustic emission. The Acoustic emission of the surface of the Plug valve reflects the distorted amplitude from the leakage surface. The leakage surface noise and the fluctuating amplitude show the change in pressure field linked with the flow of liquid in unstable condition. The instrument tracks the leakage for cylindrical surface in the Plug valve and the detection of minute leakage is still a challenging problem. For detecting the minute leakage, the thermal images are obtained for analysis through the proposed system.

3.3. Fuzzy. Fuzzy logic is performed through logical thinking with membership rules and functions. Fuzzy logic provides an effective solution for complex problems, with high accuracy and speed in execution. Fuzzy has a wide range of degrees of membership between 1 and 0. The partial membership arises when an element of one fuzzy set belongs to the other fuzzy set in the sample space. Fuzzy logic method is highly desirable for unsure or estimate reasoning with equivocal boundaries. Fuzzy logic algorithm is applied in image processing to resolve uncertainty issues in image pixels. Fuzzy logic finds the differences in the image pixels, which are either true or false, for a set of pixels. The Fuzzy logic is applied in the thermal image of valves to detect the faults in the valves. Fuzzy logic combines with Deep Learning techniques for fault detection. Fuzzy clustering permits the information to be grouped in greater than one cluster. The membership function (μ_{mn}) denotes the membership degree, as to which mth cluster the nth object belongs to.

The aim of the algorithm is to reduce the cost function, given as.

$$D = \sum_{n=1}^{N} \sum_{m=1}^{C} \mu_{mn}^{l} i_n - v_m^2, \tag{1}$$

N denotes the objects to be labeled (i.e., count of the image pixels). C denotes the cluster count. v_m represents the mth cluster centroid ranging from $\{v_1, v_2, \ldots, v_m\}$. l denotes the parameter that controls fuzziness that should be greater than 1. i_n denotes the particular image pixel. $\|\cdot\|$ represents the Euclidean distance measure. The cost function is minimized by continuously updating μ_{mn} and v_m.

$$\mu_{mn} - \frac{i_n - v_m^{-2(l-1)}}{\sum_{k=1}^{C} i_n - v_k^{-2(l-1)}},$$
$$v_m = \frac{\sum_{n=1}^{N} \mu_{mn}^{l} i_n}{\sum_{n=1}^{N} \mu_{mn}^{l}}. \quad (2)$$

The general fuzzy c-means (FCM) never considers any spatial information, therefore it is hindered by noise and artifacts. Hence, Spatial Fuzzy Clustering along with level set segmentation is considered for automated segmentation of defects in Plug valve images. Initially, Spatial FCM integrates spatial data throughout an adaptive optimization that obviates the intermediary morphological functions. The controlling parametric quantities required for Level set segmentation are obtained directly from the outcome of Spatial FCM. Finally, the Spatial FCM regularizes the Level set function.

The Level set function is denoted as,

$$\phi_0(x, y) = -4\varepsilon(0.5 - B_k), \quad (3)$$

where ε is a constant quantity governing the Dirac function. The Dirac function is expressed as:

$$\delta_e(x) = \begin{cases} 0, & |x| > \varepsilon, \\ \frac{1}{2\varepsilon}\left[1 + \cos\left(\frac{\pi x}{\varepsilon}\right)\right], & |x| \le \varepsilon. \end{cases} \quad (4)$$

B_k denotes the binary image expressed as $B_k = R_k \ge b_0$. Where b_0 is an adjustable threshold value. R_k denotes the region of interest in the FCM outcome.

3.4. Deep Learning. Deep learning is the part of machine learning and solves the problem like human brain, much better than human brain. Deep learning structure is similar to neural network, so called deep learning neural network. Neural network can go for two hidden layers, whereas Deep learning can go for 128 layers. Deep learning needs large datasets and specialized hardware such as graphics processing unit (GPU). However, machine learning needs less number of datasets and never needs any specialized hardware. The accuracy of Deep learning is better than those of machine learning and neural network. In Deep learning, computers learn to carry out classification straightaway from images, text, or sound. Deep learning does the same job many times and learns. The learning process in Deep learning is obtained from vast unstructured, interconnected datasets and from the learning solves the problem. Deep learning in image processing is utilized for object recognition, classification, and segmentation. In object recognition, Deep Learning algorithm can locate the object in the image, even in multiple locations without human intervention. Deep Learning algorithm detects faults in a Plug valve. Deep Learning algorithm classifies the defects in low-quality images. The Deep Learning algorithm is able to detect the various faults such as Porosity, Corrosion, Internal defects, and Cracks and multiple defects in single region. Recurrent Neural Network (RNN) is a type of Neural Network in which the output from the current step is fed as input to the next step; hence, it does not have the necessity to remember the outcomes of every step. The unique characteristics of the RNN are the Hidden State that has the capability to store and retrieve data in a sequence or operation. It utilizes common parametric quantities for all the inputs, since it executes a similar operation for all the inputs or hidden layers to yield the output. It renders common weights and biases to all layers, thereby lessening the issue of handling more parameters. Hence, these three layers can be merged together into a single recurrent layer. In this paper, RNN is utilized for fault detection.

The current state is expressed as follows.

$$h_t = f(h_{t-1}, x_t), \quad (5)$$

here, h_t is the present state, h_{t-1} is the former state while x_t is the present input. The input neuron might have performed the subsequent changes in the former input, hence we currently have the former input state rather than the present input. Hence, every consecutive input is termed as a time step.

The formula for employing activation function (tan$h$) is given as.

$$h_t = \tan h(W_{hh} h_{t-1} + W_{xh} x_t). \quad (6)$$

W_{hh} is the weight of the recurring neuron and W_{xh} is the weight of the input neuron. The recurring neuron considers the immediate former states. For longer sequences, the expression could have many such states. When the final state is computed, the next phase is production of the output. The output state is computed using the expression,

$$y_t = W_{hy} h_t, \quad (7)$$

where W_{hy} is the weight at the output layer.

Procedure for Recurrent Neural Networks.

(1) The input x_t is given to the network
(2) Compute the present state utilizing the present input and the former state i.e. we compute h_t
(3) The present h_t turns out as h_{t-1} for the following time step
(4) Several time steps can be carried out as the situation requires and merge the data from all the former states
(5) After completion of the time steps, the last current state is utilized to compute the output y_t
(6) The output is equated with the actual outcome, to check if there is any difference and the error is determined
(7) The error is fed back to the network for updating the weight and the network is trained.

4. Results and Discussion

The Deep Learning algorithm can analyze Cluster 1 given by fuzzy, which contains two defective Thermal crack images, assigns weights or probabilities, and finally outputs the best

match. Hence, the classification task is completed accurately at a faster rate.

The output images of the Proposed method are shown in Figure 3 with the numbering from [1–17]. Image segmentation is generally used to identify objects and boundaries (lines, curves, etc.) in thermal images. More incisively, image segmentation is the procedure of assigning a label to each image pixel, in such a way that pixels with a similar label have certain features such as color, intensity, or texture in common. The result of image segmentation is a group of segments that collectively encompass the full image, or a group of contours extracted from the thermal image. Nearby regions significantly vary with regard to the similar features. Picture 3 represents Edge Detection that possesses a wide range of mathematical operations that intend to detect points in a digital image where the image luminance varies sharply or has discontinuities. The discontinuities correspond to discontinuities in depth, surface orientation, changes in material properties, and fluctuations in scene illumination. Applying an Edge Detection Algorithm to an image may significantly reduce the quantity of information to be processed and may therefore filter out data that may be considered as less relevant, while saving the vital structural properties of an image. Pictures 4 and 5 denote the images with porosity Cluster 1 and Cluster 2, respectively. For a Good image, the Porosity count is 162. Picture 6 denotes the original bad image, in which the defect is indicated by a red marking, which shows the defect in the form of tiny granules close to each other. Picture 7 denotes the segmented image. Segmentation divides an image into distinguishable regions comprising of pixels with common properties. The defect in the segmented image is denoted by the red marking. Picture 8 denotes edge detection being carried out, which is the process of finding out boundaries of an object within an image. The defective region is denoted by red marking. Pictures 9 and 10 denote the image with porosity Cluster 1 and Cluster 2 for metal surface of valves. It clearly shows the porosity defect, which is in the form of closely, spaced granules, whereas the left-hand side of the images seems to be clear. The porosity count in the defective image is found through pixel count and is found to be 414 holes in count. Picture 11 denotes Thermal good image, which is obtained by utilizing Thermal Imaging. Picture 12 denotes the segmented version of the thermal image. Picture 13 denotes Edge Detection. The points at which image luminance varies sharply are typically organized into a set of curved line segments called edges. Pictures 14 and 15 denote the images with porosity Cluster 1 and Cluster 2, respectively. For a good thermal image, the porosity count is 54. Picture 16 denotes the defective thermal image, which is obtained by using Infrared Thermography. Infrared Thermography can identify heat patterns in the infrared wavelength spectrum that are not visible to the naked eye. The defect is indicated by a red marking. Picture 17 denotes the segmented image. Segmentation is the procedure of grouping the pixels of an image in terms of color, texture, and intensity. The right-hand side defective portion of the image, which is indicated by a red marking, is grouped together since they are sharing the same characteristics. Picture 18 denotes the edge detection. It is the process in which image brightness changes in the overall image are analyzed. The defective region in the image is indicated by a red marking. Pictures 19 and 20 denote the porosity defect in the image in terms of Cluster 1 and Cluster 2. Porosity is the presence of cavities in the weld metal caused by the freezing in of gas released from the weld pool as it solidifies. For a Defective thermal image, the porosity count is 72.

In Infrared thermography, each pixel in the image may reflect different degrees of temperature. In some cases, few pixels may reflect the same amount of energy. Hence in Figures 4(a) and 4(c) which denote the thermal images with and without defects, respectively, the difference in reflected energy is represented through different colors. Figures 4(b) and 4(d) denote the Surface plots of the defective and nondefective thermal images, respectively. Surface plot is a graphical version of the two thermal images equivalent to a histogram plot. In Infrared Thermography, defects are more clearly visible and detected easily through algorithms.

The Fuzzy Clustering outputs are denoted in Figure 5 with the numbering from [1–14] and Fuzzy Slicing outputs are denoted in Figure 6 with the numbering from [5, 15–21]. Using fuzzy, it processes the image and forms clusters, totally 4 clusters are formed. Picture 1 comprises of Cluster 1, which contains two Crack images. Picture 2 comprises of Cluster 2, which contains two Porosity images. Picture 3 comprises of Cluster 3, which contains two Corrosion images. Picture 4 comprises of Cluster 4, which contains the Internal Defect image. A similar process is carried out for detecting Porosity, Crack, Internal defects and for classifying them. Picture 17 indicates the index of clusters. Hence, the fuzzy performs slicing of the input image and so five indices or slices are obtained. Picture 18 indicates the boundary, where exactly the defect is located and hence further processing can be performed. Initially, the boundary is not determined. These figures give details on slicing performed by Fuzzy on Defective images. Using fuzzy, 4 clusters are formed. Picture 5 comprises of Cluster 1, which contains two Defective Crack images. The defects in the crack images are indicated by red markings. Picture 6 comprises of Cluster 2, which contains two defective Porosity images. Picture 7 comprises of Cluster 3, which contains two defective Corrosion images. Picture 8 comprises of Cluster 4, which contains the Internal Defect image. A similar process is carried out for detecting defective Porosity, Crack, Internal defects and for classifying them. Picture 19 indicates the fifth cluster group, hence the fuzzy performs slicing of the input image and so five indices or slices are obtained. Picture 20 indicates the boundary, where exactly the defect is located and hence further processing can be performed. Initially, the boundary is not determined. These figures give details on slicing performed by Fuzzy on Thermal images. Using fuzzy, it processes the images and forms clusters, totally 4 clusters are formed. Picture 9 comprises of Cluster 1, which contains two Thermal Crack images. Picture 10 comprises of Cluster 2, which contains two Thermal Porosity images. Picture 11 comprises of Cluster 3, which contains two Thermal Corrosion images. Picture 12 comprises of Cluster 4, which contains the two

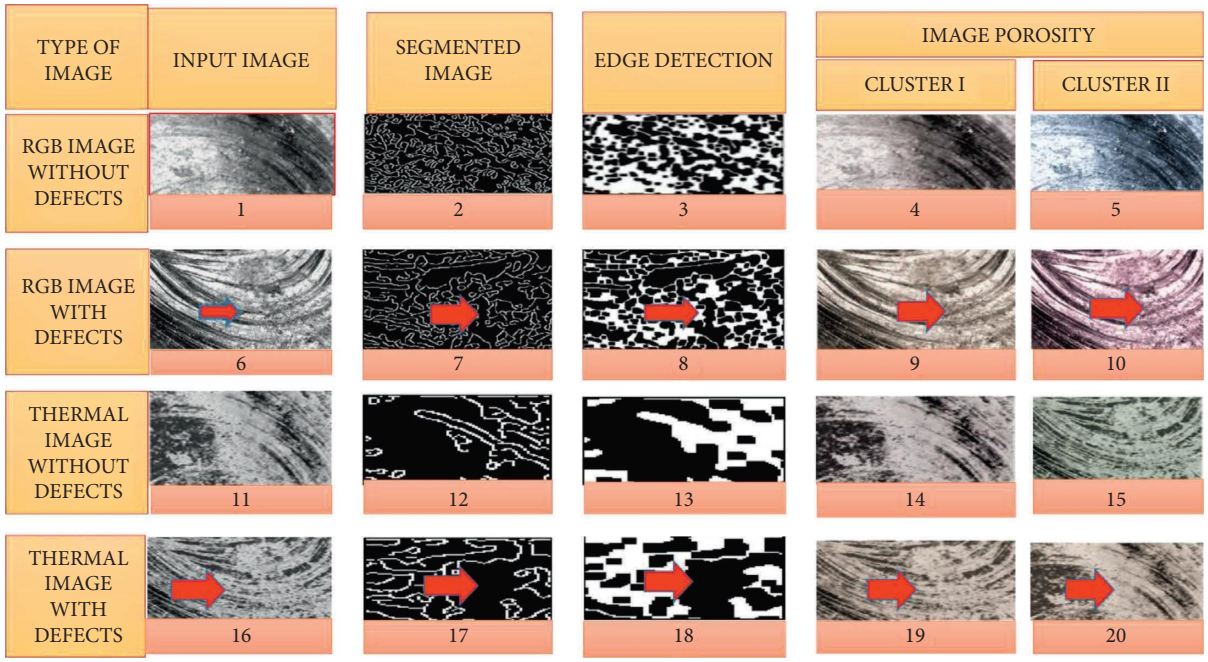

Figure 3: Fuzzy outputs for image porosity using adaptive K-means clustering algorithm.

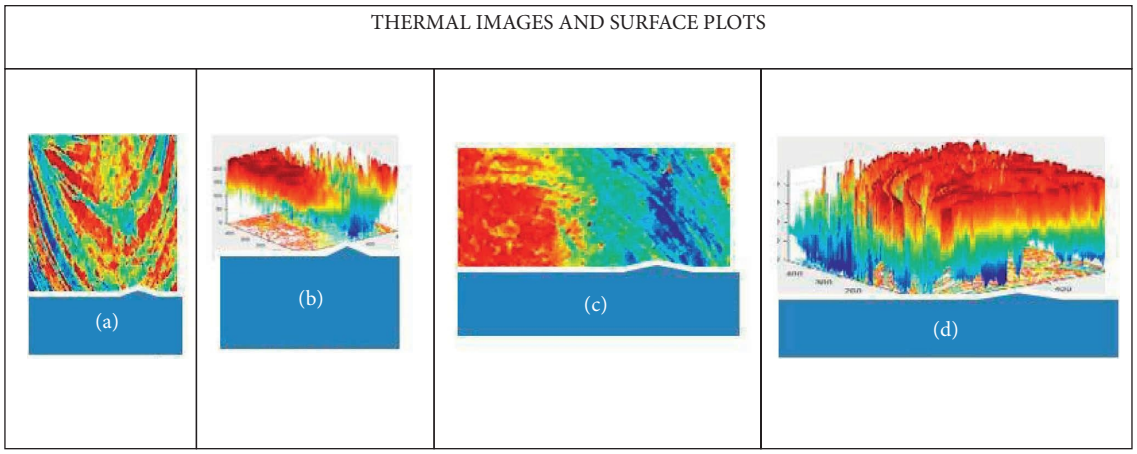

Figure 4: Metal surface and 3D plots. (a) Good thermal image. (b) Good thermal image surface plot. (c) Bad thermal image. (d) Bad thermal image surface plot.

Thermal Internal Defect images. A similar process is carried out for detecting Porosity, Crack, and Internal defects from the Thermal images for classifying defects. Picture 21 indicates the fifth group of pixel clusters, hence the fuzzy performs slicing of the input image and so five indices or slices are obtained. Picture 22 indicates the boundary as to where exactly the defect is located and hence further processing takes place. These figures give details on slicing performed by Fuzzy on defective Thermal images. Using fuzzy, it processes the images and forms clusters, totally 4 clusters are formed. Picture 13 comprises of Cluster 1, which contains two Defective Thermal Crack images. The defects in the Thermal crack images are indicated by red markings. Picture 14 comprises of Cluster 2, which contains two defective Thermal Porosity images. Picture 15 comprises of Cluster 3, which contains two defective Thermal Corrosion images. Picture 16 comprises of Cluster 4, which contains the two Thermal Internal Defect images. A similar process is carried out for detecting defective Thermal Porosity, Crack, Internal defects and also for classifying them. Picture 23 indicates the fifth index cluster, hence the fuzzy performs slicing of the input image and so five indices or slices are obtained. Picture 24 indicates the boundary, where exactly the defect is located and hence further processing takes place.

4.1. Deep Learning. For the Boundary detection and for accurate identification of defects, the Deep Learning algorithm is applied. Furthermore, the Deep Learning algorithm can analyze Cluster 1 given by fuzzy, which contains two defective Thermal crack images, assigns weights or

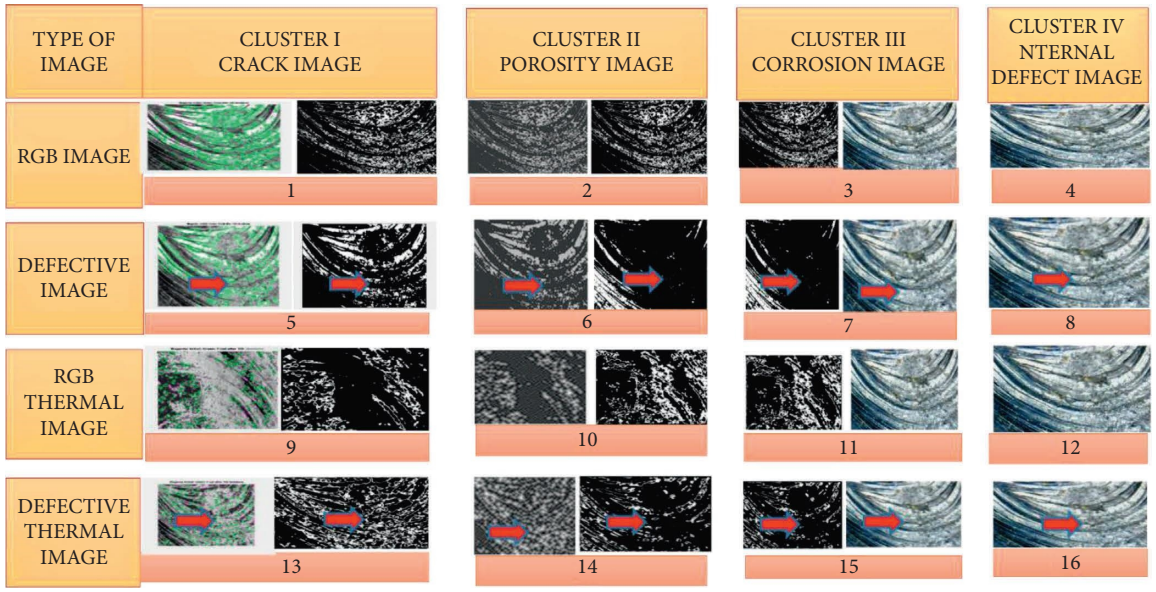

Figure 5: Fuzzy clustering.

probabilities, and finally outputs the best match. Hence, the classification task is completed accurately at a faster rate. The output of the Fuzzy becomes the input to the Deep Learning network. Hence, the Deep Learning network does not have to search for the best match from the universal database but it can search from the fuzzy output. It makes use of ResNet 50 architecture, to perform the classification task. ResNet 50 does the classification by assigning weights or probabilities and determines the best match. It will determine, if the given input image has Porosity, Crack, Corrosion, or Internal defect category. Thus, the classification of defect is perfectly performed by Deep Learning. To enhance the training procedure, a parametric quantity termed center loss is merged with Resnet50.

The center loss function is computed as

$$L_{\text{cen}} = \frac{1}{2}\sum_{i=1}^{N} f(x_i) - c_{yi2}^{2}, \tag{8}$$

where $f(x_i)$ denotes the deep feature, $c_{yi}$is the center of the yth class, and N represents the batch size. The Net Network loss can be obtained by combining softmax loss and center loss:

$$L = L_{cls} + \lambda L_{\text{cen}}, \tag{9}$$

where L_{cls} is softmax loss and λ denotes the weight of center loss. The fuzzification task is performed prior to the application of the concepts of Deep learning, since the role of Fuzzy Algorithm is to simplify the classification task. Deep Learning algorithms are without fuzzy input image then classification accuracy is less. In this case, the Deep Learning algorithm deals with the entire universal collection of images in which the number of images will be more, also there might be irrelevant images being mixed. Deep Learning algorithms perform classification of images from an entire database. Fuzzy algorithms lighten their task by doing the slicing work on the images and then database is given as input for Deep Learning. The Deep Learning algorithms need not analyze the entire collection of images from the universal database, only searches from the selected collection of image database that is rendered by the Fuzzy Algorithm. Hence, this Fuzzy input image lightens the task of the Deep Learning algorithms. After the aid of Fuzzy Algorithm, the Deep Learning algorithms improve the classification time and hence the output is obtained much faster. In addition, since fuzzy has earlier worked on the images and given a select number of images to the Deep learning to perform the classification, there are absolutely no chances of misclassification. Detection and classification of defects that are present in welding thermal images such as Cracks, Porosity, Internaldefects, and Corrosion is the universal collection of image database. This will involve roughly 10,000 images for each type. Hence, Deep Learning algorithms perform the classification task directly from this universal database, which will be tough and will encounter various drawbacks. Hence, to overcome this, we introduced the fuzzy part, which happens prior to Deep learning. This universal collection of Cracks, Porosity, Internal defects, and Corrosion images is fed as input to the Fuzzy block (algorithm). Hence, out of the 10,000 crack images, the Fuzzy Algorithm will filter out and select roughly say 200 relevant images and cluster of crack images. Now, the Deep Learning algorithm will have to work on these 200 selected crack images and perform the best match with the defect that occurred. Similarly, the Fuzzy Algorithm forms clusters for the Porosity, Internal defects, and Corrosion images. Hence, by using Fuzzy Algorithm the output is rendered at a much faster pace and without any misclassification. Figures 7(a) and 7(b) show the denoised crack image and Pixel classified images, respectively. Figures 8(a) and 8(b) show the denoised corrosion image and Pixel classified images, respectively.

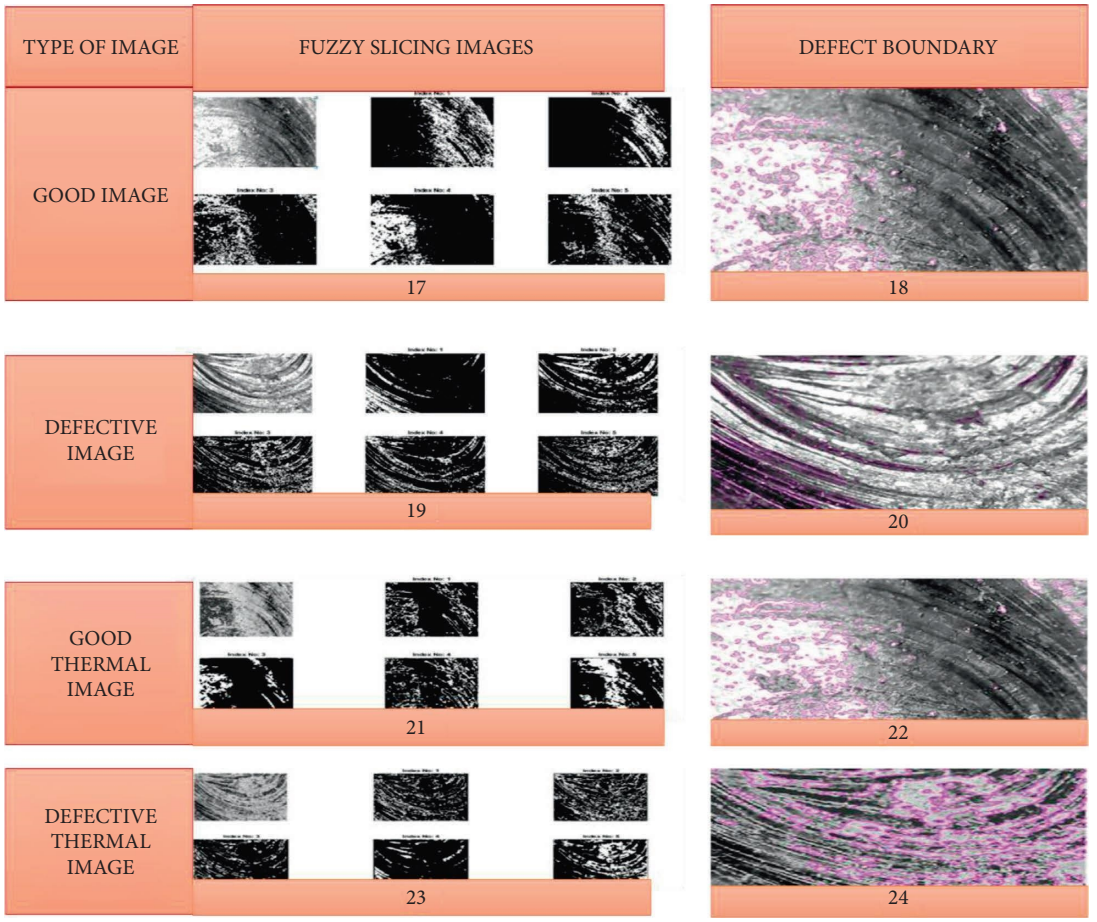

Figure 6: Fuzzy slicing outputs.

4.2. Evaluation Parameters. The efficiency of the proposed technique is verified by utilizing the mentioned parameters in Tables 3 and 4.

4.2.1. Statistical Parameters

(1) True Positive, True Negative, False Positive, and False Negative. A true positive is an effectual operation for prediction of the positive class. Similarly, a true negative is an efficacious method for prediction of the negative class. A false positive is an efficient method for prediction of the false positive class. A false negative is an efficacious operation for prognostication of the false negative class.

(2) Accuracy. Accuracy is the fraction of predictions our method fetched perfectly. Accuracy is given by:

$$\text{Accuracy} = \frac{\text{Number of correct predictions}}{\text{Total no of predictions}}. \tag{10}$$

For binary classification, accuracy is calculated utilizing positives and negatives as given as:

$$\text{Acccuracy} = \frac{(\text{TP} + \text{TN})}{(P + N)}. \tag{11}$$

(3) Precision, Recall. Precision is the count of applicable events among the retrieved events, while Recall (sensitivity) is the count of the total number of applicable events recovered. Precision and Recall depend on an understanding and level of relevance.

$$\begin{aligned} \text{Precision} &= \frac{\text{TP}}{(\text{TP} - \text{FP})}, \\ \text{Recall} &= \frac{\text{TP}}{P}, \\ P &= \text{TP} + \text{FN}, \\ N &= \text{FP} + \text{TN}, \\ \text{FP rate} &= \frac{\text{FP}}{N}, \\ \text{TP rate} &= \frac{\text{TP}}{P}. \end{aligned} \tag{12}$$

The coefficients regard true and false positives, negatives and are applied, even when the classes are of various sizes.

(4) F-measure/F-value. The F_{value} (F-score or F-measure) is a valuation metric for a test's exactitude. To evaluate the score, one views Precision p and Recall r of the test: p is the total

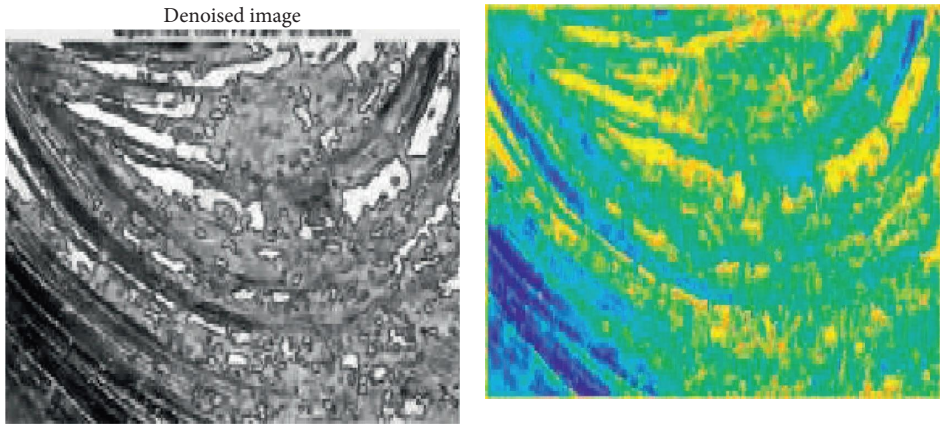

(a) (b)

Figure 7: (a) Denoised crack image. (b) Pixel classified crack image.

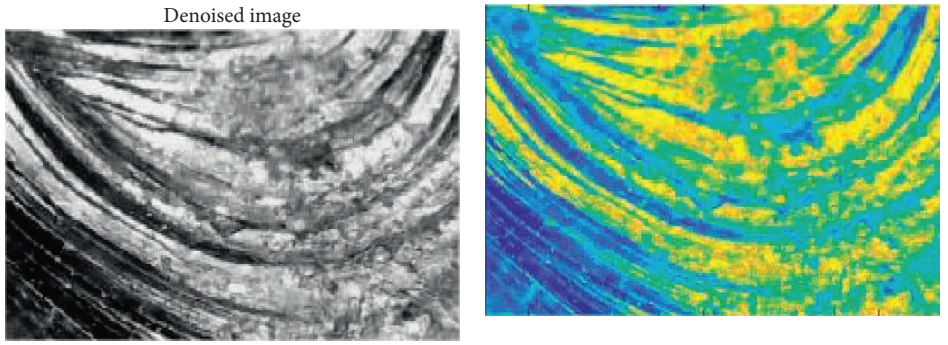

(a) (b)

Figure 8: (a) Denoised corrosion image. (b) Pixel classified corrosion image.

Table 3: Evaluation parameters.

S. No.	Evaluation standards	Fuzzy deep-learning output	
		Pixel classified corrosion image Values	Pixel classified crack image Values
1	Accuracy	0.794	0.8068
2	FN	614	396
3	FP	4020	3952
4	Fprate	0.8627	0.9191
5	Fvalue	0.8814	0.8912
6	Jaccard index	0.788	0.8037
7	MCC	0.1818	0.1301
8	Precision	0.8108	0.8183
9	Recall	0.9656	0.9782
10	TN	640	348
11	TP	17226	17804
12	TPrate	0.9656	0.9782

count of precise positive outcomes fractioned by the total count of positive outcomes the classifier yields and r is the total count of precise positive outcomes fractioned by the total count of all relevant events. The F_1 score is the harmonic average of Precision and Recall, and accomplishes the exact value at 1.

$$F\text{value} = 2 * \left(\frac{\text{precision} * \text{recall}}{\text{precision} + \text{recall}}\right). \tag{13}$$

(5) Mathews Correlation Coefficient (MCC). The MCC is normally a correlation coefficient amidst the observable and predicted binary categorizations, which yield a value ranging

Table 4: Evaluation standards.

S. No.	Parameter	Value
1	MSE	99.41
2	MSE	99.83
3	MSE	107.34
4	PSNR	28.1903302 dB
5	PSNR	28.1722913 dB
6	PSNR	27.8573563 dB
7	SSIM	0.7627
8	LSS	0.0064

from −1 to +1. A coefficient of +1 represents an exact prediction, 0 represents a random prediction, and −1 denotes complete discrepancy between prediction and observation.

$$\mathrm{MCC} = \frac{(\mathrm{TP} * \mathrm{TN} - \mathrm{FP} * \mathrm{FN})}{\sqrt{((\mathrm{TP} + \mathrm{FP}) * (\mathrm{TP} + \mathrm{FN}) * (\mathrm{TN} + \mathrm{FP}) * (\mathrm{TN} + \mathrm{FN}))}}. \tag{14}$$

(6) Jaccard Index. The Jaccard Index, also termed Jaccard similarity coefficient, is a statistical parametric quantity utilized to fetch an in-depth cognition on the similarities within finite sample sets. It is denoted as the intersection of sample sets fractioned by the union of sample sets. The formula for Jaccard Index is as follows.

$$J(A, B) = \frac{|A \cap B|}{A \cup B} = \frac{A \cap B}{|A| + |B| - |A \cap B|}. \tag{15}$$

The Jaccard distance computes dissimilarity within sample sets. The Jaccard distance is got by calculating the Jaccard Index and subtracting from 1, or fractioning the deviations in the intersection of the two sets. Jaccard distance is represented as.

$$D_J = 1 - J(A, B) = \frac{|A \cup B| - |A \cap B|}{A \cup B}. \tag{16}$$

The mean-squared error (MSE) and peak signal-to-noise ratio (PSNR) are employed to ensure the image compression quality. The PSNR ascertains the peak signal-to-noise ratio, in decibels, within two images. This ratio is employed as a quality metric between the original and a compressed image. A higher PSNR value increases the compressed or reconstructed image quality.

$$\mathrm{PSNR} = 10 \log_{10}\left[\frac{R^2}{\mathrm{MSE}}\right], \tag{17}$$

where R is the peak variation in the input image.

Mean-Squared Error (MSE) is the square of differences in the pixel values of the original and compressed images. PSNR represents the measure of peak error. The lesser the MSE value, the lesser the error. What is m, n?

$$\mathrm{MSE} = \frac{1}{\mathrm{MN}} \sum_{M,N} \left[I_1(m, n) - I_2(m, n)\right]^2, \tag{18}$$

where $I_1(m, n)$ is the Original image, $I_2(m, n)$ is the Approximate version, and M, N are the Dimensions of the image.

LSS: LSS descriptors valuate the similarity between images based on matching internal self-similarities. The local "self-similarity descriptor" efficaciously captures the internal self-similarities, valuated enormously over the full image, at different scales, and calculates the local and global geometric aberrations. LSS utilize the detection of objects in images, with no prior knowledge.

5. Conclusion

Fuzzy Deep Learning Algorithm, the output of the Fuzzy Block, is given as input to the Deep Learning block, to simplify the categorization task. The Fuzzy Algorithm performs Slicing operation on the universal collection of image database and renders selective defective images into the Fuzzy image database. Deep Learning Algorithm does not have to classify from the universal image collection and classifies only the selective defective images from the Fuzzy database. This enhances the speed of classification and leads to zero misclassification of defective images. Passive Infrared Thermography's unique feature is that it does not require an external heat source. It rather utilizes the natural infrared radiation coming out of the object. The Dye-Penetrating Test (DPT) outperforms Ultrasonic Testing, in evaluating materials, especially cast iron, through which signals are difficult to be transmitted. If the cast iron Plug valve has a huge grain size, it causes the sound waves to fade, resulting in flaws. The Porosity defects are indicated as closely spaced granules. The Porosity count in a defective thermal image is 72. The clustering results of Cracks, Porosity, Corrosion, and Internal defects are clearly indicated in separate images. The Fuzzy Slicing outputs give details on the slicing operation performed using the index value of $K = 5$. The defect boundary is also indicated as to where exactly is the defect located. The defects are evaluated utilizing parametric quantities such as Precision, Accuracy, Slicing, Jaccard Index, etc. The Parameter values are obtained for each of the 4 defects separately using the corresponding formulas. Hence, this combination of Fuzzy Deep Learning Algorithm renders enhanced efficiency compared to existing algorithms [1].

Data Availability

The data used to support the findings of this study are included within the article.

Conflicts of Interest

The authors declare that they have no conflicts of interest regarding the publication.

References

[1] V. Daniel, A. S. Britto, A. Zimmer, A. L. Koerich, and R. Paludo, "Automatic visual inspection of thermoelectric metal pipes," *Signal, Image and Video Processing*, vol. 13, no. 5, pp. 975–983, 2019.

[2] Z. Zhang, G. Wen, and S. Chen, "Weld image deep learning-based on-line defects detection using convolutional neural

networks for Al alloy in robotic arc welding," *Journal of Manufacturing Processes*, vol. 45, 2019.

[3] S. Chaudhuri, J. Crump, P. A. S. Reed, and B. G. Mellor, "High-resolution 3D weld toe stress analysis and ACPD method for weld toe fatigue crack initiation," *Welding in the World*, vol. 63, no. 6, pp. 1787–1800, 2019.

[4] R. F. Hamade and A. M. R. Baydoun, "Nondestructive detection of defects in friction stir welded lap joints using computed tomography," *Materials & Design*, vol. 162, pp. 10–23, 2019.

[5] M. Jiang, X. Chen, Y. Chen, and W. Tao, "Mitigation of porosity defects in fiber laser welding under low vacuum," *Journal of Materials Processing Technology*, vol. 276, Article ID 116385, 2020.

[6] J. Ye and N. Toyama, "Benchmarking deep learning models for automatic ultrasonic imaging inspection," *IEEE Access*, vol. 9, pp. 36986–36994, 2021.

[7] D. Mery, "Aluminum casting inspection using deep learning: a method based on convolutional neural networks," *Journal of Nondestructive Evaluation*, vol. 39, no. 1, p. 12, 2020.

[8] C. Ajmi, J. Zapata, J. J. Martinez-Alvarez, G. Domenech, and R. Ruiz, "Using deep learning for defect classification on a small weld X-ray image dataset," *Journal of Nondestructive Evaluation*, vol. 39, 2020.

[9] X. Xiao, X. Liu, M. Cheng, and L. Song, "Towards monitoring laser welding process via a coaxial pyrometer," *Journal of Materials Processing Technology*, vol. 277, Article ID 116409, 2020.

[10] K. Schaumberger, M. Beck, J. Saffer et al., "Improving process reliability by means of detection of weld seam irregularities in copper via thermographic process monitoring," *Procedia Manufacturing*, vol. 36, pp. 58–63, 2019.

[11] X. Gao, L. Wang, Z. Chen, Y. Zhang, and D. You, "Process stability analysis and weld formation evaluation during disk laser–mag hybrid welding," *Optics and Lasers in Engineering*, vol. 124, Article ID 105835, 2020.

[12] Z. Lei, B. Li, J. Bi, P. Zhu, W. Lu, and J. Liu, "Influence of the laser thermal effect on the droplet transfer behavior in laser-CMT welding," *Optics & Laser Technology*, vol. 120, Article ID 105728, 2019.

[13] Y. Huang, S. Xu, L. Yang, S. Zhao, Y. liu, and Y. Shi, "Defect detection during laser welding using electrical signals and high-speed photography," *Journal of Materials Processing Technology*, vol. 271, pp. 394–403, 2019.

[14] X. Gao, Y. Li, X. Zhou et al., "Multidirectional magneto-optical imaging system for weld defects inspection," *Optics and Lasers in Engineering*, vol. 124, Article ID 105812, 2020.

[15] X. Xie, Q. Huang, J. Long, Q. Ren, W. Hu, and S. Liu, "A new monitoring method for metal rust removal states in pulsed laser derusting via acoustic emission techniques," *Journal of Materials Processing Technology*, vol. 275, Article ID 116321, 2020.

[16] D. Zhou, J. Liu, Z. Tan, and S. Xu, "Effects of Sn-foil addition on the microstructure and mechanical properties of laser welding joint for dual phase steel and magnesium alloy," *SN Applied Sciences*, vol. 1, no. 7, pp. 694–712, 2019.

[17] Y. R. Choi, S. D. Sun, Q. Liu, M. Brandt, and M. Qian, "Influence of deposition strategy on the microstructure and fatigue properties of laser metal deposited Ti-6Al-4V powder on Ti-6Al-4V substrate," *International Journal of Fatigue*, vol. 130, Article ID 105236, 2020.

[18] D. Bacioiu, G. Melton, M. Papaelias, and R. Shaw, "Automated defect classification of SS304 TIG welding process using visible spectrum camera and machine learning," *NDT & E International*, vol. 107, Article ID 102139, 2019.

[19] U. Shah and X. Liu, "Effects of ultrasonic vibration on resistance spot welding of transformation induced plasticity steel 780 to aluminum alloy AA6061," *Materials & Design*, vol. 182, Article ID 108053, 2019.

[20] N. Nacereddine, A. B. Goumeidane, and D. Ziou, "Unsupervised weld defect classification in radiographic images using multivariate generalized Gaussian mixture model with exact computation of mean and shape parameters," *Computers in Industry*, vol. 108, pp. 132–149, 2019.

[21] J. A. Francis, N. Holtum, S. Olschok et al., "Vacuum laser welding of SA508 steel," *Journal of Materials Processing Technology*, vol. 274, Article ID 116269, 2019.

[22] Y. Zhang, D. You, X. Gao, and S. Katayama, "Online monitoring of welding status based on a DBN model during laser welding," *Engineering*, vol. 5, no. 4, pp. 671–678, 2019.

[23] G. Xu, L. Li, P. Li, Z. Zheng, Q. Hu, and B. Du, "Modeling of keyhole-induced pore formation in laser-arc hybrid welding of aluminum alloy with a horizontal fillet joint," *Journal of Materials Engineering and Performance*, vol. 28, no. 11, pp. 6555–6564, 2019.

[24] J. Y. Son, H. S. Yoon, K. Y. Lee, S. H. Park, and D. S. Shim, "Investigation into high-temperature interfacial strength of heat-resisting alloy deposited by laser melting process," *Metals and Materials International*, vol. 26, no. 3, pp. 384–394, 2019.

[25] U. Reisgen, A. Senger, and S. Olschok, "Electron beam welding in atmosphere of aluminum die casting alloys made of different qualities," *Welding in the World*, vol. 62, no. 6, pp. 1207–1213, 2018.

[26] C. Millon, A. Vanhoye, A. F. Obaton, and J. D. Penot, "Development of laser ultrasonics inspection for online monitoring of additive manufacturing," *Welding in the World*, vol. 62, no. 3, pp. 653–661, 2018.

[27] N. Wu, S. Chen, and J. Xiao, "Wavelet analysis-based expulsion identification in electrode force sensing of resistance spot welding," *Welding in the World*, vol. 62, no. 4, pp. 729–736, 2018.

[28] J. Xie, Y. Ma, W. Xing, L. Zhang, M. Ou, and K. Liu, "Heat-affected zone crack healing in IN939 repaired joints using hot isostatic pressing," *Welding in the World*, vol. 62, no. 3, pp. 471–479, 2018.

[29] Z. Qian, H. Huang, L. Zhao, Q. Ke, and G. Han, "Characterization of spontaneous magnetic signals for residual stress in plasma transferred arc welding process," *Welding in the World*, vol. 63, no. 1, pp. 201–210, 2019.

[30] H. M. Kim, H. R. Yoo, and G. S. Park, "A new design of MFL sensors for self-driving NDT robot to avoid getting stuck in curved underground pipelines," *IEEE Transactions on Magnetics*, vol. 54, no. 11, pp. 1–5, 2018.

[31] W. Hongmin and M. Wang, "Research on detection method of small size weld bead defects based on reluctance measurement," *IEEE Access*, vol. 7, pp. 164068–164079, 2019.

[32] Y. Zhang, X. Gao, D. You, and N. Zhang, "Data-driven detection of laser welding defects based on real-time spectrometer signals," *IEEE Sensors Journal*, vol. 19, no. 20, pp. 9364–9373, 2019.

[33] B. Q. Li and X. Lu, "A biomedical Ti-35Nb-5Ta-7Zr alloy fabricated by powder metallurgy," *Journal of Materials Engineering and Performance*, vol. 28, no. 9, pp. 5616–5624, 2019.

Hindawi
Journal of Engineering
Volume 2023, Article ID 2830575, 11 pages
https://doi.org/10.1155/2023/2830575

Research Article

Experimental Estimation of Energy Absorbed and Impact Strength of Kevlar/Basalt-Epoxy Interwoven Composite Laminate Added with Al_2O_3 Nanoparticles after High-Velocity Bullet Impact

J. Jensin Joshua,[1] **Dalbir Singh**,[1] **P. S. Venkatanarayanan**,[1] **Ch. Sai Snehit**,[1] **A. Bipin Sai Eswar**,[1] **and Melaku Desta**[2]

[1]*School of Aeronautical Sciences, Hindustan Institute of Technology & Science, Chennai, India*
[2]*Department of Mechanical Engineering, College of Electrical and Mechanical Engineering, Addis Ababa Science and Technology University, Addis Ababa, Ethiopia*

Correspondence should be addressed to Melaku Desta; melaku.desta@aastu.edu.et

Received 13 July 2022; Revised 19 August 2022; Accepted 24 November 2022; Published 10 February 2023

Academic Editor: Karthikeyan Sathasivam

The use of composites has increased exponentially in most industries, especially in the aerospace industry; the usage of composites has increased by almost 40% in the last 15 years. Aerospace components are often subject to high-impact loads, so it is important to use impact-resistant materials. Kevlar is known for its high-impact resistance and is commonly used as a fiber with various resins to achieve the desired properties. This paper mainly focuses on weaving Kevlar with basalt fiber in plain weave type by the traditional handloom weaving method. The epoxy resin, along with the harder, is then mixed with the aluminum oxide nanoparticles (Al_2O_3) in different percentages [1%-KB1, 3%-KB2, and 5%-KB3] to form the matrix. The laminate fabricated is then subjected to the high-velocity bullet impact of around 250 m/s. A steel hemispherical head projectile was used in the testing, and it was found to be penetrated through all the specimens making holes. The impact strength for all the different specimens was then estimated by calculating the bullet damage area and energy absorbed. The plate added with 3% Al_2O_3 nanoparticle was found to have improved impact strength when compared with the other two specimens. This plate can be used for bulletproof and other high-velocity impact applications.

1. Introduction

A composite is a mixture of two or more chemically different constituent materials combined macroscopically or microscopically to yield a useful material [1, 2]. It is a mixture of fiber/reinforcement and matrix/resin. Composites are categorized based on the type of fiber and resin being used in the fabrication process; they can be naturally occurring or manmade (synthetic). Some examples of natural composites are wood (which contains cellulose fibers and lignin), bone, granite (which has the particulate type of fiber), and manmade composites are concrete, and plywood. [3]. Macro-fiber composite (MFC) is used for energy applications using unimorph and bimorph cantilever beams [4]. Composites have proven as a good replacement for alloys because of their high stiffness/weight ratio which also helps in fabricating lightweight materials [5, 6]. During the flight take-off, cruise, and landing the aircraft surfaces such as wings, engines, turbines, and nose experience high-velocity impact loadings. One of the major impacts is due to the bird strikes because there will be high relative velocities between the birds and the aircraft [7]. The defense industry also uses composite laminated bulletproof armor to prevent the entry of bullets into the protected area; however, armor with multiple fiber layers was also developed in the past few decades which gives improved penetration resistance for the bullet [8]. Today, composites are thought to have outstanding potential applications as primary load-bearing structures in many industries; therefore, studies on the impact behavior of the composites have attracted a lot of

attention and become a burning research interest in the field of composite materials [9]. Composite structures are open to different load conditions during their useful life. An important requirement for the effective use of composites as a protective structure is resistance to ballistic impact loads from foreign objects. Such applications require a clear understanding of the damage mechanism associated with the conditions under which the projectile penetrates the composite target. Residual strength after ballistic impact is also an important consideration. Impact loads can be divided into three categories: low-speed impact, high-speed impact, and hyperspeed impact. The reason for this classification is that the energy transfer and damage propagation mechanisms between the projectile and the target change dramatically as the speed of the projectile changes. One way to raise the ballistic limit is to use fiber composites [10].

Kevlar has more fascinating properties than other natural and synthetic fibers, resulting in it being in a key position in various load carrier applications. The most significant important property of Kevlar is its high tensile strength-to-weight ratio, which means that when compared to regular material, it has a higher tensile strength at a lower weight [11]. Kevlar fabric has a tensile strength of 3620 MPa (525,000 psi) and a very low relative density of 1.44, which is suitable for ballistics applications where the strength-to-weight ratio is paramount [12]. As a fibrous polymer, Kevlar has been shown to withstand high temperatures. Its tension/tensile strength depletes by 10–20% at elevated temperatures, which continues to fall within a few hours. When Kevlar is molded, the fibers formed have a tensile strength of approximately 3620 MPa and a relative density of 1.44 [13].

Basalt fibers are prepared from basalt rocks which are obtained from volcanic magma that is solidified in the open air after flowing as a hot fluid. The general composition of basalt rocks is, SiO_2 at 51.6–59.3%, Al_2O_3 at 14.6–18.3%, Fe_2O_3 at 9.0–14.0%, and CaO at 5.9–9.4% [13]. Comparing the thermal properties of glass fiber with the thermal properties of basalt fiber, the tensile modulus of basalt fiber is about 60.4 ± 18.9 GPa, and the tensile strength is 568 ± 267 MPa [14]. Basalt has several properties that make it an excellent fiber, such as chemical resistance, heat resistance, low water absorption, and heat insulation. When mixed with other matrices, basalt is a very good reinforcement [15]. The mechanical properties of basalt fiber-reinforced composites have been completely investigated [16–18]. The properties of Kevlar and basalt are given in Table 1.

The properties of Kevlar fiber composites are dominant in the axial to the transverse direction. In order to improve mechanical properties even in the transverse direction, hybridization is considered as the way to construct [19]. The transverse mechanical properties can be improved by weaving with other fibers such as basalt, glass, and carbon. [20]. Recently, basalt fibers have acquired particular importance due to their high compound stability, heat resistance, etc. [21]. The purpose of hybridization is to obtain a better-reinforced structure.

Hybrid composites can contain at least two types of fiber aggregates, helping to integrate the properties of the two materials and reducing costs. 3D textile composites, as shown in Figure 1 [22], are well known for their resistance to ballistic forces.

Table 1: Properties of Kevlar and basalt.

Properties	Kevlar	Basalt
Density (g/cm^3)	1.44	2.66
Tensile modulus (GPa)	124	93
Tensile strength (MPa)	3620	4500
Elastic modulus (GPa)	76	57
Elongation at break (%)	2.0	3.1

The mechanical properties of hybrid composites such as basalt-carbon have been studied under ballistic impact. The results of these experiments demonstrate that the hybridization of basalt with Kevlar fibers significantly improves the performance of reinforced composites [23]. Bandaru and others studied the behavior of Kevlar–basalt composites under low-velocity impact. The basalt sample was found to have the highest peak force, and it was also found that the hybrid samples absorbed more energy than the individual samples [24].

In many studies, researchers have explored traditional fibers such as carbon-based polymer composites, glass, and Kevlar fibers using computational and experimental methods to characterize the properties of composite materials. The energy absorption, ballistic impact performance, and penetrating behavior of these conventional fiber-based polymer composites when subjected to dynamic or impact loads have been investigated. Delamination, fiber-matrix compression damage, matrix cracking, and tensile failure of yarns have been recognized as the primary failure mechanisms under impact load [25].

Therefore, based on all these observations, in this present study, the properties of the basalt hand woven with Kevlar in a plain weaving [1×1] manner composite in fiber form with epoxy resin were investigated. A traditional handloom weaving process is used to hybridize Kevlar and basalt fibers, which, although this is a time-consuming but cost-effective process, can reduce production costs. Due to the attractive mechanical properties, optimum adhesion, strong chemical resistance, and wide range of coatings, epoxy resins are often used in producing polymer-based composites [26].

2. Materials and Methods

2.1. Nanofillers (Al_2O_3). Recent trends demonstrate the use of dispersed nanoparticles in polymers to improve polymer performance, and these composites are called polymer nanocomposites. Various nanofillers such as aluminum, graphene, and titanium, are used as fillers inside polymeric epoxies and other polymers. Compared with pure polymers, polymer-based nanocomposites exhibit unique properties due to their structure. This has led to the widespread use of polymer-based nanocomposites in various engineering fields [27].

The inclusion of different concentrations of alumina nanoparticles (Al_2O_3) into the polymer matrix increased both final stress parameters and percent elongation. The existence of nanoparticles in nanocomposites acts as a bridge

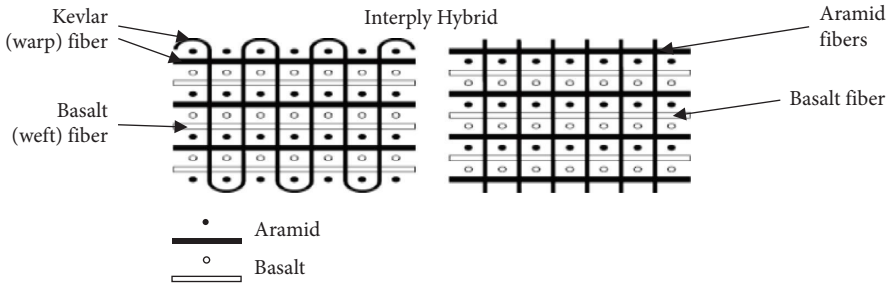

Figure 1: Plain interwoven basalt/aramid hybrid composite [22].

between different polymer molecules to come closer together to build a similarity index between them [28]. Yang et al. [29] proved that the presence of up to 10% (threshold value) by weight of distributed nano-Al_2O_3 particles in the polymer matrix plays an important role in improving the chemical and thermal properties of the nanopolymer composites obtained. According to the study, Al_2O_3 nanofillers improve the mechanical properties, but the hardening effect is gradually reduced for Al_2O_3 content higher than 10% (above a threshold value) by weight. Zhou et al. [30], in their results, found that the thermal conductivity and mechanical properties increased, and the material increased with the addition of 80% alumina nanopowder, but the mechanical properties started to decrease by 55%, i.e., above the threshold value. So, based on all the previous observations, nanoparticles, especially Al_2O_3, are known to increase the mechanical and thermal properties of composites. Therefore, in this study, the nanoalumina powder was chosen as filler in the fabrication of Kevlar/basalt and epoxy composite and examined the subsequent changes in properties. Figure 2 shows the alumina nanoparticles, and Figure 3 shows the processing methods and testing of composites.

Most studies have carried out impact testing for Kevlar/basalt composites, the content of nanoparticles plays a vital role in the mechanical properties of a composite, but this aspect is least bothered, so in this study, nanoalumina powder (Al_2O_3) was added with different percentages into different samples because it can reduce the porosity, and the density of the material increases dramatically with a small percentage of the addition of nanosized alumina particles, tensile strength also increased although there was no difference in the ductility of the material is recorded [31]. The mechanical properties, flexural strength, tensile strength, and Young's modulus or stiffness of the material will be increased. If the alumina content is too low, the intermolecular distances will increase, reducing the impact strength, while if the alumina content is too high, the close stacking of molecules can lead to the fragile property of the material [32].

2.2. Fabrication of Laminate by Weaving. The traditional weaving process takes place on a loom. This process requires two types of yarns or fibers: warp and weft. Here the warp threads are Kevlar, and the weft threads are basalt fibers, the warp running along the length of the fabric, and the weft running across the length of the warp. The woven fabrics are shown in Figure 4.

2.3. Hand Layup Process. The production of a composite laminate is carried out by the traditional hand layup method shown in Figure 5. Epoxy resin and HY951 hardener are used in the fabrication process. Three different laminates are prepared by mixing aluminum oxide nanoparticles in three different percentages viz. 10.6 g of alumina powder, 32 g of alumina powder, and 55 g of alumina powder [1%, 3%, and 5%].

After curing, the resulting composite panels (samples) will have a thickness of 3 mm (which can be achieved by adjusting the thickness of the mold), which is a mandatory requirement for high-speed impact testing, and samples are cut into 150×160 mm. Three test samples were obtained, namely, KB1 (with 10.6 g of alumina powder), KB2 (with 32 g of alumina powder), and KB3 (with 55 g of alumina powder).

2.4. High-Speed Bullet Impact Test. High-speed impact tests are typically performed by a projectile that will be ejected from a high-pressure pneumatic accelerator [33, 34]. A similar configuration was used in this study, and a mild steel hemispherical projectile with details is shown in Table 2. The projectile strikes the composite samples at 200–230 m/s.

The schematic test setup for the bullet (projectile) impact test is shown in Figure 6. Additionally, the high-speed camera was set to an appropriate frame rate to capture several frames at impact. The impact velocities and the residual velocities (velocity of the projectile after striking the specimen) are calculated from the recorded videos with the aid of phantom cine viewer software.

Table 3 shows the different velocities of the projectile before and after impact. It has been observed there is more loss of velocity or energy in KB3. The bullet impact before and after in composite are shown in Figures 7–9.

3. Damage Evaluation of Composite Samples Using Immersion Ultrasonic Testing

Ultrasonic scanning is the most popular nondestructive testing (NDT) technique principally used for flaw detection in different materials such as composites, plastics, and metals. The widely used formats for ultrasonic scanning are A-scan, B-scan, and C-scan [35]. In this work, an ultrasonic C-scan was used since it is the accurate and best method for the detection of impact in composite materials [36].

3.1. Evaluation of Absorbed Energy. The energy drawn up by the composites is given by the following equation [37]:

Figure 2: Alumina powder.

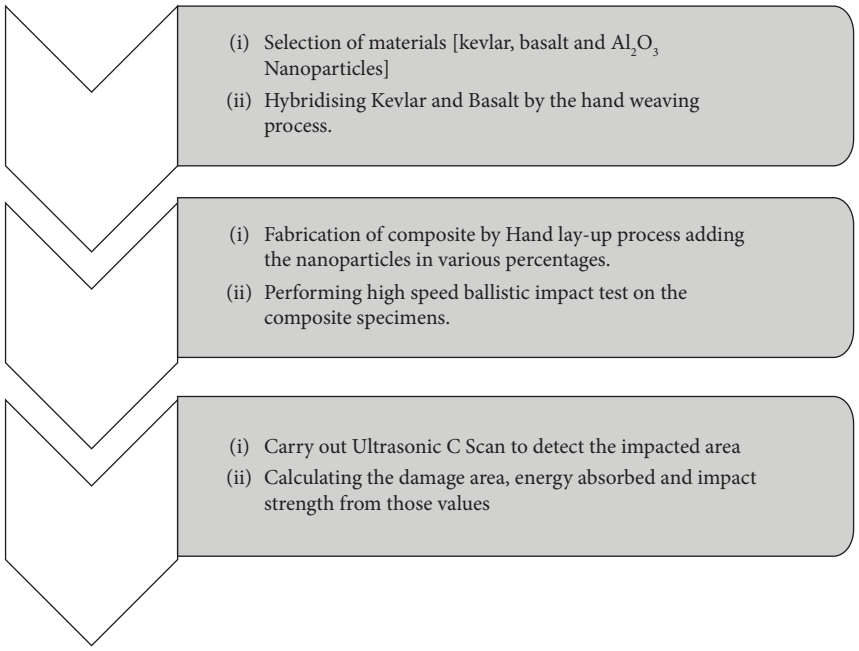

Figure 3: Flow chart for fabrication process and testing of Kevlar/basalt-epoxy interwoven composite.

Figure 4: Woven fiber.

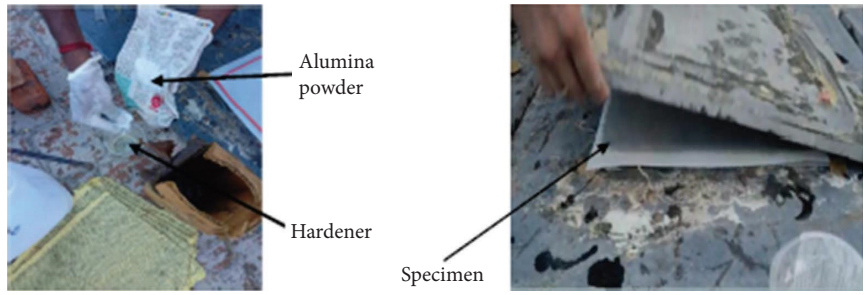

Figure 5: Hand layup process: (a) mixing of hardener and alumina powder and (b) fabricated composite laminates.

Table 2: Details of the projectile.

Parameters	Details
Material	Mild steel
Mass	7.34 (g) or 0.00734 (kg)
Length	15.5 (mm)
Diameter	9.66 (mm)

$$E_{\text{abs}} = 0.5 * m_p * \left(V_i^2 - V_r^2\right), \quad (1)$$

where E_{abs} is the energy absorbed by the composite. m_p is the mass of the projectile or bullet. V_i is the impact velocity of the projectile or bullet. V_r is the residual velocity of the projectile or bullet.

The fiber layers of the composites resist the penetration of the bullet through it converting most of its kinetic energy to absorbed energy [37]. The absorbed energy of composites is presented in Table 4. The values of $V_{\text{i}}$and V_{r} can be obtained from Table 3, and the mass of the projectile is 0.00734 kg (from Table 3). The impact energy is given by equation (2), and the residual energy is given by equation (3).

$$\text{Impact energy} = 0.5 * m_p * V_i^2, \quad (2)$$

$$\text{Residual energy} = 0.5 * m_p * V_r^2. \quad (3)$$

3.2. Calculating Impact Strength of the Composite Specimens. The impact strength of the materials can be calculated by using the following equation [38]:

$$\text{Impact strength} = \frac{(\text{Energy absorbed})}{\text{Damaged area}}. \quad (4)$$

The damaged area can be predicted from ultrasonic-C scan images of the specimens, and the impact area can be calculated with the aid of Image J software.

3.2.1. Ultrasonic-C Scan. This analysis aimed to find out the extent of bullet damage on composite specimens. Two separate tubes for channeling and receiving pulses are spaced equally on opposite faces of the composite sample, as shown in Figure 10. The echoes received from the high-quality region are taken as the threshold value such that the receiver can detect any signal below the threshold value. In general, the pulse energy of damaged regions is small compared with good regions.

The test setup of the Immersion ultrasonic testing system and transmission setup is shown in Figures 11 and 12.

3.2.2. Estimation of Damage Area through C-Scan. The impacted specimen is scanned with ultrasonic C scan nondestructive evaluation to estimate the damaged area. Impact or damaged area can be predicted using Image J software.

The impact strengths of KB1, KB2, and KB3 are 2.75 J/cm^2, 4.28 J/cm^2, and 3.63 J/cm^2, respectively, shown in Table 5 and Figure13. Table 6 shows C-scan, front and back side images of all the samples.

(i) It is evident from the values obtained that the impact strength of KB2 (4.28 J/cm^2) is higher than KB1 (2.75 J/cm^2) and KB3

(ii) In the case of KB1, the addition of alumina powder is very low (i.e., 1% or 10.6 gm); if the alumina content is too low, the intermolecular distances will increase, resulting in the low impact strength [32]

(iii) In the case of KB3, the alumina powder content is very high (i.e. 5% or 55 gm); if the alumina content is too high, the close stacking of molecules can lead to the fragile property of the material, so the impact strength of the specimen is again low

(iv) But in the case of KB2, due to the moderate addition of the alumina powder (i.e., 3% or 32 gm), the resultant impact strength is higher [32, 38]

4. Results and Discussion

(i) After the high-velocity impact test, the results are as follows:

(ii) The bullet impact test revealed that the bullet pierced smoothly through the composite specimens in all three cases

(iii) Delamination, fiber-matrix compression damage, matrix cracking, and tensile failure of yarns have been recognized as the primary failure mechanisms under impact load [25]

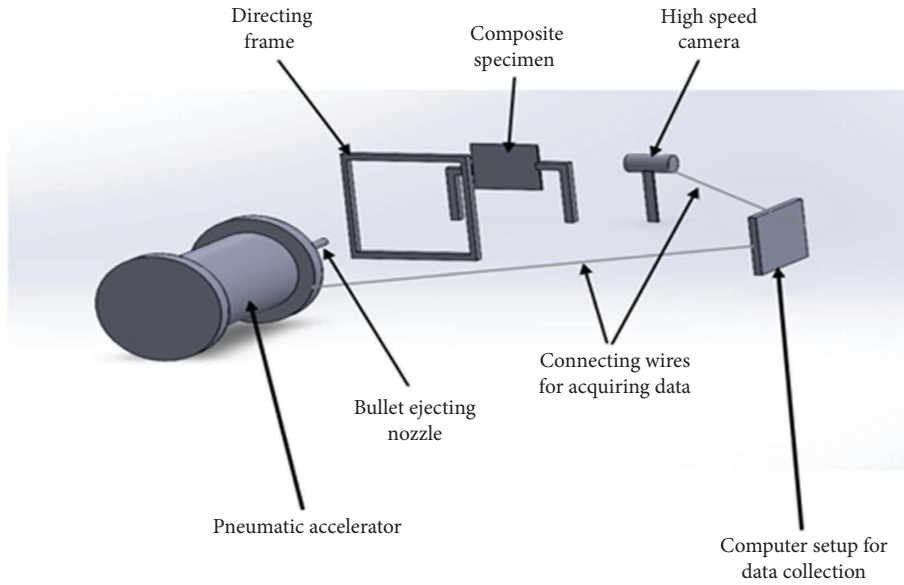

Figure 6: Schematic setup of bullet impact test.

Table 3: Velocities of the projectile.

Material	Average initial impact velocity of projectile (m/s)	Average residual velocity (m/s)
KB1	222.33	206.66
KB2	230	208.33
KB3	224.33	199

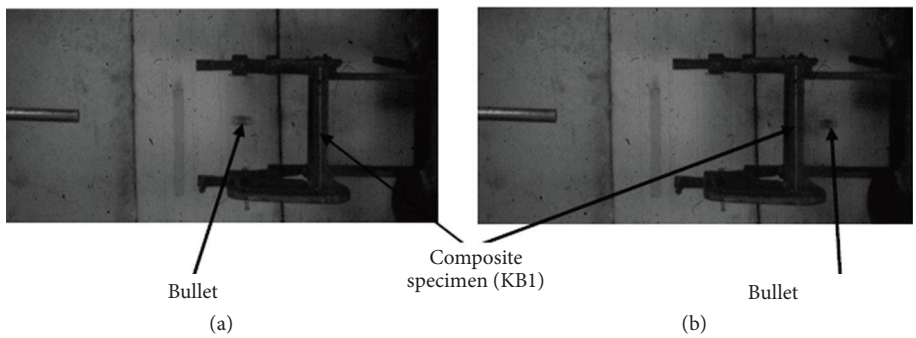

Figure 7: KB1 placed for testing: (a) KB1 before the impact and (b) KB1 bullet after the impact.

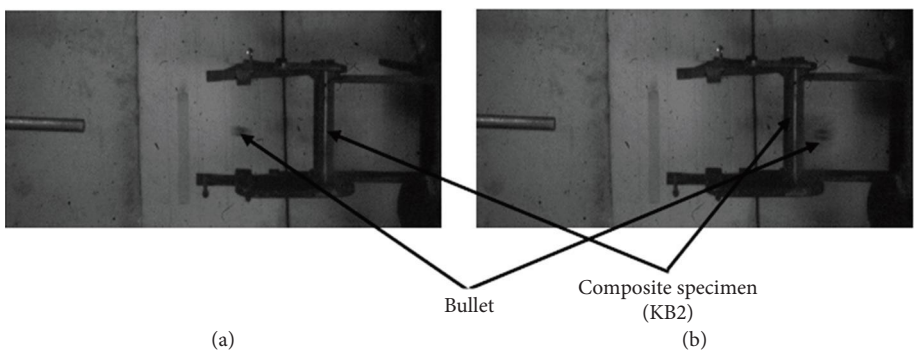

Figure 8: KB2 placed for testing: (a) KB2 before the impact and (b) KB2 bullet after the impact.

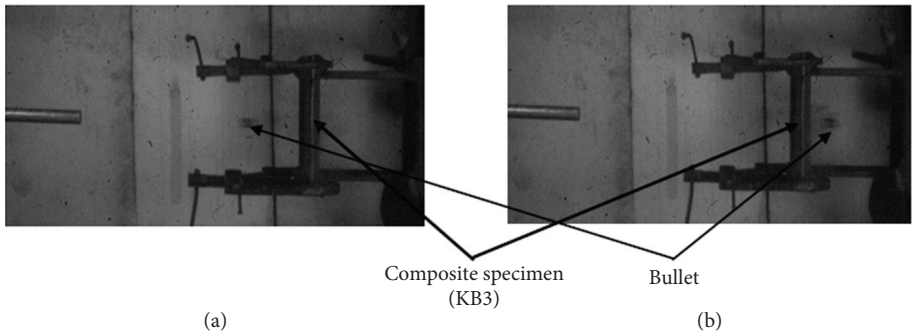

Figure 9: KB3 placed for testing: (a) KB3 before the impact and (b) KB3 bullet after the impact.

Table 4: Absorbed energy of the composite samples.

Material	The impact velocity of projectile (m/s)	Impact energy (J)	The residual velocity of the projectile (m/s)	Residual energy (J)	Absorbed energy (J)
KB1	222.33	181.41	206.66	156.73	24.67
KB2	230	194.14	208.33	159.28	34.85
KB3	224.33	184.68	199	146.8	39.34

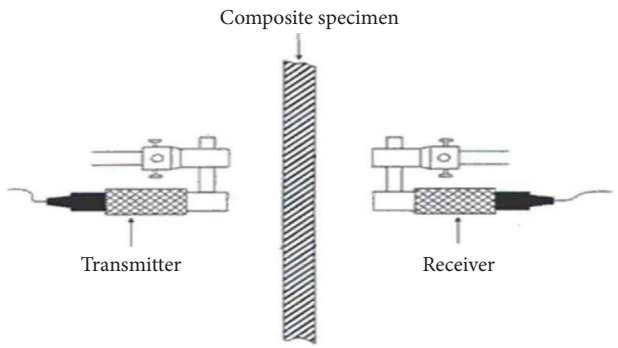

Figure 10: Simplified diagram of the immersion scan system.

Figure 11: Immersion ultrasonic testing system.

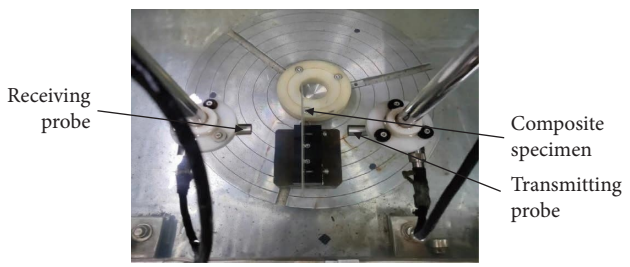

Figure 12: Through transmission setup with the sample.

Table 5: Impact strength of the samples.

Materials	Impact area (cm^2)	Absorbed energy (J)	Impact strength (J/cm^2)
KB1	8.94	24.67	2.75
KB2	8.13	34.85	4.28
KB3	10.82	39.34	3.63

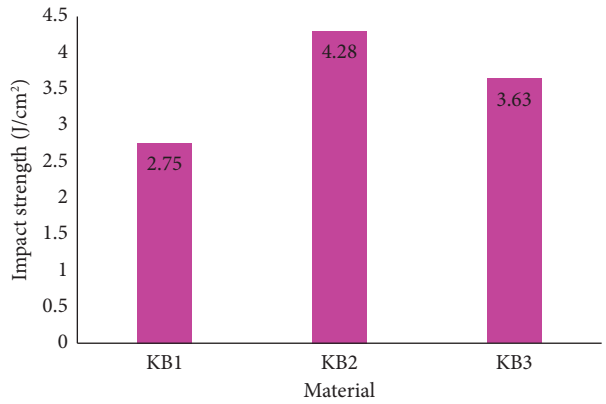

Figure 13: Impact strength vs. composite material.

Table 6: C-scan, front and back side images of all the samples.

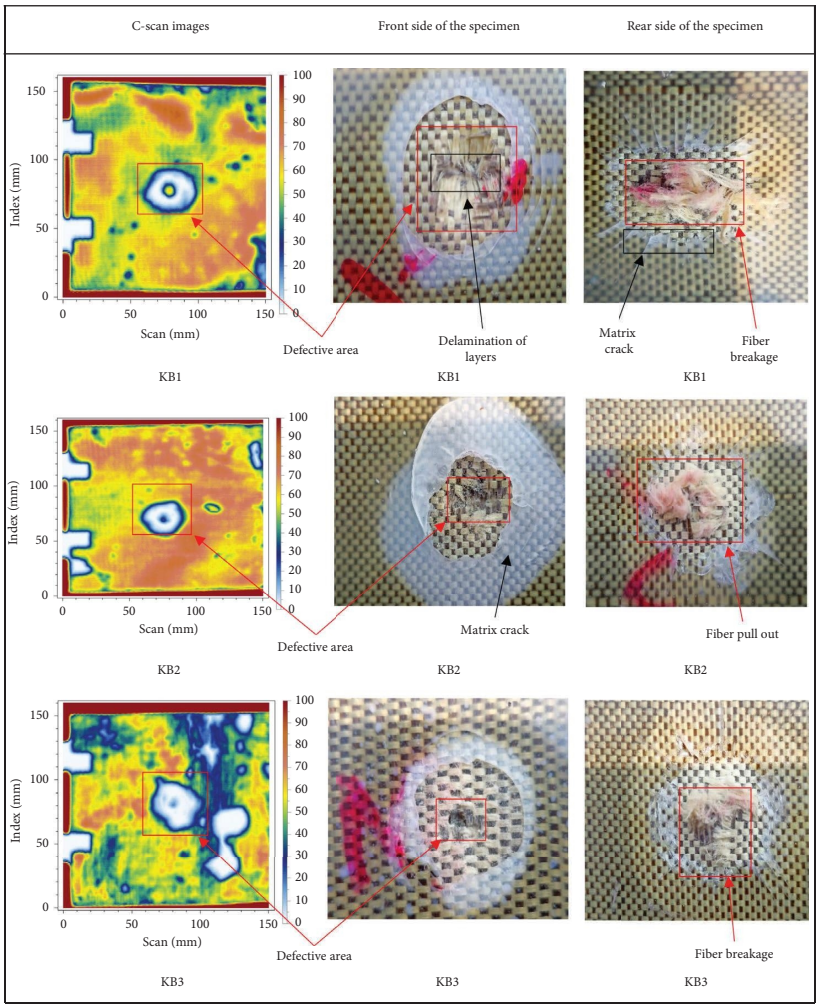

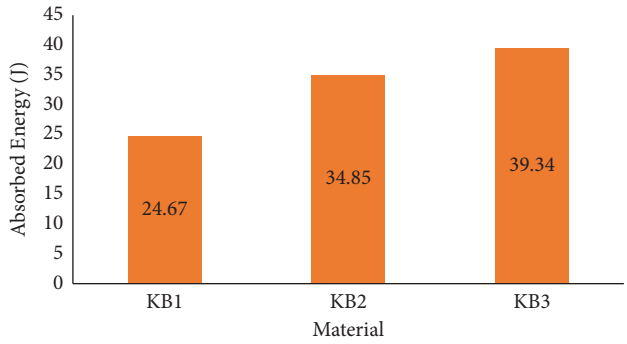

Figure 14: Absorbed energy vs. composite materials.

(iv) Composite failure is due to the high-velocity impact of the projectile, which generates a compression wave through the thickness of the sample and is reflected as a tension wave, causing fiber delamination or detachment between the lamina layers [39]

(v) When the warp and weft threads break in the collision zone, friction between the projectile and target becomes the primary mechanism, continuing to slow the projectile [39]

(vi) The impact area, impact velocity, and residual velocities were predicted using the Image J and Cine viewer software

(vii) Adding nanoparticles to composite materials results in astonishing changes in mechanical properties [25]

(viii) The hybrid samples absorb more energy than individual samples [26]

(ix) It was found that the affected area of KB3 (10.82 cm^2) was larger, i.e., more damaged composite panel; this was because the addition of a higher percentage of alumina powder resulted in a small intermolecular gap resulting in a series of alumina particles in one place causing the epoxy bond to break and lead to brittle nature of the material [32].

(x) As the nanopowder content increases, the impact energy increases, and as the impact energy increases, so does the absorbed energy, so the KB3 (39.34 J) composite sample absorbs more energy than the other two samples, as shown in Figure 14 [20, 41]

(xi) In the case of KB1, the alumina content is too low (1%), so the distance between the molecules is too small, which does not help to create stronger bonds between the epoxy molecules, so the impact strength is reduced [40]

(xii) The impact damage area is low in KB2 (8.13 cm^2) because of the strong polymeric bond, closely packed structure, and the dense nature obtained by adding nanofillers [31, 41]

(xiii) KB2 (4.28 J/cm^2), as shown in Figure 13, gives good impact strength compared to KB1 (2.75 J/cm^2) and KB3 (3.63). The mechanical properties of KB2 got heightened due to the modest content of alumina powder that provided proper dispersion of alumina powder which in turn provided more useable area for epoxy to create a strong bond between the molecules which increases the impact strength of the material [41]

(xiv) The presence of alumina particles gives a connection between the epoxy molecules creating a polymer bond that gives resistance to the impact loads [28]

(xv) The percentage of alumina (3%) present in KB2 helped in overcoming the viscous nature of the epoxy molecules and helped to create a strong polymeric chain that increased the impact strength of the specimen [41]

(xvi) The impact strength increases by two times if the content of alumina powder is moderate (KB2), and the impact strength of the composite starts degrading once the nanopowder volume goes beyond the threshold value (KB3)

(xvii) From the conclusions and results made from [28–31], every material has its threshold value in bearing the nanoalumina powder; the mechanical properties of the material increase up the threshold value and then start gradually decreasing and finally leading to the brittle behavior of the material

(xviii) From the tests performed and the results obtained, it is clear that a high percentage of alumina powder can cause higher content of porosity and dispense of alumina particles, and the formation of microcracks [42]

5. Conclusion

In this work, the effects of different percentages of nanoalumina powder on the impact strength of Kevlar/basalt and epoxy composites were investigated experimentally and numerically. The fiber layers are made with the help of the weaving process, and the fabrication of the composite is performed by the hand layup method. The ballistic study has been carried out to understand the behavior of the Kevlar/basalt polymer composite

with the addition of the alumina nanoparticles. Ultrasonic-C scan was used to find the damage in the subsurface layers and also to find the extent of the damage.

As discussed, the impact area is low in KB2 (8.13 cm^2) compared to KB1 (8.94 cm^2) and KB3 (10.82 cm^2). However, KB3 absorbed more energy (39.34 J) due to the gradual increase of impact strength from the threshold value of alumina powder. As per the results obtained, the impact strength started increasing with the increment of alumina content, and once the percentage increased above the threshold value (i.e., 3% in this study), the mechanical properties started declining. Hence the impact strength is higher in KB2 (4.28 J/cm^2), and less in KB3 (3.63 J/cm^2), and also the impact area is less in KB2 (8.13 cm^2) but more in KB3 (10.82 cm^2), this implies KB2 is more resistant to the high-speed ballistic loads due to the modest content of Al_2O_3 particles.

Several experiments and tests are still being carried out to explore the various benefits of introducing different nanoparticles to composite materials. Therefore, it is not recommended to use too high alumina powder content (above a threshold value) if the aim is to achieve high-impact resistance; a moderate amount of alumina powder can provide high-impact resistance. Alternatively, the woven Kevlar–basalt/epoxy composites can be spiked with other types of nanofillers available in various proportions, and the resulting changes can be investigated after the impact test.

Data Availability

The data used to support the findings of this study are included in the article.

Conflicts of Interest

The authors declare that they have no conflicts of interest regarding the publication.

References

[1] A. Wondimu, M. Kebede, and S. Palani, "Trash pineapple leaf fiber reinforced polymer composite materials for light applications," in *Bio-Fiber Reinforced Composite Materials*-Springer, Singapore, 2022.

[2] Y. Sinshaw, B. SirahbizuY, S. Palani, and U. PrakashJ, "Mechanical property analysis of glass particulates reinforced Aluminum matrix composites," *Materials Today Proceedings*, vol. 62, pp. 488–494, 2022.

[3] S. W. Mekonen, S. Palani, B. Ravi, S. M. Atnaw, M. Desta, and Y. Regassa, "Mechanical properties of Bone particulate and E-glass fiber reinforced hybrid polymer composite," *Advances in Materials Science and Engineering*, vol. 2022, Article ID 5902616, 7 pages, 2022.

[4] M. P. Saravanan, K. Marimuthu, and P. Sivaprakasam, "Modeling and analysis of dynamic structure with macro fiber composite for energy harvesting," *Materials Today Proceedings*, vol. 33, pp. 3481–3485, 2020.

[5] K. Kalai Thendral and D. Abraham Antony, "Ballistic Impact analysis of 2D woven Kevlar/Basalt reinforced composite," *IOP Conference Series: Materials Science and Engineering*, vol. 912, Article ID 052023, 2023.

[6] P. O. Sjoblom, J. T. Hartness, and T. M. Cordell, "On low-velocity impact testing of composite materials," *Journal of Composite Materials*, vol. 22, no. 1, pp. 30–52, 1988.

[7] S. Safri, M. T. H. Sultan, N. Yidris, and F. Mustapha, "Low velocity and high-velocity impact test on composite materials - a review," *International Journal of Engineering Sciences*, vol. 3, pp. 50–60, 2014.

[8] B. Tunaboylu, A. G. Elsabagh, A. K. Sari, and R. Akdeni, "Simulation and experimental tests of ballistic impact on composite laminate armor," *Advances in Materials Science and Engineering*, vol. 2018, Article ID 4696143, 12 pages, 2018.

[9] E. A. Duodu, J. Gu, W. Ding, and S. Tang, "Performance of composite structures subjected to high-velocity impact," *Journal of Researches in Engineering*, vol. 16, no. 4, 2016.

[10] N. K. Naik, "Composite structures under ballistic impact," *Composite Structures*, vol. 66, no. 1–4, pp. 579–590, 2004.

[11] A. N. Nair, S. Sundharesan, and I. S. M. Al Tubi, "Kevlar-based composite material and its applications in body armour: a short literature review," *IOP Conference Series: Materials Science and Engineering*, vol. 987, Article ID 012003, 2003.

[12] R. Stopforth and S. Adali, "Experimental study of bullet-proofing capabilities of kevlar of different weights and number of layers, with 9 mm projectiles," *Defence Technology*, vol. 15, no. 2, pp. 186–192, 2019.

[13] E. Kowsari and J. Hemmat, "Aramid fibers composites to innovative sustainable materials for biomedical applications," *Materials for Biomedical Engineering*, Elsevier, Amsterdam, Netherlands, 2022.

[14] K. Pareek and P. Saha, "Basalt fiber and its composites: an overview," in *Proceedings of the National Conference on Advances in Structural Technologies (CoAST2019)*, Silchar, India, February 2019.

[15] T. Czigány, "Special manufacturing and characteristics of basalt fiber reinforced hybrid polypropylene composites: mechanical properties and acoustic emission study," *Composites Science and Technology*, vol. 66, no. 16, pp. 3210–3220, 2006.

[16] R. Anjabin and H. Khosravi, "Property improvement of a fibrous composite using functionalized carbon nanofibers," *Polymer Composites*, vol. 40, no. 11, pp. 4281–4288, 2019.

[17] N. Jamali, H. Khosravi, A. Rezvani, and E. Tohidlou, "Mechanical properties of multiscale graphene oxide/basalt fiber/epoxy composites," *Fibers and Polymers*, vol. 20, no. 1, pp. 138–146, 2019.

[18] N. Jamali, A. Rezvani, H. Khosravi, and E. Tohidlou, "On the mechanical behavior of basalt fiber/epoxy composites filled with silanized graphene oxide nanoplatelets," *Polymer Composites*, vol. 39, no. S4, Article ID E2472, 2018.

[19] Y. Swolfs, R. M. McMeeking, I. Verpoest, and L. Gorbatikh, "The effect of fibre dispersion on initial failure strain and cluster development in unidirectional carbon/glass hybrid composites," *Composites Part A: Applied Science and Manufacturing*, vol. 69, pp. 279–287, 2015.

[20] M. R. Karamooz, H. Rahmani, and H. Khosravi, "Hybrid effects of basalt and kevlar fibers on low-velocity impact behavior of epoxy-based composites," *Fibers and Polymers*, vol. 21, no. 11, pp. 2590–2598, 2020.

[21] V. Lopresto, C. Leone, and I. De Iorio, "Mechanical characterisation of basalt fibre reinforced plastic," *Composites Part B: Engineering*, vol. 42, no. 4, pp. 717–723, 2011.

[22] A. Kunal Singha, "Short review on basalt fiber," *International Journal of Textile Science*, vol. 1, no. 4, pp. 19–28, 2012.

[23] J. Tirillò, L. Ferrante, F. Sarasini et al., "High velocity impact behaviour of hybrid basalt-carbon/epoxy composites," *Composite Structures*, vol. 168, pp. 305–312, 2017.

[24] A. K. Bandaru, S. Patel, Y. Sachan, R. Alagirusamy, N. Bhatnagar, and S. Ahmad, "Low velocity impact response of 3D angle-interlock Kevlar/basalt reinforced polypropylene composites," *Materials & Design*, vol. 105, pp. 323–332, 2016.

[25] A. Chaurasia, R. S. Mulik, and A. Parashar, "Polymer-based nanocomposites for impact loading: a review," *Mechanics of Advanced Materials and Structures*, vol. 29, 2021.

[26] X. Zhao, S. Lu, W. Li et al., *Epoxy as Filler or Matrix for Polymer Composites*, IntechOpen, London, UK, 2022.

[27] V. Mahesh, D. Harursampath, and V. Mahesh, "An experimental study on ballistic impact response of jute reinforced polyethylene glycol and nano silica based shear thickening fluid composite," *Defence Technology*, vol. 18, 2022.

[28] R. Mukherjee and S. De, "Adsorptive removal of nitrate from aqueous solution by polyacrylonitrile–alumina nanoparticle mixed matrix hollow-fiber membrane," *Journal of Membrane Science*, vol. 466, pp. 281–292, 2014.

[29] C.-C. Yang, S.-J. Chiu, W.-C. Chien, and S.-S. Chiu, "Quaternized poly(vinyl alcohol)/alumina composite polymer membranes for alkaline direct methanol fuel cells," *Journal of Power Sources*, vol. 195, no. 8, pp. 2212–2219, 2010.

[30] W. Zhou, S. Qi, C. Tu, H. Zhao, C. Wang, and J. Kou, "Effect of the particle size of Al2O3 on the properties of filled heat-conductive silicone rubber," *Journal of Applied Polymer Science*, vol. 104, no. 2, pp. 1312–1318, 2007.

[31] B. Sadeghi, M. Shamanian, F. Ashrafizadeh, P. Cavaliere, and A. Rizzo, "Influence of Al2O3 nanoparticles on microstructure and strengthening mechanism of Al-based nanocomposites produced via spark plasma sintering," *Journal of Materials Engineering and Performance*, vol. 26, 2022.

[32] S. Mallakpour and E. Khadem, "Recent development in the synthesis of polymer nanocomposites based on nano-alumina," *Progress in Polymer Science*, vol. 51, pp. 74–93, 2015.

[33] J. P. Johnston, J. M. Pereira, C. R. Ruggeri, and G. D. Roberts, "High-speed infrared thermal imaging during ballistic impact of triaxially braided composites," *Journal of Composite Materials*, vol. 52, 2022.

[34] A. Amirian, H. Rahmani, and H. Moeinkhah, "An experimental and numerical study of epoxy-based Kevlar-basalt hybrid composites under high velocity impact," *Journal of Industrial Textiles*, vol. 51, pp. 804S–821S, 2021.

[35] M. F. Raiminor Ramzi, F. M. Mahmod, and A. B. Elmi, "Immersion ultrasonic inspection system for small scaled composite specimen," *Journal of Engineering and Applied Sciences*, vol. 10, no. 22, 2022.

[36] S. Arhamnamazi, N. Bani, N. B. M. Arab, A. R. Oskouei, and F. Aymerich, "Accuracy assessment of ultrasonic C-scan and X-ray radiography methods for impact damage detection in glass fiber reinforced polyester composites," *Journal of Applied and Computational Mechanics*, vol. 5, 2018.

[37] V. Mahesh, S. Joladarashi, and S. M. Kulkarni, "Damage mechanics and energy absorption capabilities of natural fiber reinforced elastomeric based bio composite for sacrificial structural applications," *Defence Technology*, vol. 17, no. 1, pp. 161–176, 2021.

[38] M. Moyo, K. Kanny, and R. Velmurugan, "Performance of kenaf non-woven mat/PLA biocomposites under medium velocity impact," *Fibers and Polymers*, vol. 21, no. 11, pp. 2642–2651, 2020.

[39] A. K. Bandaru, V. V. Chavan, S. Ahmad, R. Alagirusamy, and N. Bhatnagar, "Ballistic impact response of kevlar reinforced thermoplastic composite armors," *International Journal of Impact Engineering*, vol. 89, pp. 1–13, 2016.

[40] S. Zhang, X. Y. Cao, Y. M. Ma, Y. C. Ke, J. K. Zhang, and F. S. Wang, "The effects of particle size and content on the thermal conductivity and mechanical properties of Al2O3/high density polyethylene (HDPE) composites," *Express Polymer Letters*, vol. 5, no. 7, pp. 581–590, 2011.

[41] In-Y. Jeon and J.-B. Baek, "Nanocomposites derived from polymers and inorganic nanoparticles," *Materials*, vol. 3, no. 6, pp. 3654–3674, 2010.

[42] N. Srivastava and G. P. Chaudhari, "Microstructural evolution and mechanical behavior of ultrasonically synthesized Al6061-nano alumina composites," *Materials Science and Engineering A*, vol. 724, pp. 199–207, 2018.

Hindawi
Journal of Engineering
Volume 2022, Article ID 3669584, 5 pages
https://doi.org/10.1155/2022/3669584

Research Article

Influence of SiC/TiB_2 Particles Addition on Corrosion Behavior of As-Cast Zn-Al-Cu Alloy Hybrid Composites

Rohinikumar Chebolu,[1] **Ramanaiah Nallu**,[1] **Ratnam Chanamala**,[1] **Surender Kumar Sharma**,[2] **and Ramesh Rudrapati**[3]

[1]*Dept. of Mechanical Engineering, A.U. College of Engineering, Andhra University, Visakhapatnam, Andhra Pradesh 530003, India*
[2]*PP & EMD, BARC, Visakhapatnam, Andhra Pradesh 531011, India*
[3]*Department of Mechanical Engineering, Bulehora University, Bule Hora, Ethiopia*

Correspondence should be addressed to Rohinikumar Chebolu; rohinikumar.rs@andhrauniversity.edu.in and Ramesh Rudrapati; rameshrudrapati@gmail.com

Received 28 June 2022; Accepted 28 July 2022; Published 17 August 2022

Academic Editor: Karthikeyan Sathasivam

In this work, the silicon carbide (SiC) and titanium diboride (TiB_2) reinforced as-cast Zn-Al-Cu alloy-based hybrid composites were produced with ultrasonic-assisted stir casting. The corrosion behavior of as-cast Zn-Al-Cu/TiB_2/SiC hybrid composites with varying 0, 5, 10, and 15 weight percent of SiC + TiB_2 particulates in Zn-Al-Cu matrix alloy was investigated in this study, The effect of additional reinforcements content on the corrosion behavior of hybrid composites with respect to Zn-Al-Cu alloy was investigated. The corrosion rate of hybrid composites was taken by using potentiodynamic polarization equipment (with 3.5 wt.% NaCl solution). The potentiodynamic polarization test findings showed that the hybrid composites' uniform and localized corrosion resistances were enhanced by the addition of dual reinforcements. As the weight fraction of the SiC/TiB_2 reinforcement increases, weak microgalvanic cells that form between the constituent phases of the fabricated as-cast Zn-Al-Cu hybrid composites weaken, improving their resistance to uniform and localized corrosion. The results revealed that the corrosion rate values were reduced to 28.88% at 15% of reinforcement when compared to the base alloy.

1. Introduction

The hybrid composites outperform typical metal matrix composites in terms of mechanical and functional performance which suits to be widely adopted in structural engineering and functional device applications[1]. With a larger reinforcement content, typical MMCs reinforced with fibers or micron particles can attain ultrahigh strength and improved elastic modulus [2, 3]. But due to the inverse relationship between strength and ductility, toughness and ductility dropped dramatically with increased reinforcement volume [4]. The addition of nano-reinforcements to metal matrix alloys can enhance strength and elastic modulus without sacrificing ductility and toughness [5, 6]. Furthermore, the nano-reinforcements have a far higher strength-to-weight ratio than their micron-sized counterparts. However, due to the influence of strong Vander Waals forces and the intrinsic incompatibility of nano-reinforcements with more metal matrix alloys, uniform dispersion in MMCs with more volume% nano-reinforcements is extremely challenging [4]. Therefore, a limited number of nano-reinforcements in nanocomposites (MMNCs) of most metal matrixes showed less increment in strength, which restricted their usage in the engineering and biomedical fields [4]. A great deal of research has been done to help MMCs overcome these difficulties.

Hybrid reinforcing is a distinct and significant technology in the design and fabrication of progressive MMCs. This technique's main principle is to introduce a variety of hybrid reinforcements into a metal matrix and rely on the hybrid reinforcements to demonstrate their potential

benefits to achieve synergistic effects that result in excellent overall performance. When compared to the bioinspired structures, the hybrid reinforcement method is more advantageous and appealing for the production of a substantial amount of MMCs because it is based on the selection of the most suitable type, content, and ratio of hybrid reinforcements to achieve excellence. Thus, the existing practices for fabrication of MMCs are also broadly applicable to the producing hybrid MMCs. As a result, the evolution of hybrid composites has the great potential to make a significant contribution to expansion of the range of applications for MMCs.

Zinc-aluminum alloys have grown tremendously in recent years, for applications like bearings, as it provides advantages over other standard materials [7, 8]. The Zn27Al alloy, in particular, is a member of the zinc-aluminum alloy family. It has a wide range of applications. In response, it competes with materials made of bronze, copper, aluminum, and iron [6]. Many structural applications continue to rely on Zn-Al-based composites [9]. As a matrix, Zn-Al alloys are noted for their excellent combo of physical, mechanical, and technical characteristics [10–12]. Generally, metal matrix alloys (MMCs) are preferred for bearing applications that require lightweight, good durability, advanced strength at high temperatures, and corrosion resistance. At this point, hybrid composites are very useful in the industry, especially automotive and aerospace, due to their numerous good properties because it has the content of at least two reinforcement materials inside them.

Furthermore, according to the findings of recent investigations, the isotropic features of MMCs are improved by the addition of reinforcing particles. Even though there are different processes for making composite materials reinforced with particles, stir casting is the most common method for producing hybrid MMCs. Stir casting in the making of hybrid MMCs has a number of advantages including low cost, simplicity, and the ability to disperse the particulates that serve as reinforcement in hybrid MMCs throughout the matrix material [13]. However, because particles can easily agglomerate in the composite material, dispersion alone is insufficient to acquire the essential attributes of hybrid MMCs.

Corrosion can variously impact metal matrix composites, depending on their composition and the surrounding environment. The corrosion resistance of Al-based materials must be studied, particularly for their extensive usage in automotive and aerospace applications [14]. In general, uniform corrosion is observed in zinc-aluminum alloys [8]. A passive layer is formed on the metal surface of ZA alloys in the as-cast condition, which prevents further corrosion attacks from occurring [15]. This passive layer provides adequate corrosion resistance for the majority of atmospheric environments. And also, this alloy exhibits high resistance to corrosion in the natural environment, waters, and soils as a result of the ability of zinc to form a protective layer on the surface primarily of corrosive products containing zinc oxide, simonkolleite, zinc hydroxide, or their mixtures. Additional corrosion protection needs to be considered in more aggressive environments, such as marine environments.

The corrosion behavior of MMCs in different environments where the material is likely to be exposed is an important factor in selecting the appropriate material for a particular application [16]. It follows from the literature that limited work has been done to study the corrosive behavior of MMCs. Although, some studies on the corrosive behavior of MMCs have shown that they are more susceptible to attack than related nonreinforced alloys [8].

Numerous factors influence the corrosion behavior of MMCs, including the alloy composition and reinforcing particles used, as well as their distribution and size in the matrix, the fabrication technique used to make them, and the nature of the interface between reinforcement and the matrix [16, 17].

Even a relatively minor change in any one of these elements can have a significant impact on the corrosion behavior of the material. The major challenge with the usage of particles in metal alloys for various applications is the effect of reinforcement on corrosion resistance of that particular metal alloy. The incorporation of a reinforcing phase could result in irregularities or defects in the protective layer that forms on the alloy surface to counteract the effect of corrosion, by increasing the number of sites for initiation of corrosion and making the composite vulnerable to severe attack. There have been several investigations on the microstructural, tribological, and mechanical properties of the ZA27 composites using reinforcement materials. However, there have been few investigations into the corrosion behavior of ZA27 composites including nanoparticles. The main objective of this research was carried out to investigate the impact of reinforcing SiC and TiB_2 particles on the corrosion behavior of the as-cast Zn-Al-Cu alloy.

2. Constituents and Approaches

2.1. Matrix. "The base material for this experiment is an as-cast Zn-Al-Cu alloy. The dimensions of the rectangular ingots are $150 \times 150 \times 25$ mm and are cast by the process of liquid metallurgy in accordance with the ASTM B669-82 standard. Zinc has a purity of 99.90 percent, aluminum has a purity of 99.98 percent, and copper has a purity of 99.00 percent. In a crucible, aluminum and copper were placed and heated to 650 degrees Celsius, and then, zinc is added. The degassing agent C_2Cl_6 was also added after the stirring process was done for 5 minutes. During the duration of this technique, grain refining was not made" [18] (Table 1).

2.2. Reinforcement. Silicon carbide and titanium diboride, which are available commercial ceramic particles with average particle sizes of 20 microns and 30 microns, respectively, and with 99.00% purity, were procured from Sigma-Aldrich in India. Table 2 contains information about ceramic particles, including their sizes and shapes.

2.3. Preparation of the Composites. The alloy was placed into the graphite crucible for 15 minutes and heated to 680°C. Hexafluoro titanate salt (K_2TiF_6) with 2.7 weight percent was

Table 1: The chemical constitution of as-cast Zn-Al-Cu alloy.

Material	Zn	Al	Cu	Act
Constitution (wt.%)	Balance	25–28	2.0–2.4	0.01-0.02

Table 2: Properties of the reinforcements.

Reinforcement	Density (g/cc)	Melting point (°C)	Young's modulus (GPa)	Tensile strength (MPa)
SiC	3.21	2730	137	625
TiB_2	4.52	2970	575	754

added to improve the wettability of the molten alloy. X wt% SiC + TiB_2 ($X = 0$, 5, 10, and 15) particles were incorporated into the molten form of the alloy. Before administering the particulate ceramics to the molten form of alloy, the ceramic particles are heated to 800°C and sustained at that temperature for one hour. "A mechanical stirrer operating at 85 rpm was used to mix the molten alloy, and the rotational velocities were maintained for 15 minutes at the same level to guarantee that the composite was of proper composition. The titanium alloy ultrasonic probe was immersed in the molten slurry to a depth of 3/4 of the molten slurry's height in the crucible" [19].

Sonication was carried out at a frequency of 20 kHz using ultrasonic processing. A 22-minute ultrasonic energy pulse was used to disperse the grouped reinforcements. Following the sonication procedure, the graphite crucible was removed from the furnace and the molten hybrid metal matrix composite was poured into an MS mold.

By using the Wire Cut EDM (WEDM) machine composite samples were generated for testing as per ASTM standards. Table 3 lists the materials and their composition of the as-cast samples, as well as the designations that will be utilized throughout this study.

2.4. Corrosion Test. The composite specimens were tested under a potentiodynamic polarization test in an aerated 3.5 percent NaCl solution with the pH adjusted to a value of 10 using potassium hydroxide pellets. The pitting corrosion behavior of produced composite specimens with varying vol % of reinforcement was studied using an electrochemical system (Gill-AC). Experiments were carried out on a polished surface with a 1 cm^2 exposure area and a 0.166 mV/sec potential scan rate from −250 mV initial potential to the final pitting potential. The corrosion potential (Ecorr) was defined from the resulted graphs. Specimens with a higher positive Ecorr (or a lower negative Ecorr) were thought to be less vulnerable to pitting corrosion.

3. Results and Discussion

3.1. Corrosion Behavior of As-Cast Zn-Al-Cu Hybrid Composites. When compared to corrosion of an unreinforced matrix alloy, the presence of reinforcing particles, as well as the processing associated with MMCs manufacturing, can cause severe corrosion of the metal matrix. As a result, it is important to sustain a rate and a type of corrosion that will not be significantly damaging to the characteristics

Table 3: Wt.% of the composite samples.

S. no	As-cast Zn-Al-Cu alloy (wt%)	TiB_2 (wt.%)	SiC (wt.%)
1	100	0	0
2	95	2.5	2.5
3	80	5	5
4	85	7.5	7.5

of the MMC during its intended life span. For hybrid composites, the distribution and content of reinforcement powders in the matrix alloy are critical parameters. Pitting and crevice corrosion susceptibility, as well as other types of corrosion, are normally determined by exposure testing or electrochemical test methods on metal matrix composites (MMCs).

Generally, electrochemical test methods show the passive properties of one MMC compared to another and provide understanding of the mechanisms that can cause corrosion. In this work, potentiodynamic curves generated by the potentiodynamic polarization test are used to study the pitting corrosion behavior of the hybrid composite samples. Ecorr, Icorr, and corrosion rate (mpy) values are obtained using the Tafel extrapolation method (Table 4). These values clearly show that the corrosion rate of as-cast Zn-Al-Cu alloy (without any reinforcement) was more than any other composite used in this study. If we examine the corrosion rate trend concerning the vol% of reinforcement, it gradually decreases by increasing the vol% of reinforcement. It is a well-known fact that the addition of SiC as reinforcement can increase corrosion resistance due to SiC plays a significant role as a physical barrier to the initiation and formation of pits [17]. It may be attributed to the inert nature of SiC as a ceramic material. And the formation of Al_3C_4 which is mainly responsible for corrosion attack can be avoided by processing temperatures less than 710 C, which is also the reason for increment in the corrosion resistance in the presence of TiB_2 (Table 4) [3, 17, 20]. Especially, the addition of SiC resulted in a significant difference in the corrosion rate of the composites, as SiC ceramic particles do not react with molten aluminum, which prevents the development of brittle intermetallics at the reinforcements-matrix interfaces [21].

Hybrid composite with 15% reinforcement resulted in better corrosion resistance than as-cast Zn-Al-Cu and with 5% and 10%. As SiC can form a passive layer readily, the presence of SiC may assist actively in the passivity of hybrid composite which resulted in improved corrosion resistance.

Table 4: The corrosion data of the as-cast Zn-Al-Cu and its hybrid composites.

Composites	E_{corr} (mV)	I_{corr} (mA/cm^2)	Corrosion rate (mm/year)
ZA27	−1050	2.388	367
ZA27 + 2.5% TiB_2 + 2.5% SiC	−984	2.320	334
ZA27 + 5% TiB_2 + 5% SiC	−906	1.814	297
ZA27 + 7.5% TiB_2 + 7.5% SiC	−867	1.314	261

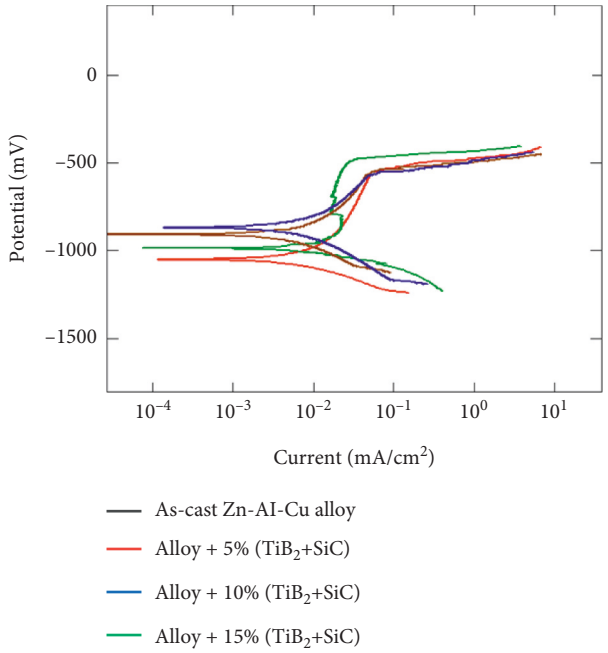

Figure 1: Potentiodynamic polarization curves of the as-cast Zn-Al-Cu and hybrid composites.

15% of TiB_2 + SiC hybrid composite resulted in overall better corrosion resistance than any other sample used in this study. Generally, grain boundaries are more prone to corrosion attack in Zn alloys, as SiC covers most of the region at grain boundaries, inert nature (as a ceramic material) of SiC and acting as nucleating sites for passive layer formation may lead to the enhanced corrosion resistance [17]. The presence of TiB_2 and SiC can decrease the gradient of potential difference between the Zn-Al-Cu matrix and SiC which is responsible for galvanic corrosion in the case of only Al and SiC, which may be the reason for better corrosion resistance which is evident in Figure 1 [22, 23].

4. Conclusions

Zn-Al-Cu with 7.5% TiB_2+ 7.5% SiC resulted in overall better corrosion resistance than other samples in this study and also showed better value than as-cast Zn-Al-Cu alloy

The potentiodynamic polarization curves clearly show that hybrid composite with increasing wt.% of reinforcement has better corrosion resistance

The addition of SiC has a major impact on the improved corrosion resistance of Zn-Al-Cu/15% TiB_2 + SiC hybrid composite due to its inert nature and active participation in the formation of the passive layer

Due to the addition of dual reinforcements to Zn-Al-Cu matrix alloy gives excellent resistance, no corrosion-related pits could be noticed on the corrosion surfaces. Only a variety of tiny microcracks, depending on the size of the reinforcing particles, were visible on the surfaces.

Data Availability

The data used to support the findings of this study are included within the article.

Conflicts of Interest

The authors declare that they have no conflicts of interest.

Acknowledgments

The authors sincerely thank the authorities of Weld Lab, PP&EMD, for permitting to conduct the experiment and support extended by Dr. S. K. Sharma, Scientific Officer-G, PP&EMD, BARC, Visakhapatnam, India, for their valuable guidance and encouragement in publishing this article.

References

[1] G. Pitchayyapillai, P. Seenikannan, K. Raja, and K. Chandrasekaran, "Al6061 hybrid metal matrix composite reinforced with alumina and molybdenum disulphide," *Advances in Materials Science and Engineering*, vol. 2016, Article ID 6127624, 9 pages, 2016.

[2] M. V. Krishna and A. M. Xavior, "An investigation on the mechanical properties of hybrid metal matrix composites," *Procedia Engineering*, vol. 97, pp. 918–924, 2014.

[3] K. P. S. S. K. Umanath, K. Palanikumar, and S. T. Selvamani, "Analysis of dry sliding wear behaviour of Al6061/SiC/Al2O3 hybrid metal matrix composites," *Composites Part B: Engineering*, vol. 53, pp. 159–168, 2013.

[4] M. Y. Zhou, L. B. Ren, L. L. Fan et al., "Progress in research on hybrid metal matrix composites," *Journal of Alloys and Compounds*, vol. 838, Article ID 155274, 2020.

[5] E. D. Yalçın, A. Çanakçı, F. A. T. İ. H. Erdemir, H. Çuvalcı, and A. H. Karabacak, "Enhancement of wear and corrosion resistance of ZA27/nanographene composites produced by powder metallurgy," *Arabian Journal for Science and Engineering*, vol. 44, no. 2, pp. 1437–1445, 2019.

[6] O. Güler, F. Erdemir, M. Çelebi, H. Çuvalcı, and A. Çanakçı, "Effect of nano alumina content on corrosion behavior and microstructure of Za27/graphite/alumina hybrid nanocomposites," *Results in Physics*, vol. 15, Article ID 102700, 2019.

[7] S. S. Owoeye, D. O. Folorunso, B. Oji, and S. G. Borisade, "Zinc-aluminum (ZA-27)-based metal matrix composites: a review article of synthesis, reinforcement, microstructural, mechanical, and corrosion characteristics," *International Journal of Advanced Manufacturing Technology*, vol. 100, no. 1-4, pp. 373–380, 2019.

[8] B. Bobić, S. Mitrović, M. Babić, and I. Bobić, "Corrosion of aluminium and zinc-aluminium alloys based metal-matrix composites," *Tribology in industry*, vol. 31, no. 3&4, p. 44, 2009.

[9] O. Güler, M. Çelebı, R. Dalmış, A. Çanakçi, and H. Çuvalci, "Novel ZA27/B4C/graphite hybrid nanocomposite-bearing materials with enhanced wear and corrosion resistance," *Metallurgical and Materials Transactions A*, vol. 51, no. 9, pp. 4632–4646, 2020.

[10] K. K. Alaneme, B. O. Fatile, and J. O. Borode, "Mechanical and corrosion behaviour of Zn-27Al based composites reinforced with groundnut shell ash and silicon carbide," *Tribology in Industry*, vol. 36, no. 2, p. 195, 2014.

[11] K. K. Alaneme, S. I. Adama, and S. R. Oke, "Mechanical properties and corrosion behaviour of Zn-27Al based composites reinforced with silicon carbide and bamboo leaf ash," *LEJPT*, vol. 25, pp. 58–71, 2014.

[12] K. K. Alaneme, O. A. Ajibuwa, I. E. Kolawole, and A. V. Fajemisin, "Mechanical, corrosion and wear behaviour of steel chips and graphite reinforced Zn-27Al alloy based composites," *Acta Metallurgica Slovaca*, vol. 23, no. 2, pp. 171–181, 2017.

[13] S. O. Akinwamide, B. T. Abe, O. J. Akinribide, B. A. Obadele, and P. A. Olubambi, "Characterization of microstructure, mechanical properties and corrosion response of aluminium-based composites fabricated via casting—a review," *International Journal of Advanced Manufacturing Technology*, vol. 109, no. 3-4, pp. 975–991, 2020.

[14] H. V. Jayaprakash, M. K. Veeraiah, and P. V. Krupakara, "Studies of ZA-27/Red mud metal matrix composites with respect to corrosion properties," *Materials Today Proceedings*, vol. 5, no. 5, pp. 12956–12962, 2018.

[15] A. E. Ares, L. M. Gassa, and C. M. Mendez, "Corrosion Resistance of Directionally Solidified Casting Zinc-Aluminum Matrix," *Corrosion resistance*, pp. 35–54, 2012.

[16] S. C. Sharma, D. R. Somashekar, and B. M. Satish, "A note on the corrosion characterisation of ZA-27/zircon particulate composites in acidic medium," *Journal of Materials Processing Technology*, vol. 118, no. 1-3, pp. 62–64, 2001.

[17] H. M. Zakaria, "Microstructural and corrosion behavior of Al/SiC metal matrix composites," *Ain Shams Engineering Journal*, vol. 5, no. 3, pp. 831–838, 2014.

[18] R. Chebolu, R. Nallu, and R. Chanamala, "Effect of TiB_2 on trıbologıcal propertıes of as-cast Zn-Al-Cu/SiC composıtes usıng taguchi and ANOVA technıques," *Composites Theory and Practice*, vol. 2, pp. 79–86, 2022.

[19] R. Chebolu, R. Nallu, and R. Chanamala, "Experimental investigation on mechanical behavior of as cast Zn-Al-Cu/SiC/TiB_2 hybrid metal matrix composite by ultrasonic assisted stir casting technique," *Engineering Research Express*, vol. 4, no. 2, Article ID 025040, 2022.

[20] M. O. Bodunrin, K. K. Alaneme, and L. H. Chown, "Aluminium matrix hybrid composites: a review of reinforcement philosophies; mechanical, corrosion and tribological characteristics," *Journal of Materials Research and Technology*, vol. 4, no. 4, pp. 434–445, 2015.

[21] S. J. James, K. Venkatesan, P. Kuppan, and R. Ramanujam, "Comparative study of composites reinforced with SiC and TiB2," *Procedia Engineering*, vol. 97, pp. 1012–1017, 2014.

[22] M. Schneider, K. Kremmer, C. Lämmel, K. Sempf, and M. Herrmann, "Galvanic corrosion of metal/ceramic coupling," *Corrosion Science*, vol. 80, pp. 191–196, 2014.

[23] P. Senthil Kumar, V. Kavimani, K. Soorya Prakash, V. Murali Krishna, and G. Shanthos Kumar, "Effect of TiB2 on the corrosion resistance behavior of in situ Al composites," *International Journal of Metalcasting*, vol. 14, no. 1, pp. 84–91, 2020.

Hindawi
Journal of Engineering
Volume 2022, Article ID 4274436, 8 pages
https://doi.org/10.1155/2022/4274436

Research Article

An Investigation of the Dielectric Properties of Barium Oxide: Therm500 Nanofluids at Different Temperatures

P. Prakash,[1] J. Catherine Grace John,[2] A. Kingson Solomon Jeevaraj ,[1] and Belete Tessema Asfaw [3]

[1]*Department of Physics, LRG Government Arts College for Women, Tirupur 641604, Tamilnadu, India*
[2]*Department of Mathematics, Karunya Institute of Technology and Sciences, Coimbatore 641114, Tamilnadu, India*
[3]*Department of Chemical Engineering, Haramaya Institute of Technology, Haramaya University, Haramaya, Ethiopia*

Correspondence should be addressed to A. Kingson Solomon Jeevaraj; drkingson.a@gmail.com and Belete Tessema Asfaw; belete.tessema@haramaya.edu.et

Received 3 June 2022; Revised 27 June 2022; Accepted 9 July 2022; Published 17 August 2022

Academic Editor: Karthikeyan Sathasivam

The dielectric characteristics of barium oxide: Therm500 nanofluids were investigated at a static frequency in this study. Barium oxide: Therm500 nanofluids are made by dispersing barium oxide nanoparticles in Therm500 (base fluid) using a sonicator. The static dielectric measurements were made with a frequency domain reflectometry (FDR) sensor. At various temperatures, the values of several dielectric properties, including dipole moment (μ), molar polarization (P), excess dielectric constant (ε^E), static dielectric constant (ε^O), and excess dipole moment (μ^E), have been measured for BaO: Therm500 nanofluids. Kirkwood factor and Bruggman factor were also computed and presented. The fluctuations in dielectric properties concerning six distinct combinations including 0.001 grams, 0.002 grams, 0.003 grams, 0.004 grams, 0.005 grams, and 0.006 g of nanofluid systems and four different temperatures such as 300 K, 303 K, 313 K, and 323 K are investigated in terms of intermolecular interactions. At all temperatures, the abovementioned dielectric properties BaO: Therm500 nanofluids are positive-negative variations across the whole combination range suggesting in nanofluids the existence of molecular interactions. Synchronization in both parallel and antiparallel of the dipoles in the fluid's mixture are verified by the Kirkwood factor. The Bruggman factor depicts the divergence from the linear relationship in nanofluids, indicating molecular interactions. Dielectric properties of BaO: Therm500 are being studied to understand better their physical, technical, chemical, industrial, laboratory, biological, and pharmaceutical applications.

1. Introduction

The dielectric constant is a material's ability to increase a condenser's capacitance. The dielectric constant is governed by the molecule's permanent dipole moments and its polarizability in terms of structure. The ease with which the electron density of a molecule can be altered is called polarizability. The dielectric constant rises as the dipole moment and polarizability rise. The formation and composition of complexes in nanofluids containing various numbers of nanoparticle molecules are determined using dielectric measurements [1, 2]. Researchers have been intrigued by the dielectric behaviour of polar and non-polar substances, as well as their combinations, at various combinations and temperatures. Merely only a few researchers, however, have used dielectric properties to investigate the molecular interactions of nanofluids [3, 4].

Dielectric studies have become increasingly important in understanding the interplay of the components in recent years. The other dipole moment in numerous H-bonded complexes was explained using the polarization effect, charge transfer effect, and proton transfer impact. Poor H-bonding can be caused by poor interaction between electrostatic charges. No chemical approach can detect such low-energy hydrogen bonding. As revealed by Sivakumar and Kumar, even weak interactions can be detected in dielectric investigations [5]. They understood the intermolecular interactions induced by dipole-dipole contact and

H-bonding. These investigations allow for the provision of precise data on the fluids and their mixtures' chemical mechanics. Dipole-dipole, H-bondingrams, molecular associations, and dipole-induced dipole contact are some of the molecular interactions between components in particle-fluid mixtures [6]. These interactions lead to variations in the dielectric constant and its optimum behaviour. Excessive dielectric constants serve as a definition for these aberrations. Numerous papers [7–10] provide experimental information on excess dielectric constants, Kirkwood correlation factor, and Bruggman factor for a variety of binary and ternary fluid mixes. Conclusions on how systems deviate from the behaviour of an ideal mixture may be drawn from their study.

The intermolecular interaction found in diverse particle-fluid mixes determines the thermophysical properties of nanofluids, such as density [11], dielectric constant [12], and refractive index [13]. The dielectric constant and dipole moment deviate from their ideal behaviour due to these interactions [14]. The well-known method for analyzing molecule interactions in fluids uses physical features such as dielectric factors [15]. Therefore, various dielectric factors relating to the intermolecular and intramolecular connection and rotation with temperature fluctuation must be studied to understand molecules' structural behaviour.

It is well accepted that the thermophysical characteristics of fluid systems, including density, viscosity, dielectric constant, and refractive index, are directly correlated with the molecular interactions found in various binary fluid combinations. We learn crucial information about intermolecular interactions and structure from how these qualities vary with composition [16]. Dielectric parameters, refractive index, and thermodynamic parameters do not vary linearly whenever a particle-fluid solution is produced. The deviation of these parameters from linearity is referred to as excess parameters. It helps understand the nature of particle and fluid bonding [2]. Dielectric fluids' properties and physical processes have lately sparked a rush of interest [17]. The underlying difficulties are volume-induced particle contacts and actions in fluids, connected with the dielectric features of these fluids.

The dielectric constant is known as a feature of solvent systems utilized to characterize the electrical components of materials [17]. Excess thermodynamic characteristics have become popular in the study of chemical thermodynamics. Thus, physicists and electrical engineers rarely employ them. As a result, we are looking for a spot in the region of binary dielectrics where excess dielectric permittivity can exist. Fundamental information about molecular interactions and molecular process mechanisms can be gleaned from the frequency-dependent dielectric behaviour of fluid mixtures. For example, the dielectric constant of mixed solvents is necessary for pharmaceutical and analytical sciences to forecast a drug's solubility and chemical stability [18, 19].

Therm500 is an H-bond fluid with a vital dipole moment. Research [20–22] on several binary liquid systems' dielectric and excess dielectric characteristics is essential in chemical and electrochemical operations. Therm500 dielectric constant enables exact conductometry and potentiodynamic polarization measurements [23]. Glycols have lower boiling points than non-polar molecules of the same molecular weight and more incredible boiling points than hydrocarbons of identical mass. Glycols interact more strongly with electron-withdrawing groups in a component than with other molecules. Glycols are bioorganic solvents that are among the essential reagents in organic synthesis. The dielectric constant of mixed solvents nanofluids containing amines is being investigated to understand better its biological, chemical, pharmacological, technical, and laboratory uses [24].

The present study of BaO: Therm500 nanofluids were generated by ultrasonic dispersion. The two-step process is often used to prepare nanofluids and is the most cost-effective way to produce nanofluids on a big scale. The two-step methodology is used in the current work. This procedure involved dispersing pure, synthesized BaO nanoparticles in base fluids (Therm500). Simple mixing is ineffective in producing stable nanofluids, which is the main issue in the formulation of these fluids. Hence, an ultrasonic processor is used in the current work to achieve that goal. This strategy for increasing reaction rate has become a standard synthetic technique for many homogeneous and heterogeneous chemical processes [25]. Their ultrasonic and several dielectric properties such as dipole moment (μ), molar polarization (P), excess dielectric constant (ε^E), static dielectric constant (ε^O), excess dipole moment (μ^E), Kirkwood factor, and Bruggman factor were measured with aid of particle volume (0.001–0.006 g) and temperature (300–323 K), and molecular interaction was investigated.

2. Experimental Section

2.1. Materials Used. The compounds employed in the research are of evolutional spectroscopic grade and consist of a purity of 99.99%. They were utilized without additional purification. BaO nanoparticles were first produced utilizing an ultrasonic aided chemical precipitation technique [26]. Then BaO: Therm500 nanofluids are made using the following procedure: To achieve uniform BaO nanoparticle dispersion in the Therm500 fluid, first weigh the BaO with an accuracy of 0.1 mg using a digital electronic mass balance (model: AY220, SHIMADZU), then mix the BaO nanoparticles with the weighed Therm500, and finally sonicate the mixture continuously for 30 minutes with a cup horn sonicator. A combination without sonication processing has a less uniform and unstable dispersion than the generated nanofluids with sonication processing. In this research, six different concentrations of the synthesized Bao nanoparticles (0.001 g, 0.002 g, 0.003 g, 0.004 g, 0.005 g, and 0.006 g) were combined with the specified amount of base fluids (Therm500). The suspension of the nanofluids was then improved and made more stable by intense ultrasonication using a cup horn sonicator for 30 minutes at a working frequency of 20 kHz and a 100% output amplitude (Hielscher UP400S). To keep the temperature of the suspension consistent, the sonication was carried out in an ice bath. For dispersing the aggregated nanoparticles, the sonication period is a crucial factor. After conducting

multiple experiments, 30 minutes was ultimately chosen for this study's sonication period. In order to prevent nanoparticle agglomeration and to create a well-dispersed, stable solution, ultrasonication was one of the dispersion techniques utilized. Venlub Petro Products (P) Ltd., Chennai, Tamil Nadu, India, provided the base fluid Therm500. "Chemical composition varies across heat transfer fluids and thermal oils. Polyglycol and water-glycol fluids, silicone-based greases, and oils are examples of manufactured goods. They are made up of alkaline organic and inorganic chemicals and are employed in the diluted form at combinations ranging from 3% to 10%. Petroleum or mineral oils, as well as water, make up non-synthetic goods. Synthetic fluids are more expensive than non-synthetic fluids, but they perform better in fire resistance and cooling. Semi-synthetic fluids have a cost and heat transfer performance halfway between synthetic and soluble oil fluids. Non-flammable compounds containing carbon, chlorine, and fluorine are chlorofluorocarbons (CFCs). This category includes halogenated fluorocarbon (HFC), halogenated chlorofluorocarbon (HCFC), and perfluorocarbon (PFC) fluids" [27].

A water-bath-based temperature control system was used to maintain a 1°C precision level. The sample cell is enclosed in a heat-insulating container, and water is circulated through it at a constant temperature because of a temperature-controlling mechanism. For cells with fluids as the dielectric medium (Cs), the capacitance of the cell can be expressed as the ratio of its capacitance in the air at a certain temperature to that in fluid (Co).

A dipole metre was used to measure the dielectric properties (Mittal Enterprises, New Delhi). Two stainless steel round discs (25 mm in diameter) make up the dielectric cell. Using specific processes, the faces are painstakingly carved and highly polished. The electricity is routed through a specially designed top with a BNC connector that directly corresponds to the two plates of a capacitor at a distance of around 3 mm. An integrated circuit in the function generator allows it to create high-quality sine waveforms with exceptional precision and stability.

For determining the fluid's static dielectric constants, a sensor was utilized. It is based on the same principle as the FDR method basically. Power provides a 100 MHz frequency signal to the sensor. In order to form an electromagnetic field, the pulse is sent to two stainless steel rods. It is possible to measure the dielectric constant with this method because the field travels quickly through the fluids, leading to consistent voltage output. The average of the five tests was used to calculate the dielectric constant. An accuracy of 5% was achieved in the measurement of the dielectric constant.

Benzene is used for reference liquid. To measure the air capacitance of the cell (C_o), the capacitance of benzene (C_r), and the capacitance fluid whose dielectric constant must be calculated, the dielectric constant of an unknown fluid (x) may be estimated using the relationship (C_x).

$$\varepsilon_X = 1 + \left(\frac{C_o - C_X}{C_o - C_R}\right)(\varepsilon_R - 1), \quad (1)$$

where ε_x– unknown fluid dielectric constant, ε_R– reference fluid dielectric constant, C_O– air capacitance, C_X– unknown fluid capacitance, and C_R– reference fluid capacitance.

The reference liquid dielectric constant (benzene = 2.26) is denoted by ε_r. As an oscillator, a one-of-a-kind function-generating semi-conductor is employed. When the data of the resistor (R) and capacitor (C) change, the frequency of an oscillation changes. As a result, the oscillator's frequency changes. The oscillator's frequency may be used to compute the cell's capacitance and, as a result, the medium's dielectric constant.

2.2. Stability of Nanofluids, Particle Size, and pH Value. Suspension stability is a critical issue in both scientific study and practical applications. The reasonably long stability of nanofluids and their stability in real-world applications should be prioritized. HFC, HCFC, and PFC were used to increase the stability of BaO: Therm500 nanofluids without adding surfactants in this study. So far, the strategies for improving the stability of nanofluids have only been reported to be stable for a few days or a few months [28]. But, in this study, over the course of a month, it was discovered that the suspensions of BaO: Therm500 were stable, and there was no discernible sedimentation. In the future study, an effective and easy strategy for maintaining the long-term stability of BaO: Therm500 nanofluids will be obtained by modifying the surface characteristics of suspended nanoparticles. It suppresses the formation of nanoparticle clusters to generate a stable and homogeneous suspension by adding various surfactant types. Surfactant effects of thermal conductivity measurements of BaO: Therm500 nanofluids were also investigated. In nanofluids, the particle size of nanoparticles is critical for improving heat conductivity and stability. The pH value of the nanofluids also affects their stability. Therm500 nanofluids' size and pH values can be modified in the future to optimize particle size and pH values for increased BaO [29].

2.3. Dielectric Parameters Measurements of Bao: Therm500 Nanofluids. According to dielectric constant values, the derived dielectric parameters are listed below.

2.4. Excess Dielectric Constant (ε^E). ε^E indicates the nature of intermolecular interactions and the strength of fluids [30]. It is defined as follows:

$$\varepsilon^E = \varepsilon_{12} - (\varepsilon_1 X_1 + \varepsilon_2 X_2), \quad (2)$$

where ε_{12} is the nanofluid dielectric constant; ε_1 and ε_2 are the base fluids and nanoparticles dielectric constants, respectively; and X_1 and X_2 are the molar fractions of base fluids and nanoparticles, respectively.

2.5. Dipole Moment (μ). For calculating μ of nanofluids, the Kirkwood factor [31, 32] is also useful. Equation (3) has been used by Kumbharkhane et al. [33–35] to examine the

direction of electric dipoles in fluids. The following is an example of an equation that was employed:

$$\mu^2 = \frac{27\,KTM_2}{4\pi N_A d_1}\left(\frac{a_0 - a_\infty}{(\varepsilon_{01}+2)^2}\right), \tag{3}$$

where μ^2 is the nanofluid's dipole moment, K is the Boltzmann's constant, T is the temperature, M_2 is the nanoparticles molecular weight, N_A is the Avogadro's number, d_1 be the solvent density, ε_{01} be the base fluid static dielectric constant, and a_0 and a_∞ are the static dielectric constant and optical dielectric constant, respectively. Deviation from unity in an ideal fluid mixing might imply an interaction between the two fluid components.

2.6. Excess Dipole Moment (μ^E). The expression of μ^E is

$$\mu^E = \mu_m - (\mu_A X_A + \mu_B X_B), \tag{4}$$

where μ_m be nanofluid mixtures dipole moment; μ_A and μ_B are the base fluids dipole moments and nanoparticles dipole moments, respectively; and X_A and X_B are the base fluids mole fractions and nanoparticles mole fractions, respectively.

2.7. Molar Polarization (P_{12}). The molar polarization (P_{12}) of nanofluid mixes had been measured using the Clausius–Mosotti equation that states

$$P_{12} = \left(\frac{\varepsilon - 1}{\varepsilon + 2}\right)\frac{M_1 f_1 + M_2 f_2}{d_{12}}, \tag{5}$$

where ε be the nanofluid systems dielectric constant; f_1 and f_2 are the constituent's molar combinations and the nanofluid mixtures molar combinations, respectively; M_1 and M_2 are the base fluids molecular weight and nanoparticles molecular weight, respectively; and d_{12} is the density of the nanofluid mixtures.

2.8. Static Dielectric Constant (ε^0). As the first proof of molecular interactions in nanofluids, the Bruggman mixing formula [36–40] may be applied. The non-linearity of the Bruggman formula best illustrates how solute-solvent interactions change the effective volume of the solute. The Bruggman mixing formula with a volume proportion of nanoparticles is connected to the dielectric constant (0) of nanofluids, which reveals the interaction between fluids and particles. The Bruggman factor f_B and V are predicted to have a non-linear connection according to equation (6). In nanofluids, this non-linear relationship reveals molecular interaction [41]. The volume fraction of particles (V) may be connected to static dielectric permittivity (ε_{sm}), nanoparticles (ε_{sA}), and fluids (ε_{sB}), which displays the interaction between fluids and particles in the mixture as follows:

$$f_B = \left(\frac{\varepsilon_{sm} - \varepsilon_{sB}}{\varepsilon_{sA} - \varepsilon_{sB}}\right)\left(\frac{\varepsilon_{sA}}{\varepsilon_{sm}}\right)^{1/3} = 1 - V. \tag{6}$$

3. Result and Discussion

3.1. Static Dielectric Constant (ε^0). Figure 1 depicts the fluctuations in ε^0 with BaO: Therm500 nanofluid combination at four different temperatures (300 K, 303 K, 313 K, and 323 K). Figure 1 of BaO: Therm500 nanofluids indicates that ε_0 data vary slightly with a rise in all combinations at all four temperatures (300 K, 303 K, 313 K, and 323 K). The creation of solid contacts in the BaO: Therm500 nanofluid system is responsible for the rise in ε_0 data at a combination of 0.006 g. The number of molecules of BaO present in the BaO: Therm500 nanofluids generates a good shape for the strong interaction at a combination of 0.006 g of BaO nanoparticles. However, the addition of additional BaO disrupts the favorable structure at higher combinations. Therm500 fluids' dielectric constant rises as a direct function of molecule length [42]. Dipole orientation is caused by molecule rotation and intermolecular motion.

When the temperature and the volume fraction of BaO both rise, the dielectric permittivity falls. The orientation of the permanent dipoles is affected by high thermal motion, resulting in a fast reduction in orientation polarization. The reduction in dielectric permittivity as the volume fraction of BaO nanoparticles increases. It might be attributable to the rise in the number of carbon atoms.

This trend might be explained by a decline in the molar volume of the spinning molecule as the number of dipoles in the nanofluid mixture decreases [43]. Figure 1 shows that the static dielectric constant values of BaO: Therm500 nanofluids rise as the combination of BaO nanoparticles increases. The field and dipole alignment move from parallel to antiparallel as a result of this occurrence [44]. Therm500 and BaO have longer chains, making it difficult for the molecules to rotate. In contrast, the static dielectric constant value of BaO: Therm500 nanofluids rises as all five temperatures rise (300 K, 303 K, 313 K, and 323 K).

3.2. Dipole Moment (μ). The dipole moment of BaO: Therm500 nanofluids is shown in Table 1 for six distinct combinations (0.001 grams, 0.002 grams, 0.003 grams, 0.004 grams, 0.005 grams, and 0.006 g) and four different temperatures (300 K, 303 K, 313 K, and 323 K). Except for a combination of 0.003 grams, there is only a minor variance in the dipole moment values for all combinations and temperatures. The shape, configuration, and interfacial charge of molecular entities all influence their (μ). The variation in (μ) of Bao: Therm500 nanofluids with increasing temperature indicates the presence of the Therm500 interaction, whereas no change in (μ) with temperature rises indicates that lack of BaO: Therm500 nanofluids association.

Figure 1 shows the Kirkwood factor (g_{eff}) measurements for various combinations and temperatures of BaO: Therm500 nanofluids examined. At 300 K and over the whole volume fraction range, the $g_{eff} > 1$ shows that the dipole pairs in the mixture have formed in a parallel orientation. However, the $g_{eff} < 1$ over the whole volume fraction range at 303 K, 313 K, and 323 K temperatures

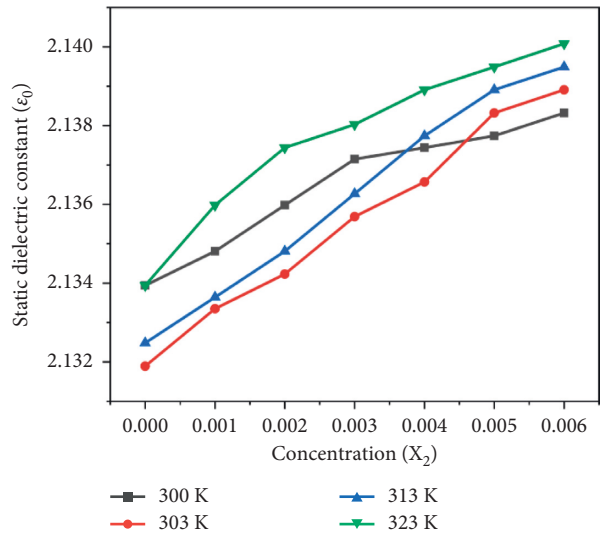

Figure 1: Variations in static dielectric constant values as a function of BaO: Therm500 nanofluids.

Table 1: The variation of the molar polarization (P_{12}) and dipole moment (μ) values of BaO: Therm500 nanofluids with different combinations.

Concentration, X_2 (g)	P_{12}	μ (D)	P_{12}	μ (D)	P_{12}	μ (D)	P_{12}	μ (D)
	300 K		303 K		313 K		323 K	
0.000	27.3813	9.12	28.5621	8.15	29.7451	11.63	31.2314	12.98
0.001	25.7882	9.52	27.4526	8.56	29.6542	11.02	31.6587	12.15
0.002	24.8722	9.26	26.7854	8.99	28.1254	9.67	30.8956	10.01
0.003	35.8715	10.01	37.2614	10.82	39.2659	13.95	41.6985	15.65
0.004	30.115	9.54	32.1452	9.12	34.8952	9.89	36.2561	12.45
0.005	29.7935	9.57	31.6852	9.01	33.6985	9.26	35.2614	10.57
0.006	21.895	10.59	23.2658	10.57	30.6521	9.29	34.2365	10.99

suggests that the dipole pairs in the nanofluids have formed an antiparallel orientation.

The dipole moments of the Bao: Therm500 nanofluids with varying BaO combinations at four distinct temperatures are shown in Table 1. The μ grows as the temperature rises from 300 K to 323 K. Also, when the temperature increases, molar volume increases. Then when the temperature rises, the thermal disturbance rises. As the dipole elevation increases, the effective length increases correspondingly. A positive dipole moment shows that polarization interaction is to blame for the higher proclivity of complex development in particle-fluid systems [45, 46].

3.3. Molar Polarization (P_{12}). The P_{12} of BaO: Therm500 with different volumes and temperatures are shown in Table 1. The drop in molar polarization values of BaO: Therm500 nanofluids with increasing BaO: Therm500 combinations is due to the weak contact between the BaO and Therm500 molecules. Similarly, the increase in molar polarization values of BaO: Therm500 nanofluids with increasing BaO: Therm500 combinations is owing to the vital contact between the BaO and Therm500 molecules. The molar polarization values of pure BaO: Therm500 nanofluids fluctuate at all volumes, except at 0.003 grams, which reaches a high value at all four temperatures. The increased P_{12} value at 0.003 g of BaO: Therm500 is attributed to strong interactions in the BaO: Therm500 system. Polarization variations may be affected by the volumes of the nanofluid system. Because of variations in electron negativity, the electron density is focused on one side of a molecule. As a result, the molecule is polarized, with both partial equal charges [47, 48]. Using dielectric constant values BaO: Therm500, the polarizability may be computed directly. In reality, the interactions between them are determined by the polarizability of the chemical and its combination [49].

3.4. Excess Dielectric Constant (ε^E). The ε^E values of BaO: Therm500 nanofluids are shown in Figure 2. The ε^E data provides the following information $\varepsilon^E = 0$ and demonstrates that none of the interaction takes place in nanofluid, as a result of which the mixing behaviour is best. $\varepsilon^E < 0$ indicates that interaction takes place in nanofluids due to a total number of significant dipoles leading to the nanofluid's dielectric polarization hat is lowered. $\varepsilon^E > 0$ permits interaction to take place in a system that increases the amount of efficient dipoles involved in nanoparticle fluid dielectric polarization. A measure of the intensity of the H-bond contacts between unlike molecules is the magnitude of the ε^E values; greater ε^E values, and vice versa, signify stronger H-bond, unlike molecular connectivities. The molar

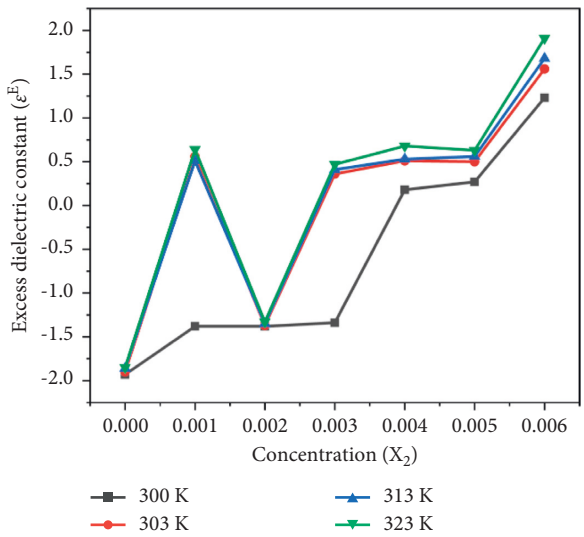

Figure 2: The variation of the excess dielectric constant values of BaO: Therm500 nanofluids.

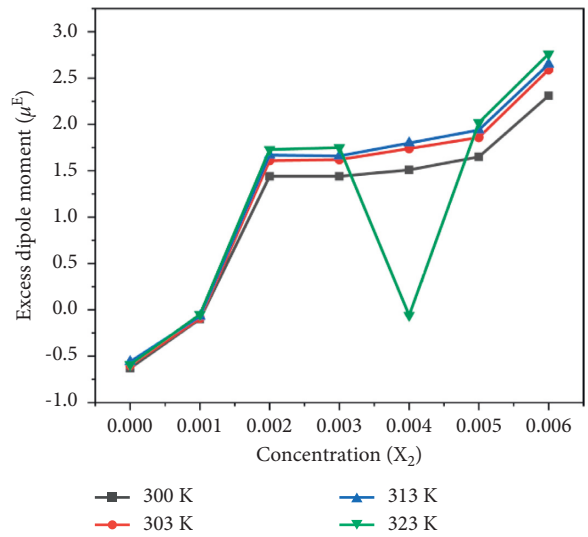

Figure 3: The variation of the excess dipole moment values of BaO: Therm500 nanofluids.

concentration that relates to the higher values of ε^E denotes the stable combination [50].

Figure 2 depicts ε^E versus BaO combination at four distinct temperatures (300 K–323 K). ε^E provides significant information regarding interaction of fluids. ε^E of BaO: Therm500 nanofluids was calculated using equation (3). The excess dielectric constant values for BaO: Therm500 systems are found to be both positive-negative for all combinations. The ε^E's negative value indicates that one of the combination components acts as a structure-breaker. For self-association structures based on H-bonding, some dipoles are aligned anti-parallel. These lower ε^E of the nanofluids below their ideal mixing values by reducing the total amount of parallel aligned dipoles in the mixture [51]. Negative values of (ε^E) are visible in Figure 2 because the less polar configuration is created, resulting in a decreased macro permittivity. The (ε^E) is positive for a few volumes at 300 K, indicating that ideal interaction. During this temperature range, the net dipole moment rises. It has been obtained from Figure 2 that the other three temperatures had similar variations of ε^E. It is possible that the overall number of dipoles in the fluid is higher than in pure fluids. The formation of new structures results in a greater macroscopic permittivity [52].

3.5. Excess Dipole Moment (μ^E). The fluctuations in the μ^E values of pure BaO: Therm500 nanofluids as a function of volume and temperature are depicted in Figure 3. It is also discovered that μ^E values of BaO: Therm500 nanofluids vary barely slightly across all combinations, exception of 0.004 g at all 323 K. At a combination of 0.004 g of BaO, the μ^E for the pure BaO: Therm500 nanofluids system is negative, showing that the ionic structure of the pure BaO: Therm500 nanofluids makes no contribution to the overall dipole moment. In order to form an ionic structure, an excess dipole moment is required, which is related to protonation [53]. In BaO: Therm500 nanofluids, there is a departure from the linear relationship, indicating molecular interactions in BaO nanoparticles.

4. Conclusion

At different temperatures (300 K–323 K), the dielectric characteristics of the synthesized BaO: Therm500 nanofluids are calculated (0.001 g–0.006 g). The value of the BaO: Therm500 nanofluid dielectric constant rises with temperature. The Kirkwood factor provides evidence for the dipoles' parallel and antiparallel alignment in the mixture of the fluids. At different fluid and nanoparticle combinations at four different temperatures, it seems that the alignment of the dipoles along the field is changing from parallel to antiparallel. The excess permittivity is positive at lower temperatures, meaning there are more dipoles overall in the fluids than there would be if they were pure fluids, which would be the case if the excess permittivity were negative. The excess permittivity turns negative at higher temperatures, suggesting that specific interactions between different molecules are occurring. The ionic structure of the pure BaO: Therm500 nanofluids system does not contribute to the overall dipole moment, as shown by the negative μ^E for the pure BaO: Therm500 nanofluids system at a combination of 0.004 g of BaO. Negative values of excess dipole moment demonstrate the absence of any contribution to the overall dipole moment from the ionic structure of the BaO: Therm500 nanofluids (μ^E). BaO: Therm500 nanofluids' dielectric characteristics value display positive-negative fluctuations across the combination range at all temperatures, suggesting the presence of intermolecular interactions in nanofluids. BaO: Therm500 nanofluids' molar polarization values change at all volumes, with the exception of 0.003 grams, which experiences a high value at all four temperatures. Strong interactions in the BaO: Therm500 system were said to be the cause of the elevated (P_{12}) value at 0.003 g of BaO. The Bruggman factor exhibits a deviation from the

linear relationship in nanofluids, indicating molecular interactions. Ultrasonic and dielectric investigations are used to support the molecular interactions discovered in BaO: Therm500 nanofluids. This paper provides precise dielectric constant values for nanofluids, which are widely used in physical, biological, chemical, industrial, pharmaceutical, technical, and scientific applications.

Data Availability

The data used to support the findings of this study are included within the article.

Disclosure

This work was performed as a part of the employment of institutions.

Conflicts of Interest

The authors declare that there are no conflicts of interest in the article.

Acknowledgments

The authors gratefully credit the Karunya Institute of Science and Technology in Coimbatore, Tamil Nadu, for providing characterization facilities.

References

[1] I. Kuznetcov, A. Kantzas, and S. Bryant, "Dielectric spectroscopy of nanofluids in deionized water: method of removing electrode polarization effect," *Colloids and Surfaces A: Physicochemical and Engineering Aspects*, vol. 647, Article ID 129039, 2022.

[2] S. P. Kamble, Y. S. Sudake, S. S. Patil, P. W. Khirade, and S. C. Mehrotra, "Dielectric and optical properties of polar and nonpolar liquids at different temperatures," *International Journal of Pharma Bio Sciences*, vol. 2, pp. 297–309, 2011.

[3] B. S. Narwade, P. G. Gawali, R. Pande, and G. M. Kalamse, "Dielectric studies of binary mixtures of n-propyl alcohol and ethylenediamine," *Journal of Chemical Sciences*, vol. 117, no. 6, pp. 673–676, 2005.

[4] U. B. Tumberphalea, R. S. Kawaleb, N. P. Pawara, and G. M. Kalamsea, "Ultrasonic behaviour of binary mixture of N-propyl alcohol in ethylene diamine at 3 MHz frequency international symposium on ultrasonics," *International Journal of Science and Research*, vol. 22, no. 24, 2015.

[5] M. Kumar, R. Tamilarasan, and V. Sivakumar, "Adsorption of Victoria blue by carbon/Ba/alginate beads: kinetics, thermodynamics and isotherm studies," *Carbohydrate Polymers*, vol. 98, no. 1, pp. 505–513, 2013.

[6] A. P. Maharolkar, Y. Sudke, S. Kamble et al., "Densities, viscosities and refractive indices of n-butanol+ allyl chloride mixture at 298 K," *International Journal of Chemistry*, vol. 2, no. 2, p. 250, 2010.

[7] G. C. Pedrosa, J. A. Salas, and M. Katz, "Excess molar volumes and excess viscosities of the n-pentanol-cumene-1, 4-dioxane system at 298.15 K," *Thermochimica Acta*, vol. 160, no. 2, pp. 243–252, 1990.

[8] J. Nath and S. K. Chaudhary, "Excess volumes, dielectric constants, refractive indexes, and viscosities for anisole+ methylene chloride, 1, 2-dichloroethane, trichloroethene, tetrachloroethene, and cyclohexane," *Journal of Chemical & Engineering Data*, vol. 37, no. 4, pp. 387–390, 1992.

[9] F. Rived, M. Roses, and E. Bosch, "Densities, refractive indices, absolute viscosities, and static dielectric constants of 2-methylpropan-2-ol+ hexane, +benzene, +propan-2-ol, +methanol, +ethanol, and +water at 303.2 K," *Journal of Chemical & Engineering Data*, vol. 40, no. 5, pp. 1111–1114, 1995.

[10] F. Casarini, L. Marcheselli, A. Marchetti, L. Tassi, and G. Tosi, "The relative permittivity of 1, 2-ethanediol+ 2-methoxyethanol+ water ternary mixtures," *Journal of Solution Chemistry*, vol. 22, no. 10, pp. 895–905, 1993.

[11] A. K. Tiwari, A. Kumar, and Z. Said, "Synthesis, characterization, and measurement techniques for the thermophysical properties of nanofluids," in *Advances in Nanofluid Heat Transfer*, pp. 59–93, Elsevier, Amsterdam, Netherlands, 2022.

[12] A. Subramaniyan, L. P. Sukumaran, and R. Ilangovan, "Investigation of the dielectric properties of TiO_2 nanofluids," *Journal of Taibah University for Science*, vol. 10, no. 3, pp. 403–406, 2016.

[13] R. A. Taylor, P. E. Phelan, T. P. Otanicar, R. Adrian, and R. Prasher, "Nanofluid optical property characterization: towards efficient direct absorption solar collectors," *Nanoscale Research Letters*, vol. 6, no. 1, pp. 225–311, 2011.

[14] B. G. Nemmaniwar, N. V. Kalyankar, and P. L. Kadam, "Dielectric behaviour of binary mixture of 2-chloroaniline with 2-methoxyethanol and 2-ethoxyethanol," *Orbital-The Electronic Journal of Chemistry*, vol. 5, no. 1, pp. 1–6, 2013.

[15] P. S. Nikam, M. C. Jadhav, and M. Hasan, "Density and viscosity of mixtures of nitrobenzene with methanol, ethanol, propan-1-ol, propan-2-ol, butan-1-ol, 2-methylpropan-1-ol, and 2-methylpropan-2-ol at 298.15 and 303.15 K," *Journal of Chemical & Engineering Data*, vol. 40, no. 4, pp. 931–934, 1995.

[16] H. Yilmaz, "Excess properties of alcohol-water systems at 298.15 K," *Turkish Journal of Physics*, vol. 26, no. 3, pp. 243–246, 2002.

[17] W. Wen, S. Men, and K. Lu, "Structure-induced nonlinear dielectric properties in electrorheological fluids," *Physical Review E*, vol. 55, no. 3, pp. 3015–3020, 1997.

[18] V. V. Shcherbakov, Y. M. Artemkina, I. A. Akimova, and I. M. Artemkina, "Dielectric characteristics, electrical conductivity and solvation of ions in electrolyte solutions," *Materials*, vol. 14, no. 19, p. 5617, 2021.

[19] K. Savjani, "Design and optimization of itraconazole tablet employing solid dispersion approach," *Asian Journal of Pharmaceutics*, vol. 11, no. 1, 2017.

[20] C. V. V. Ramana, A. B. V. K. Kumar, M. A. Kumar, and M. K. Moodley, "Dielectric and excess dielectric constants of acetonitrile+ butyl amine, + ethylamine, and+ methylamine at 303, 313, and 323 K," *Journal of Chemistry*, vol. 2013, Article ID 687106, 6 pages, 2013.

[21] S. S. Dubal, S. B. Sayyad, S. S. Patil, and P. W. Khirade, "Microwave dielectric characterization of binary mixture of diethylene glycol monomethyl ether with N, N-dimethylformamide," *International Multidisciplinary Research Journal*, vol. 1, no. 4, 2011.

[22] I. Capek, "Hard template-directed synthesis," in *Noble Metal Nanoparticles*, pp. 415–536, Springer, Berlin, Germany, 2017.

[23] A. Alexiadis and S. Kassinos, "Molecular simulation of water in carbon nanotubes," *Chemical Reviews*, vol. 108, no. 12, pp. 5014–5034, 2008.

[24] 2022 https://www.dow.com/en-us/product-technology/pt-lubricants.html.
[25] M. Saeidi, H. Sarpoolaky, and S. M. Mirkazemi, "Ultrasonic–assisted co–precipitation method of preparation of nanocomposites in the Al_2O_3–TiO_2–ZrO_2 system: characterization and microstructure," *Journal of Ultrafine Grained and Nanostructured Materials*, vol. 45, no. 1, pp. 7–12, 2012.
[26] E. Sundharam, A. K. S. Jeevaraj, and C. Chinnusamy, "Effect of ultrasonication on the synthesis of barium oxide nanoparticles," *Journal of Bionanoscience*, vol. 11, no. 4, pp. 310–314, 2017.
[27] M. A. AbolghassemiFakhree, D. R. Delgado, F. Martínez, and A. Jouyban, "The importance of dielectric constant for drug solubility prediction in binary solvent mixtures: electrolytes and zwitterions in water + ethanol," *American Association of Pharmaceutical Scientists*, vol. 11, no. 4, pp. 1726–1729, 2010.
[28] R. Choudhary, D. Khurana, A. Kumar, and S. Subudhi, "Stability analysis of Al_2O_3/water nanofluids," *Journal of Experimental Nanoscience*, vol. 12, no. 1, pp. 140–151, 2017.
[29] S. Umar, F. Sulaiman, N. Abdullah, and S. N. Mohamad, "Investigation of the effect of pH adjustment on the stability of nanofluid," *AIP Conference Proceedings*, vol. 2031, no. 1, Article ID 020031, 2018.
[30] 2022 https://www.venlub.in/heat-transfer-fluid.html.
[31] S. S. Sastrya, K. Parvateesama, T. Vishwamb, and V. R. K. Murthyc, "Investigation of intermolecular interaction between isobutanol and methyl benzoate using excess dielectric and thermodynamic parameters," *International Journal of Engineering Research*, vol. 3, no. 3, 2014.
[32] M. Valiskó and D. Boda, "Dielectric constant of the polarizable dipolar hard sphere fluid studied by Monte Carlo simulation and theories," *Condensed Matter Physics*, vol. 8, no. 2, p. 357, 2005.
[33] B. Maribo-Mogensen, G. M. Kontogeorgis, and K. Thomsen, "Modeling of dielectric properties of complex fluids with an equation of state," *The Journal of Physical Chemistry B*, vol. 117, no. 12, pp. 3389–3397, 2013.
[34] A. C. Kumbharkhane, S. M. Puranik, and S. C. Mehrotra, "Dielectric relaxation of tert-butyl alcohol–water mixtures using a time-domain technique," *Journal of the Chemical Society, Faraday Transactions*, vol. 87, no. 10, pp. 1569–1573, 1991.
[35] V. A. Rana, A. D. Vyas, and S. C. Mehrotra, "Dielectric relaxation study of mixtures of 1-propanol with aniline, 2-chloroaniline and 3-chloroaniline at different temperatures using time domain reflectometry," *Journal of Molecular Liquids*, vol. 102, no. 1–3, pp. 379–391, 2003.
[36] A. C. Kumbharkhane, S. M. Puranik, and S. C. Mehrotra, "Dielectric relaxation studies of aqueous N, N-dimethylformamide using a picosecond time domain technique," *Journal of Solution Chemistry*, vol. 22, no. 3, pp. 219–229, 1993.
[37] D. A. G. Bruggman, "Berechnung verschiedener physikalischer konstanten von heterogenen substanzen," *Annalen der Physik*, vol. 24, pp. 636–664, 1935.
[38] U. Kaatze and K. Giese, "Dielectric spectroscopy on some aqueous solutions of 3 : 2 valent electrolytes. A combined frequency and time domain study," *Journal of Molecular Liquids*, vol. 36, pp. 15–35, 1987.
[39] S. M. Puranik, A. C. Kumbharkhane, and S. C. Mehrotra, "The static permittivity of binary mixtures using an improved Bruggeman model," *Journal of Molecular Liquids*, vol. 59, no. 2-3, pp. 173–177, 1994.
[40] R. J. Sengwa, S. Sankhla, S. Sankhla, and S. Sharma, "Characterization of heterogeneous interaction behavior in ternary mixtures by a dielectric analysis: equi-molar H–bonded binary polar mixtures in aqueous solutions," *Journal of Solution Chemistry*, vol. 35, no. 8, pp. 1037–1055, 2006.
[41] N. E. Hill, W. E. Vaughan, A. H. Price, and M. Davies, *Dielectric Properties and Molecular Behaviour*, Van Nostrand Reinhold, London, UK, 1969.
[42] S. S. Kumar, E. J. Rubio, M. Noor-A-Alam et al., "Structure, morphology, and optical properties of amorphous and nanocrystalline gallium oxide thin films," *Journal of Physical Chemistry C*, vol. 117, no. 8, pp. 4194–4200, 2013.
[43] V. V. Navarkhele and M. K. Bhanarkar, "Temperature-dependent dielectric relaxation study of binary mixture using the time domain reflectometry method," *Physics and Chemistry of Liquids*, vol. 50, no. 3, pp. 378–388, 2012.
[44] P. S. Patil, "Versatility of chemical spray pyrolysis technique," *Materials Chemistry and Physics*, vol. 59, no. 3, pp. 185–198, 1999.
[45] Z. R. Herm, J. A. Swisher, B. Smit, R. Krishna, and J. R. Long, "Metal–organic frameworks as adsorbents for hydrogen purification and precombustion carbon dioxide capture," *Journal of the American Chemical Society*, vol. 133, no. 15, pp. 5664–5667, 2011.
[46] M. Jorge, J. R. Gomes, and M. C. Barrera, "The dipole moment of alcohols in the liquid phase and in solution," *Journal of Molecular Liquids*, vol. 356, Article ID 119033, 2022.
[47] P. L. Silvestrelli and M. Parrinello, "Structural, electronic, and bonding properties of liquid water from first principles," *Journal of Chemical Physics*, vol. 111, no. 8, pp. 3572–3580, 1999.
[48] V. V. Navarkhele, S. S. Patil, and P. W. Khirade, "Measurement of static dielectric constants of aqueous solution of methanol for various temperatures," *Journal of Chemical and Pharmaceutical Research*, vol. 6, no. 12, pp. 832–838, 2014.
[49] G. A. Samara, "The relaxational properties of compositionally disordered ABO3 perovskites," *Journal of Physics: Condensed Matter*, vol. 15, no. 9, pp. R367–R411, 2003.
[50] C. V. Ramana, A. K. Kumar, A. S. Kumar, M. A. Kumar, and M. K. Moodley, "Dielectric and excess dielectric constants in non polar+ polar binary liquid mixtures of toluene with alcohols at 303, 313, and 323 K," *Thermochimica Acta*, vol. 566, pp. 130–136, 2013.
[51] N. A. Kamel, S. L. Abd-El-Messieh, S. H. Mansour, B. A. Iskander, W. A. Khalil, and K. N. Abd-El-Nour, "Biophysical properties of crosslinked poly (propylene fumarate)/hydroxyapatite nanocomposites," *Romanian Journal of Biophysics*, vol. 22, no. 3-4, pp. 189–214, 2012.
[52] V. A. Durov, "Modeling of supramolecular ordering in molecular liquids: structure, physicochemical properties and macroscopic manifestations," *Journal of Molecular Liquids*, vol. 78, no. 1-2, pp. 51–82, 1998.
[53] N. Šegatin, T. PajkŽontar, and N. PoklarUlrih, "Dielectric properties and dipole moment of edible oils subjected to "frying" thermal treatment," *Foods*, vol. 9, no. 7, p. 900, 2020.

Hindawi
Journal of Engineering
Volume 2022, Article ID 8216221, 4 pages
https://doi.org/10.1155/2022/8216221

Research Article

Algorithm for Recognition of Movement of Objects in a Video Surveillance System Using a Neural Network

S. Harish,[1] C. Anil Kumar,[1] Lakshmi Shrinivasan,[2] S. Rohith,[3] and Belete Tessema Asfaw[4]

[1]*Department of Electronics and Communication Engineering, R. L. Jalappa Institute of Technology, Kodigehalli, Doddaballapur, Karnataka 561203, India*
[2]*Department of Electronics and Communication Engineering, Ramaiah Institute of Technology, Bengaluru, Karnataka 560054, India*
[3]*Department of Electronics and Communication Engineering, Nagarjuna College of Engineering and Technology, Bengaluru, Karnataka 562164, India*
[4]*Department of Chemical Engineering, Haramaya Institute of Technology, Haramaya University, Haramaya, Ethiopia*

Correspondence should be addressed to Belete Tessema Asfaw; belete.tessema@haramaya.edu.et

Received 28 June 2022; Revised 22 July 2022; Accepted 26 July 2022; Published 12 August 2022

Academic Editor: Karthikeyan Sathasivam

The aim of this article is to address the problem of protecting the private property of a protected object, namely: we propose an algorithm for detection of object movements by means of a neural network for the video surveillance system. Consistency of perception of the external world in the form of images allows for the investigation of properties of the limited number of objects on the basis of familiarization with their final number. Based on the literature analysis, the main definitions of the theory of image recognition were established, such as "image," "sign," and "vector realization." A comparison is made of approaches, methods, and technologies for recognizing the movement of objects, and their strengths and weaknesses are discussed. It was found that the neuron network is the most effective method for solving the problem of recognition of the movement of objects due to the accuracy of the result, simplicity, and speed. On the basis of the structural scheme of the complex algorithm of processing and analysis of images, the algorithm for recognition of the motion of objects by means of a neural network for the system of video observation is developed.

1. Introduction

In today's world, the slogan is becoming more and more relevant. This applies to all spheres of activity and human life. Security of the object being protected is one of its components, and video surveillance is one of the ways to maintain security at the appropriate level [1]. The surveillance system is a set of hardware and software designed to monitor the territory, activities, and situation. Traditional video surveillance systems are widespread in today's security agencies and show a high level of protection but have their own shortcomings: as a result, the large amount of recorded video material requires a high amount of memory and time to analyze and view. Our research is focused on improving the efficiency of video surveillance systems [2]. The video surveillance information system is based on modern cybernetic methods and technologies, namely, machine learning [1], computer vision theory [2], and the theory of image recognition [3].

The work of F. Rosenblatt must be noted among foreign scientists; he proposed in 1957 a perfect machine for the recognition of images. It was the simplest model of human brain activity. A significant contribution to the further development of the theory of image recognition was made by W. Gardner. The identification of object movements is an extremely complex task, but all of them rely on neural measurements, which allows for more accurate results in a short period of time. This is confirmed by the practical experience of the authors. The aim of this research is to develop and create an algorithm for recognition of objects' movements by means of a neural network for video surveillance systems [3]. Artificial neural networks are

composed of nodes or units that resemble the neurons in a biological brain. A signal can be transmitted from one artificial neuron to another through each connection, just as it would be in a biological brain.

1.1. Theoretical Foundations of Research. Pattern recognition theory is a branch of cybernetics devoted to creating theoretical foundations for the classification and identification of objects. The processes of classification and identification are called recognition, and objects are called things. Based on the research of the authors, we shall identify the main definitions and give a short description of each method of the theory of image recognition. A pattern is a model that reproduces the properties of the object being recognized. An image is characterized by a multiplicity of recognition features, which create a structured vector-image realization. Often the image is replaced with a recognition class. The feature of recognition is a characteristic of a certain property of the object being analyzed. Vector realization of an image is a structured, i.e., ordered, sequence of recognition features, which will be presented in the form of a vector row or vector carrier. System image recognition—a complex electronic and computational method—is capable of modelling mental processes in humans during decision making with the aim of detecting analogies among the surveyed objects [4]. For image recognition, it is necessary to solve two main tasks: to divide the space of recognition signs into areas corresponding to a certain class of objects and to identify the relevance of the image being recognized to the corresponding class. The main approaches in image recognition theory are as follows: (1) algebraic, the main advantage of which is simple decisive rules; the main disadvantage of this approach is the unreliability of recognition, as it does not take into account uncontrolled factors that affect the recognition process; (2) geometric, which is characterized by its universality, simplicity, and ease of interpretation of the recognition algorithms; (3) statistical, which uses statistical characteristics of data analysis; (4) biological, which includes neural networks; (5) measurement; (6) the non-fuzzy one, which is created on the basis of algebraic approach, allows modelling the processes of recognition of images, which are naturally overlapping in the space of recognition signs, but it is not applied to optimization of parameters of the recognition system functioning; and (7) a game-theoretic approach, in which the decision-making rules are characterized by a high degree of complexity and a low degree of certainty of recognition. In practice, these approaches complement one another to improve the efficiency of image recognition. Image recognition methods can be roughly divided into two groups: intrinsic and extrinsic [5]. The study demonstrates the features of each group and the methods that belong to each group and identifies the quality characteristics of these methods and their disadvantages. There are several main tasks involved in image recognition, including the following: input data; a selection of informative features; object recognition and classification; automatic classification; dynamic recognition; dynamic classification; forecasting.

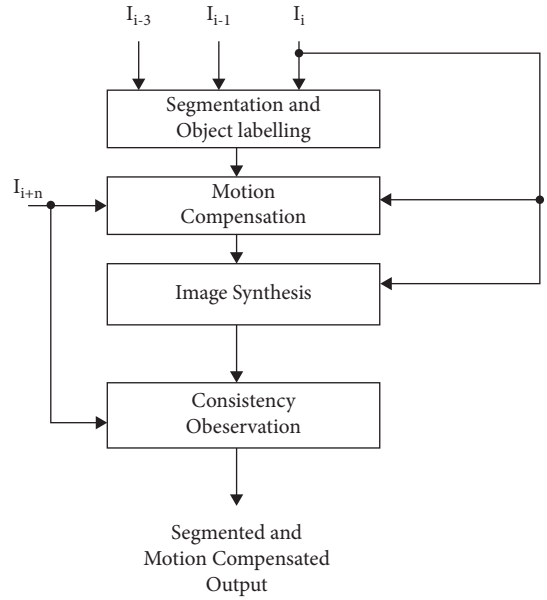

Figure 1: An algorithm for processing and analyzing images.

1.2. Research Results. As evidenced by the scientific sources on the problem of image recognition, the interest in solving more complex tasks of recognition of objects, due to automation, and the need for image communication processes in intelligent systems are growing every year. Therefore, improving the implementation of recognition of computer systems images is relevant. One of the promising directions of solving this problem is based on using piecewise neural networks and neurocomputers as the most progressive method in relation to the problems of image recognition classification [6]. At our time, a large number of neural network archetypes have been proposed for use in the recognition of objects. The analysis of the proposed solutions shows that none of the best-performing neuroscience solutions would be the best. The development of the theory of piecewise neural networks is associated with the names of neural networks which are useful for solving tasks in cases where a large amount of data has been accumulated, but there is no software to process and systematize it; the data available are spoiled, incomplete, or not systematized; and data are so different that it is difficult to see the links and patterns between them [1]. The artificial neural network (ANN) is a system of interconnected and mutually interconnected neurons based on relatively simple processors. Each ANN processor periodically receives signals from one processor and periodically sends signals to the other processors. Together, these simple processors integrated into the measure are able to solve complex tasks [7]. Neurons are most often located in the network by rank. Neurons of the first level are usually input. They receive data from outside and after their processing transfer impulses through synapses of neurons to the next level. Neurons on the other level (called adjacent, as it is indirectly connected to neither the input nor the output of the ANN) process the received impulses and transmit them to the neurons on the output level. As the neurons are mutated, each input-level processor

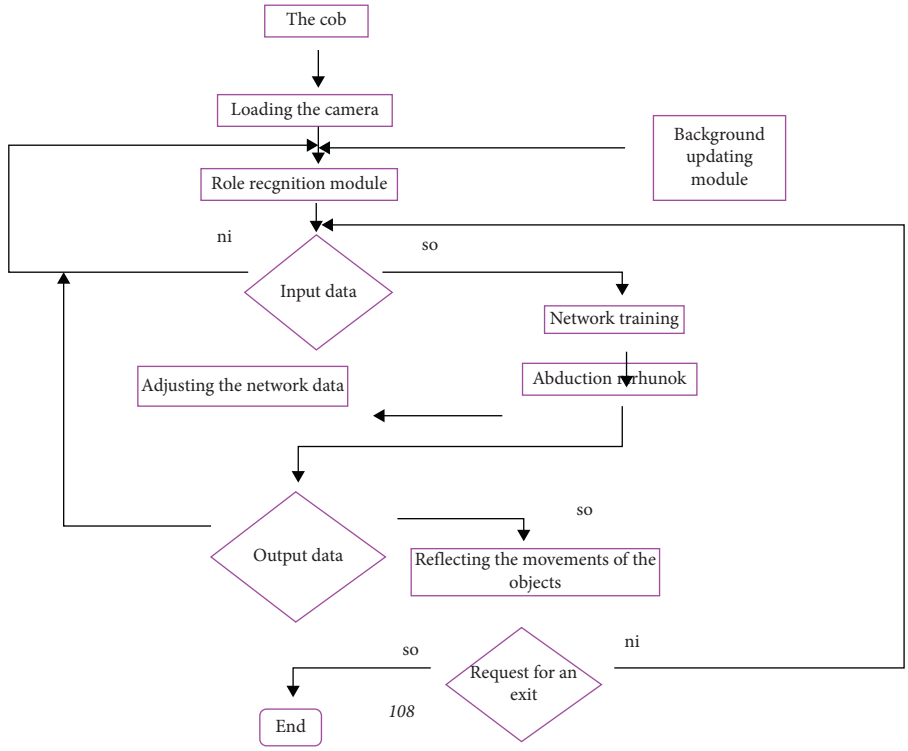

Figure 2: Image recognition algorithm.

is linked to several output-level processors, each of which in turn is linked to several output-level processors. This architecture is the simplest ANN, which is trainable and can find simple interconnections in the data. Figure 1 shows a schematic diagram of the complex image processing and analysis algorithm. This algorithm includes modules for controlling the calculation process. Thus, depending on the type of tasks solved, the structure of the complex algorithm can vary. When each stage of image processing and analysis is completed, the obtained information is fed to the control unit, which forms the plan for further procedures. Apart from the control unit, the database is stored in the processing system's memory, which contains the required data and various information processing procedures in accordance with accepted regulations [8].

1.3. Image Recognition Algorithm. Information support of the project of the automated system of video surveillance by means of a mathematical model of recognition of object movements can be represented in the form of a structural algorithm of information flows, which is presented in Figure 2. As a result, the network is self-organized, i.e., after the method is defined, modules based on different criteria matrixes are reconfigured in a cycle, making the scheme dynamic rather than static.

1.4. Findings and Prospects for Further Research. The development of video surveillance systems offers new possibilities not only for the detection of offenses but also, and more importantly, for their prevention. The capabilities of modern systems are also used for intelligent analysis of the video stream received. At present, there are a lot of different algorithms for image recognition. Each of them was created for a particular type of image, and for its subsequent use in the application of programming, we need to choose the most optimal method in terms of the specific task and improve it in specific realities. Our next task is to develop a software maintenance algorithm for video surveillance with the help of the runway recognition system.

Data Availability

The data used to support the findings of this study are included within the article.

Conflicts of Interest

The authors declare that they have no conflicts of interest.

References

[1] G. V. Mygal and O. F. Protasenko, "Inzheneriya lyudskogo chinnika v suchasniy osviti Human factor engineering in modern education," *Scientific notes of Taurida National V.I. Vernadsky University. Series: Technical Sciences*, vol. 6, no. 1, pp. 1–6, 2019.

[2] J. Dul, R. Bruder, P. Buckle et al., "A strategy for human factors/ergonomics: developing the discipline and profession," *Ergonomics*, vol. 55, no. 4, pp. 377–395, 2012.

[3] J. R. Saward and N. A. Stanton, "Individual latent error detection: simply stop, look and listen," *Safety Science*, vol. 101, pp. 305–312, 2018.

[4] J. R. Wilson, "Fundamentals of systems ergonomics/human factors," *Applied Ergonomics*, vol. 45, no. 1, pp. 5–13, 2014.

[5] R. H. Stevens, T. L. Galloway, and A. Willemsen-Dunlap, "Neuroergonomics: quantitative modeling of individual, shared, and team neurodynamic information," *Human Factors: The Journal of the Human Factors and Ergonomics Society*, vol. 60, no. 7, pp. 1022–1034, 2018.

[6] H. Hsiao, J. Chang, and P. Simeonov, "Preventing emergency vehicle crashes: status and challenges of human factors issues," *Human Factors: The Journal of the Human Factors and Ergonomics Society*, vol. 60, no. 7, pp. 1048–1072, 2018.

[7] A. C. Marinescu, S. Sharples, A. C. Ritchie, T. Sánchez López, M. McDowell, and H. P. Morvan, "Physiological parameter response to variation of mental workload," *Human Factors: The Journal of the Human Factors and Ergonomics Society*, vol. 60, no. 1, pp. 31–56, 2018.

[8] E. Kapkın and S. Joines, "An investigation into the relationship between product form and perceived meanings," *International Journal of Industrial Ergonomics*, vol. 67, pp. 259–273, 2018.

Hindawi
Journal of Engineering
Volume 2022, Article ID 9735862, 6 pages
https://doi.org/10.1155/2022/9735862

Research Article

Smart Manufacturing through Machine Learning: A Review, Perspective, and Future Directions to the Machining Industry

A. S. Rajesh,[1] **M. S. Prabhuswamy**,[2] **and Srinivasan Krishnasamy**[3]

[1]*Department of Mechanical Engineering, JSS Science and Technology University, Mysuru, Karnataka 570006, India*
[2]*Department of Mechanical Engineering, JSS Science and Technology University, Mysuru, Karnataka 570006, India*
[3]*Arba Minch University, Arba Minch, Ethiopia*

Correspondence should be addressed to A. S. Rajesh; as.rajesh.jce@gmail.com and Srinivasan Krishnasamy; srinivasan.krishnasamy@amu.edu.et

Received 24 June 2022; Accepted 13 July 2022; Published 11 August 2022

Academic Editor: Karthikeyan Sathasivam

Nowadays, to reach progressive growth although being competitive in the market, the manufacturing industries are using advanced technologies such as cloud computing, the Internet of things (IoT), artificial intelligence, 3D printer, nanotechnology, cryogenics, robotics, and automation in smart manufacturing sectors. One such subclass of artificial intelligence is machine learning, which uses a computer system for making predictions and performing definite tasks without any use of specific instructions to enhance the quality of the product, and rate of production, and to optimize the processes and parameters in machining operations. A broad category of manufacturing that is technology-driven utilizes internet-connected machines to monitor the performances of manufacturing processes referring as smart manufacturing. The current paper presents a comprehensive survey and summary of different machine learning algorithms which are being employed in various traditional and nontraditional machining processes, and also, an outlook of the manufacturing paradigm is presented. Subsequently, future directions in the machining industry were proposed based on trends and challenges that are accompanying machine learning.

1. Introduction

The manufacturing industry takes on many paradigm changes over the past due to industrial revolution that took place in the eighteenth century with the invention of steam engine to the development of information and communication technology. Moving on, automation and robotization in the late twentieth century followed by industry 4.0, the worldwide manufacturing sectors are currently dealing with smart manufacturing areas to get ready for improving their profitability through the elimination of nonvalued operations to attain a higher profit. Significant innovations such as deep learning, data analytics, cloud computing, IoT, 3D printing, robotics, and artificial intelligence have been applied to different fields of manufacturing to achieve higher productivity [1]. The technological development that takes place in the field of advanced smart systems has reached a high level which leads to the way to use of modern tools like machine learning algorithms to a greater extent in the field of manufacturing. Figure 1 represents the different phases present in artificial intelligence for solving problems.

Collecting necessary data and information to preprocess for the subsequent analysis is necessary for choosing an appropriate machine learning algorithm to solve properly defined problems. According to the gathered data, the right kind of model must be established, and it should be trained properly with the required amount of data to achieve the best results. Furthermore, obtained results should be analyzed and validated for fetching the best-improved results.

Smart manufacturing takes conventional manufacturing to a leading edge. To attain the objectives, machining parameters respond smartly to the changes according to the process. By the effective collaboration of all the resources together to make strategic innovation in the existing manufacturing industry to achieve a predefined set of objectives in real time [2]. It has an effective data-driven system coupled with 5 Ms' (man, machine, material, method, and

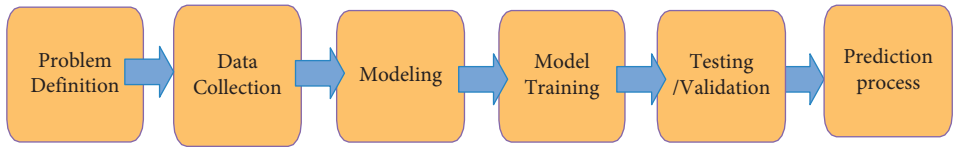

Figure 1: Steps involved in problem-solving using artificial intelligence.

money) and all other resources to achieve desired benefits which are displayed in Figure 2.

Here, this paper focused on different machine learning algorithms used in various smart machining processes were reviewed and summarized, and a perspective on the machining industry was suggested. Furthermore, future trends and challenges with smart machining using machine learning were indicated as future research directions.

The manufacturing industry has made huge advancements over the years, from the early machining process to today's automated manufacturing process [3]. Manufacturing and industrialization systems have reached their fourth generation of industrial revolution after undergoing various inventions and repeated trials over the years. Several improvements and changes have taken place during this time period [4].

In the current industrial age, smart manufacturing systems play an important role in implementing better manufacturing technology. Global economic growth is strengthened by smart manufacturing technologies that increase operational efficiency and productivity. IoT and IIoT have played a significant role in enhancing the manufacturing system equipped with smart manufacturing systems with the emergence of IoT and IIoT. Many industries are developing their manufacturing systems using smart technologies, according to various researches in manufacturing systems. Compatible existing machines and systems with the new technology are one of the challenges for a smart manufacturing system [5].

2. Machine Learning Algorithms Used for Smart Machining

2.1. Processes. An ample amount of work has been done by several researchers to describe the significance of machining learning algorithms in different categories of smart machining operations. Machining processes are categorized as traditional and nontraditional machining, and a summary of algorithms is used for its dealt with herein [6].

2.2. Traditional Machining. Traditional machining is based on the removal of materials by the use of harder tools by using mostly mechanical energy. This section emphasizes different cases of traditional machining processes which use machine learning algorithms to optimize the process thereby increasing productivity. Turning, milling, grinding, and drilling operations are discussed and summarized in Table 1.

2.3. Turning Operation. Here, 5 recent papers based on turning operations that employed different types of machine learning algorithms are reviewed for many reasons viz, parameter optimization, tool monitoring, and Ra predictions. It reviewed in detail the use of the multiobjective genetic algorithm (MOGA) for analysis of tool selection and tool path length by optimizing the cutting forces that are induced in the turning process [7]. It reviewed and studied the way to determine the optimum cutting parameters in terms of tool life and operation time by the modified harmony search algorithm. This has predicted the surface roughness using vibration signals acquired in the turning process. Most used algorithms are artificial neural network (ANN), MOGA, genetic algorithm (GA), etc. [8].

2.4. Milling Operation. A total of 5 cases are studied here to know the importance of artificial intelligence (AI) algorithms in milling machining operations [9]. For the high-speed milling process, he developed a model to predict surface roughness based on the backpropagation (BP) algorithm and GA [10]. Shankar et al. [11] studied the effects of machining force and sound pressure to design an efficient tool monitoring system using ANFIS. Garcia-Ordas et al. [12] studied the characterization of tool wear and monitoring using shape and texture descriptors by support vector machine (SVM) and K-NN. Cho et al. [13]explained the effects of cutting force and power consumption on milling machines for the detection of tool breakage using SVM. Wu et al. [14] proposed comparative studies on machine learning (ML) algorithms for the prediction of tool wear using random forests are reviewed. Most used algorithms include GA, K-NN, and SVM.

2.5. Grinding Operation. Despite the fact that very few cases for grinding operations were found for study, efforts to anticipate the prediction of surface finishing quality were reviewed. Gao et al. [15] have attempted to optimize material removal rate (MRR) using the XGBoost algorithm by identifying the undesirable noise and idle time during operations. Zhang et al. [16] utilized many input parameters to monitor the surface roughness of the work material by IFSVR.

2.6. Drilling Operation. Similar to the grinding process, here also a very few cases were found for the study to analyze the finishing quality of the work material. This part contains a summary of 2 papers. Shaban et al. [17] diagnosed the machining outcome by a logical analysis of data for evaluation of product finishing quality and geometric profile by considering process parameters. Shi et al. [18] have studied the characteristics of drilling in real time to detect influx and loss during machining operations using random forests and

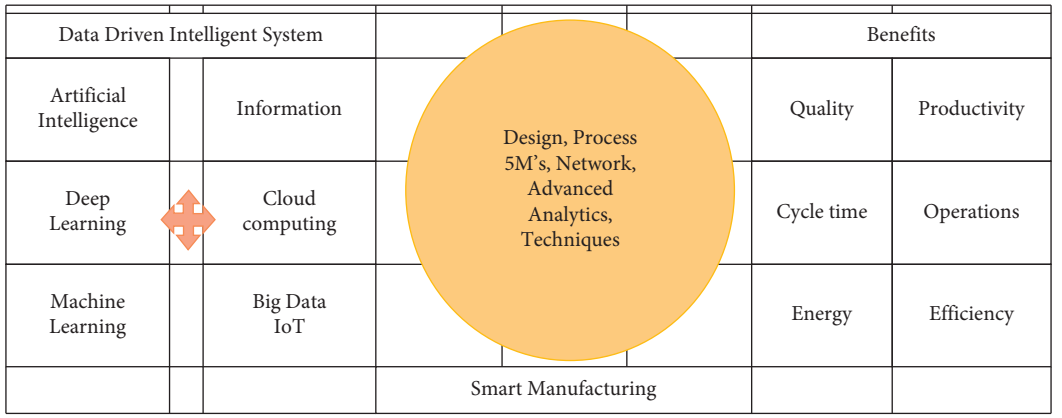

Figure 2: Smart manufacturing: elements and its benefits.

Table 1: Cases of Traditional machining processes using machine learning algorithms.

Sl no	Purpose	Algorithms	Input parameters	Ref. (Year)
1	Optimization of machining parameters	MOGA, AI	Tool path cutting force	[1] (2019)
2	Multi-objective optimization	Modified harmony search Algorithm, GA	Cutting velocity, DOC, feed	[2] (2017)
3	Carbon emission quantification and prediction, cutting parameter optimization	Regression, MOTLBO	Speed, feed, depth of cut	[3] (2015)
4	Surface roughness prediction	Multiple linear Regression (MLR)	Speed, feed, depth of cut, flank wear, vibration	[4] (2015)
5	Microhardness and grain size prediction	RF, GA	Cutting speed, feed rate, tool edge radius, tool coating status	[5] (2015)
Cases of Milling processes using Machining Learning Algorithms				
1	Prediction model of milling surface roughness	Genetic algorithm range analysis	Milling depth, milling row spacing, speed	[6] (2019)
2	Tool condition monitoring	Adaptive neuro-fuzzy Inference, ANFIS model	Sound pressure, Cutting force	[7] (2018)
3	Tool wear monitoring	K-NN, SVM	Tool images	[8] (2017)
4	Tool breakage detection	SVM, SVR	Cutting force and power consumption data	[9] (2005)
5	Tool wear prediction	RF	Cutting force, vibration, Acoustic emission	[10] (2017)
Cases of grinding processes using machining learning algorithms				
1	Monitoring of surface roughness (Ra) and surface shape peak valley	IFSVR	Acoustic emission, grinding force, vibration	[11] (2015)
2	Material removal prediction method	XGBoost learning algorithm	Contact time, belt velocity Mesh size	[12] (2019)
Cases of drilling processes using machining learning algorithms				
1	Evaluation of quality and geometric profile circularity, dimensional error, delamination	Logical analysis of data	Thrust force, cutting force, torque	[13] (2015)
2	Detection of influx and loss	Random forests, support vector machine	Time-indexed drilling measurement parameters	[14] (2019)

support vector machine. The most likely used algorithm in these studies is RF and SVR.

3. Nontraditional Machining

Nontraditional machining is based on the removal of materials mostly by electrical energy. Very less cases are found in the study. The main objective is to improve the finishing quality of a product while optimizing the MRR and Ra predictions. Here, machining processes such as EDM, ECM, LBM, and AJM operations are discussed and summarized in Table 2.

3.1. Electric Discharge Machining Process—EDM. The fundamental reason for implementing ML algorithms is to enhance the surface quality of the product. It was used to investigate the surface integrity, bio-activity, and performance characteristics of WEDM on biomedical alloy for medical applications [19]. Experiments were done on

Table 2: Cases of nontraditional machining processes using machine learning algorithms.

Sl. No.	Purpose	Algorithms	Input parameters	Ref. (Year)
1	Predict optimum process parameter for minimum wear ratio and maximum MRR	BpNN, particle swarm optimization, simulated annealing, GA	Pulse current, pulse-on time, pulse-off time	[15] (2015)
2	Investigations of surface integrity and bio-activity performance	TRMGP	Servo voltage pulse off-time pulse on-time	[16] (2019)
3	Prediction of surface roughness and MRR	Taguchi, GRA ANNs	Pulse on & off time wire feed rate	[17] (2018)
Cases of Electrochemical Machining processes using Machining Learning Algorithms				
1	Process parameter optimization for MRR and Ra	LS-SVM, MFNN, Taguchi technique, ANOVA	Flow rate, feed voltage	[18] (2012)
2	Process parameter optimization for maximizing MRR and minimizing radial overcut	TLBO	Electrolyte concentration, electrolyte flow rate, applied voltage, inter-electrode gap,	[19] (2011)
Cases of laser machining processes using machining learning algorithms				
1	Process monitoring and control	Convolutional neural networks (CNNs)	Beam translation beam rotation	[20] (2019)
2	Prediction of surface quality, dimensional features, and productivity	NN, decision trees, K-NN, linear regression	Scanning speed, pulse intensity, pulse frequency	[21] (2015)
Cases of abrasive water jet machining processes using machining learning algorithms				
1	Surface roughness prediction	Extreme machine learning, ANN, GPR	Cutting speed, material thickness, abrasive flow, measurement position	[22] (2016)
2	Prediction of process parameters	Adaptive neuro-fuzzy inference system	Jet pressure standoff distance number of shots	[23] (2019)
3	Surface roughness prediction	Feed-forward BpNN, regression model	Traverse speed, water jet pressure, stand-off distance, abrasive grit	[24] (2008)

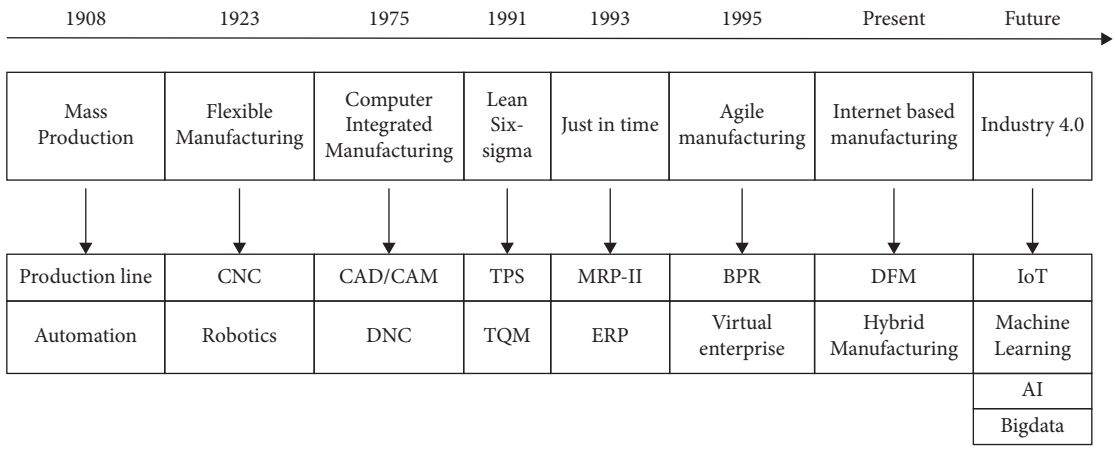

Figure 3: Manufacturing paradigm.

advanced material like composites using RA and ANN. Most of the studies were focused on process voltage, pulse ON/OFF time, wire feed rate, etc.

3.2. Electrochemical Machining Process—ECM. In this process, major focus is on the chemical aspects of the electrolyte used, flow rate, and gap to access and improve the quality of the workpiece. Nayak et al. [20] successfully compared LSSVM and FFNN algorithm to predict MRR and Ra and suggested that LS-SVM is the most powerful machine learning tool. The most likely used algorithm in these studies includes SVR, NN, Taguchi, ANOVA, and TLBO tech.

3.3. Laser Beam Machining Process—LBM. In today's global requirements for the finest quality of products in terms of precision and accuracy, LBM plays a vital role. However, the process parameter is optimized using many algorithms that are dealt with herein. Kang et al. [21] monitored the process and its parameters viz beam translation and beam rotation to control the process using CNNs. Many kinds of NN algorithms were used to monitor and control the process and its

parameter to achieve the predetermined objectives. The study concludes that the productivity rate of this process was found to be high.

3.4. Abrasive Water Jet Machining Process—AWJM. This process mainly emphasizes on prediction of surface roughness and process parameters. Cojbasic et al. [22] predicted the surface roughness of the process using flow, speed, and material thickness as input parameters using ANNs and GPR. Many other researchers have tried a lot to predict using different kinds of ML algorithms to predict the Ra.

A novel revolution for today's industrial settings is to effectively examine the field of machine learning and its impact on smart machining in order to attract worldwide attention. The contextual analyses reviewed in this paper have for the most part been published in the ongoing years.

Evolution of Manufacturing paradigm.

Figure 3 shows the development in the field of manufacturing during the last century. It also explains the importance of advanced manufacturing methods, techniques, and technologies in the industry. By looking at it, one can say that there is significant scope for artificial intelligence and its algorithms in manufacturing to attain a benchmark.

4. Conclusions

Machining strategies play a major role in the substantial growth of the machining industry. The use of ML algorithms is becoming increasingly prevalent in many industries in order to meet market demands in the current global environment. A review of past and present smart machining processes with machine learning algorithms was conducted in this paper, as well as future directions for the machining industry were outlined. Based on the present study, ML algorithms have a huge potential in manufacturing industries.

Data Availability

The data used to support the findings of this study are included in the article.

Conflicts of Interest

The authors declare that they have no conflicts of interest.

References

[1] AfrimGjelaj and B. Berisha, "Optimization of turning process and cutting force using multiobjective genetic algorithm," *Universal Journal of Mechanical Engineering*, vol. 7, p. 64, 2019.

[2] S. Phuyal, D. Bista, J. Izykowski, and R. Bista, "Performance analysis of new SCADA interface developed in C# environment," in *Proceedings of the 2020 IEEE International Students' Conference on Electrical, Electronics and Computer Science (SCEECS)*, Bhopal, India, 2020.

[3] S. Phuyal, D. Bista, J. Izykowski, and R. Bista, "Design and implementation of cost efficient SCADA system for industrial automation," *International Journal of Engineering and Manufacturing (IJEM)*, vol. 10, no. 2, pp. 15–28, 2020.

[4] C. Zhang and J. Yang, *A History of Mechanical Engineering*, Springer, Berlin, Germany, 2020.

[5] R. Farshbaf Zinati and M. R. Razfar, "Multi-objective constrained optimization of turning process via modified Harmony search algorithm," *Iranian Journal of Science and Technology, Transactions of Mechanical Engineering*, vol. 43, 2017.

[6] W. Lin, D. Yu, S. Wang et al., "Multi-objective teaching–learning-based optimization algorithm for reducing carbon emissions and operation time in turning operations," *Engineering Optimization*, vol. 47, no. 7, pp. 994–1007, 2015.

[7] M. Elangovan, N. Sakthivel, S. Saravanamurugan, B. B. Nair, and V. Sugumaran, "Machine learning approach to the prediction of surface roughness using statistical features of vibration signal acquired in turning," *Procedia Computer Science*, vol. 50, p. 282, 2015.

[8] Y. Chen, Y. Sun, L. Han, and B. Zhang, *Prediction Model of Milling Surface Roughness Based on Genetic Algorithms*, Springer Nature Switzerland AG, Berlin, Germany, 2020.

[9] S. Shankar, T. Mohanraj, and R. Rajasekar, "Prediction of cutting tool wear during milling process using artificial intelligence techniques," *International Journal of Computer Integrated Manufacturing*, vol. 32, 2018.

[10] M. Garcia-Ordas, *Wear characterization of the cutting tool in milling processes using shape and texture descriptors*, Ph.D. Thesis, Universidad de Leon, León, Spain, 2017.

[11] S. Cho, S. Asfour, A. Onar, and N. Kaundinya, "Tool breakage detection using support vector machine learning in a milling process," *International Journal of Machine Tools and Manufacture*, vol. 45, no. 3, pp. 241–249, 2005.

[12] D. Wu, C. Jennings, J. Terpenny, R. X. Gao, and S. Kumara, "A comparative study on machine learning algorithms for smart manufacturing: tool wear prediction using random forests," *Journal of Manufacturing Science and Engineering*, vol. 139, p. 7, 2017.

[13] K. Gao, H. Chen, X. Zhang, X. Ren, J. Chen, and X. Chen, "A novel material removal prediction method based on acoustic sensing and ensemble XGBoost learning algorithm for robotic belt grinding of Inconel 718," *The International Journal of Advanced Manufacturing Technology*, vol. 105, 2019.

[14] D. Zhang, G. Bi, Z. Sun, and Y. Guo, "Online monitoring of precision optics grinding using acoustic emission based on support vector machine," *International Journal of Advanced Manufacturing Technology*, vol. 80, no. 5-8, pp. 761–774, 2015.

[15] Y. Shaban, S. Yacout, M. Balazinski, M. Meshreki, and H. Attia, "Diagnosis of Machining Outcomes Based on Machine Learning with Logical Analysis of Data," in *Proceedings of the International Conference on Industrial Engineering and Operations Management*, Dubai, United Arab Emirates, 2015.

[16] X. Shi, "A New Method to Detect Influx and Loss during Drilling Based on Machine Learning," in *Proceedings of the International Petroleum Technology Conference*, Beijing, China, 2019.

[17] T. Titus, "Prediction of surface roughness and material removal rate in wire electrical discharge machining on aluminum based alloys/composites using taguchi coupled grey relational analysis and artificial neural networks," *Applied Surface Science*, vol. 472, 2018.

[18] K. C. Nayak, "Taguchi integrated least square support vector machine an alternative to artificial neural network analysis of electrochemical machining process," *IOSR Journal of Mechanical and Civil Engineering*, vol. 1, no. 3, pp. 01–10, 2012.

[19] H. S. Kang, J. Y. Lee, S. Choi et al., "Smart manufacturing: past Research, present findings, and future directions," *International Journal of Precision Engineering and Manufacturing-Green Technology*, vol. 3, no. 1, pp. 111–128, 2016.

[20] Ž. Ćojbašić, D. Petković, S. Shamshirband et al., "Surface roughness prediction by extreme learning machine constructed with abrasive water jet," *Precision Engineering*, vol. 43, p. 86, 2016.

[21] D. Teixidor, M. Grzenda, A. Bustillo, and J. Ciurana, "Modeling pulsed laser micromachining of micro geometries using machine- learning techniques," *Journal of Intelligent Manufacturing*, vol. 26, no. 4, pp. 801–814, 2015.

[22] Ž. Ćojbâsić, D. Petković, S. Shamshirband, C. W. Tong, C. W. Tong, and S. Ch, "Surface roughness prediction by extreme learning machine constructed with abrasive water jet," *Precision Engineering*, vol. 43, pp. 86–92, 2016.

Hindawi
Journal of Engineering
Volume 2022, Article ID 6559215, 5 pages
https://doi.org/10.1155/2022/6559215

Research Article

Monitoring of an Electromechanical Prototype Material for Environmental Parameters Using IoT

P. Bharat Siva Varma,[1] **Kothapalli Phani Varma**,[2] **V. Anjani Kranthi**,[1] **Anusha Rudraraju**,[3] **and Nalla Nandakishore**[4]

[1]*Department of Computer Science and Engineering, Sagi Rama Krishnam Raju Engineering College, Bhimavaram 534204, India*
[2]*Department of Electronics and Communication Engineering, Sagi Rama Krishnam Raju Engineering College, Bhimavaram 534204, India*
[3]*Department of Information Technology, Sagi Rama Krishnam Raju Engineering College, Bhimavaram 534204, India*
[4]*Dept of Electrical and Computer Engineering, College of Engineering, Wolaita Sodo University, Sodo, Ethiopia*

Correspondence should be addressed to Nalla Nandakishore; nandakishore.nalla@wsu.edu.et

Received 1 June 2022; Revised 30 June 2022; Accepted 5 July 2022; Published 8 August 2022

Academic Editor: Karthikeyan Sathasivam

The Internet of Things (IoT) is a phenomenon where everything is connected to everything, where the development of sensors and microprocessors helped in the rise of embedded technologies, such as Wi-Fi and Bluetooth, and the evolution of bandwidth available on the Internet. This phenomenon will continue unabated due to sensor technology, programmable chips, and embedded technologies. In recent years, the Internet of Things (IoT) has become one of the most prominent technology niches. IoT is the network of interconnected devices or "things" that exchange information or send data with each other over the Internet. The article describes a computer prototype for monitoring and controlling the environmental parameters of a communication equipment room. A technological tool, such as the one obtained, can be implemented in many applications, such as weather stations, food chains, smart home systems, measuring the heart rate of humans, and fruit dehydrators. The article's research was focused on an IoT electronic device and a web platform. A major feature of this electronic device is that its Internet connectivity is achieved using the TCP/IP protocol, an integrated feature of the Shield Ethernet board stacked on top of the Arduino mega board.

1. Introduction

Technological advances have marked the twenty-first century from its earliest years: personal computers are becoming ever smaller, smartphones and tablets are all increasing in popularity, and cloud computing may be one of the most important changes in the information society that we are living in today [1]. A study conducted by the Mexican Internet Association (AMIPCI) in 2015 on Internet usage habits in Mexico reveals that 53.9 million Mexicans use the Internet via their smartphone and spend an average of 6 hours and 11 minutes online each day. The study predicts that this number will continue to rise in the years to come [2]. In total, more than 53 million people connect to the Internet via various devices on average for six hours and eleven minutes every day, generating an outsized amount of data on a daily basis. The development of systems that operate in various ways under various approaches such as Data Warehouses (Data Warehouses) and large data sets (Big Data) has been one of the fruits of the development of branches of information technology that deal with the arduous task of processing this data [3]. Due to their constant miniaturization and mass production, Internet of Things devices is becoming more and more important due to their decreased cost and ability for increasing numbers of people to access and use them. As a result of this, there has been an emergence of a concept known as M2M, which entails those two devices communicating with each other to perform a task [4]. Due to this limited interaction, M2M could only be utilized by specific sectors, including the construction of

smart buildings. The Internet created a paradigm shift in the field of devices with the introduction of the Internet, which became known as the Internet of Things. The physical ojects and their characteristics are used in measuring [5]. There are devices that will allow us to exert an influence on these objects in different ways: census, which refers to taking measurements; control, which directs or indirectly affects their behavior; and act, which allows these objects to make their own decisions based on external conditions and events [6]. However, there have been a number of alternative interconnection mechanisms implemented recently that have not yet been affected by the Internet, the main means of sending and receiving data between objects. This article describes the design and development of an IoT system for the Central American Corporation of Air Navigation Services, COCESNA [7]. An electronic device connected to a LAN and the Internet is used to measure the physical properties of an environment through sensors. This web portal includes, as the main element, a Dashboard or an interactive graphic that displays the information sent by the IoT device; it also describes a mobile application on the Android operating system that allows real-time monitoring of physical magnitudes, such as temperature and humidity [8]. A web portal describes the connectivity of the information, which can be scaled and added to the country at the Central American level.

2. Methodology

It is a project management technique widely used in the IT industry and by large companies. It is the main advantage of this kind of approach that it allows for flexibility and capacity to modify the product during the project since it is used as it is being developed. An objective was determined to develop an IoT system that monitors data through a wirelessly attached electronic device connected to a web portal to display the data dynamically in real-time using a web portal connected to the Internet. An IoT system, developed in sprints, consists of an electronic device with sensors to measure preselected physical parameters of the environment such as temperature, humidity, and movement. It is LAN and Internet connection and conforms to COCESNA specifications. An IoT device dashboard or interactive graphics can be displayed on the web portal as part of its main pictorial element. The web portal has the option to scale and add new control rooms per country in Central America. The application interacts with an Android operating system to monitor physical quantities, such as temperature and humidity.

2.1. IoT System Elements. The research was conducted in the previous study to examine alternative IoT systems that can be constructive. It was determined what type of electronic device should be developed via the weighted criteria method. The system to be implemented has been determined to be one with Internet connectivity via Ethernet since Wi-Fi is out of the question due to the fact that a frequency inhibitor or signal blocker is already installed in the Women's Prison nearby the COCESNA facilities. A web portal controls objects based on a parameterized threshold based on temperature or humidity. Additionally, e-mail and SMS notifications of "all/nothing" actions can be incorporated into the web portal. As a result, the information is agile and timely enough for immediate decision-making and to prevent equipment damage. The electronic device, as shown in Figure 1, consists mainly of a controller board for the complex electronics (Arduino/brain), an Ethernet shield, sensors and actuators (indicators), a relay interface for high-voltage loads (DC/AC), switches to start and stop the device, and an LCD monitor for displaying sensor data. There is also a cooling system consisting of two side coolers. In an open-source development environment based on the Processing programming language, it is based on an open-source hardware and software platform with analog and digital sensors.

2.2. Arduino. An open-source, hardware and software platform that employs an analog and digital board with computer inputs and outputs, as well as the processing programming language. A prototyping platform using open-source hardware and software. The log-in page is shown in Figure 2.

2.2.1. Ethernet Shield. A shield designed for Arduino allows connecting to an Ethernet network. A TCP/IP protocol stack is implemented on a physical level by the protocol stack. The protocol stack utilizes the Wiznet W5100 Ethernet chip. It supports both TCP and UDP over an IP network stack. A connection-oriented protocol is TCP, and a connectionless protocol is UDP. TCP is comparatively slower than UDP, which makes it a key difference between the two protocols. In general, UDP is faster, simpler, and more efficient than TCP, but TCP is a connection-oriented protocol, while UDP is a connectionless protocol. Four socket connections can be made simultaneously. Reading and writing data streams over the Ethernet port are handled using the Ethernet library. This shield enables sketches to connect to the Internet. It is powered by a 32 bit Xtensa Dual-Core LX6 processor running at 160 or 240 MHz. The ESP8266 architecture relies on two cores, one of them dedicated to IP and WIFI communication, the other to the rest of the tasks, which solves one of the most significant difficulties. The ESP8266 architecture has one of the biggest challenges. There is 520 kB of RAM memory available to both processors, and it can use an additional 8 MB of external RAM memory.

2.3. Electronic Interface. The control interface is designed using transistors and relays. As the Arduino microcontroller's output pins are limited to between 10 and 30 mA, the higher required current can damage the pin programmed as an output. In order to handle higher currents, transistors are used, while a relay is used to handle currents that are significantly higher than those that can be handled by a BJT transistor, as well as providing isolation to handle the alternating current. The bipolar junction

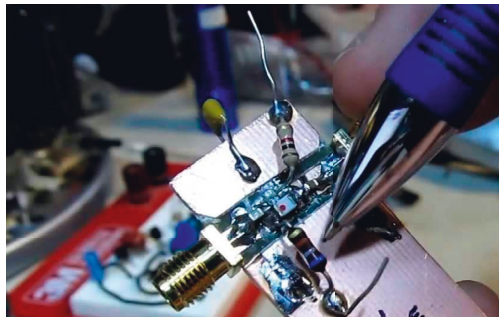

Figure 1: Prototype construction.

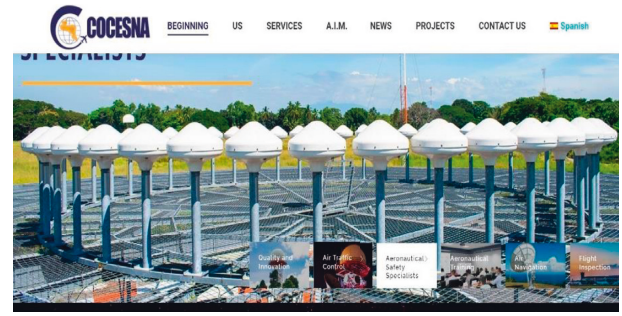

Figure 2: Log-in page.

transistor (BJT) is used as an amplifier, filter, rectifier, oscillator, or even as a switch, as we illustrate in the first section. Transistors biased into the linear region will act as amplifiers or other linear circuits. There is also a Darlington transistor shown in the diagram, which allows the relay coil to be energized by connecting the optocoupler (the device transmits electrical signals between two isolated circuits by using an LED that emits infrared light and a photosensitive device that detects the light) to the NPN transistor. Various semiconductor materials can be used to make NPN transistors, including silicon and germanium. NPN transistors are formed when two n-type semiconductor materials are fused with p-type semiconductor materials. An NPN transistor is made of semiconductor materials such as silicon or germanium. A transistor is connected to the microcontroller through an optocoupler, which isolates the currents flowing through the transistor from the microcontroller output so that an LED is powered by the optocoupler, which feeds the transistor's base in its simplest form. The device functions as a switch that is controlled by an electronic circuit consisting of resistors limiting the current, an optocoupler controlling the transistor, and a rectifier diode protecting the transistor. In the transistor, the output of the relay is controlled and the internal electromagnet is actuated, enabling the contacts to open or close and being capable of controlling an output circuit of larger power than the input circuit, in a general sense, like electrical amplifiers.

2.3.1. Sensor. Instrumentation variables are physical variables that are converted into electrical variables by a device called an instrumentation variable. An active sensor injects light, microwaves, or sound into an environment and determines if the environment has changed. The detection of infrared waves is used by many alarms and passive sensors. This type of sensor is known as a passive infrared sensor (PIR). An infrared passive sensor measures the infrared light emitted by objects within its field of view. The most common application of these sensors is in motion detectors based on PIR technology. A PIR sensor is commonly used in security alarm systems and automatic lighting systems. A sensitivity adjustment must be made to one of these sensors in order to detect human body heat. In order to implement an IoT system via Wi-Fi electronic cards, the following can be used: based on the popular chip (ESP8266) that revolutionized embedded systems with Wi-Fi, the node MCU development board is equipped with a board. The device (ESP32) is much more capable, not only because it is faster but also because it is designed to function as a microcontroller in IoT applications.

2.3.2. Actuator. A pneumatic or electric hydraulic actuator is capable of transforming energy into mechanical power and triggering a process or device in order to increase efficiency. An order is received from the regulator or controller, and the control element is activated in response, such as an air conditioner, fan, or valve. Depending on what instructions the control unit sends, these elements directly affect the output signal of the automation.

2.4. Experimental Development. A communication test between the parts of the developed IoT system was performed to verify its correct operation. These are shown in Figures 3–6.

2.5. The Brain of the System. Data exchange between the Arduino Mega and Ethernet shield is carried out by the Arduino Mega and Shield attached. Sensor data is collected by the Arduino Mega and processed by the shield. Arduino boards use a mega 2560 microcontroller to provide open-source. This board's growth environment is used to execute the processing or wiring language. This information is also sent to the Ethernet shield, which, thanks to its characteristics, and allows the data to be uploaded to local servers with the TCP/IP protocol. A sensor is an element that gathers and analyzes information from the environment, which is then sent to the controller card or brain of the system for processing, while at the same time being sent to the network through the Ethernet shield. A high-voltage 120VAC load can be controlled with these devices, which consist of an electronic interface and relay modules. The Arduino Mega board controls the relay modules using TTL signals. These electronic interfaces allow you to control objects such as air conditioning and fans.

2.6. Web Server. HTTP (Hypertext Transfer Protocol) is an application that serves web pages to users, in response to requests forwarded by HTTP clients of its equipment, based on the HTTP (Hypertext Transfer Protocol) protocol.

Figure 3: Humidity visualisation graph.

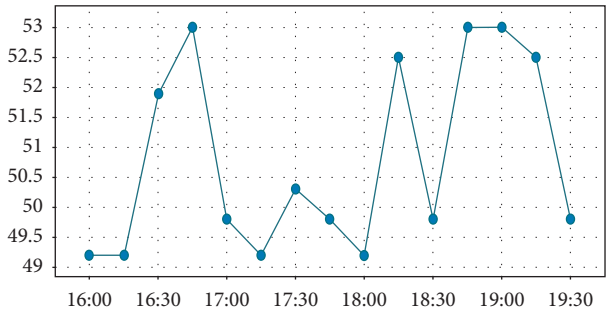

Figure 4: Temperature visualisation graph.

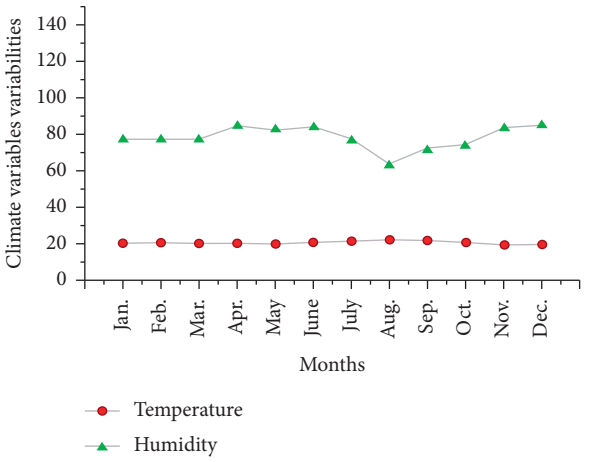

Figure 5: Statistical graph of monthly temperature and humidity.

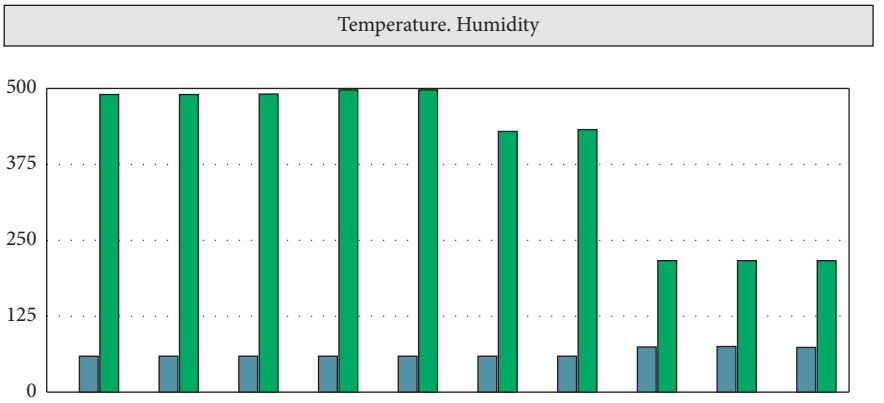

Figure 6: Bar graph views of temperature and humidity.

2.7. Router. An interconnector is a piece of hardware that allows computers in a network to communicate. In addition to environmental parameter information, the IoT device is built to send other data to the server as well. As a prerequisite to sending the information to the remote server, the router's administration website must be accessed in order to make basic configurations such as enabling the port on which it listens and responds to incoming and outgoing requests and reserving the IP address for the IoT device using its MAC address. The MAC address is a unique identifier that is assigned to a network interface controller so that it can be used as a network address during communications within a network segment. This technique is consistent with how the DHCP server of a router or network operating system determines whether the device obtains the same network identifier (IP address) over time.

2.8. Dashboard. As part of this article, you will be presented with graphical representations or user interfaces that allow you to view information handled by a system, for example, temperature, humidity, movement, communication testing signal, and SW on/off graphs. A dashboard is a control panel, which contains the instruments and controls and faces the driver of a vehicle or pilot of an aircraft.

2.9. Web Portal. There are websites and Internet portals that offer easy and integrated access to a range of resources and services related to the same subject. This portal presents a series of graphical elements to display information gathered by the IoT device in this case study. A prototype for cloud computing was tested locally as a first step to determine if it could be developed and scaled for the cloud. The results are shown in Figure 6. Computing services can be offered over a network, typically the Internet, under a cloud computing system. Cloud services are also known as cloud computing or cloud computing services.

3. Conclusions

In this article, we have discussed the concept of the Internet of Things (IoT) developed in the project, including its characteristics. An IoT electronic device connected to the cloud has been proposed as a solution for interconnecting objects with Internet access; this device then functions as a hub or HUB for connecting objects to the system via IO (input/output) ports, digital and analogue channels. As many elements as there are IO channels on the mainboard, the IoT device can control objects and monitor them with electronic instrumentation. This device was built with an Arduino Mega, which has 54 digital inputs/outputs, of which 14 can be used as PWM outputs, 16 analog inputs, and four hardware serial ports. There is a 16 MHz crystal oscillator on the board that can be programmed using a computer via USB. We developed an IoT system using low-cost hardware and software that included the ability to communicate with other applications so that business processes could be enhanced. We used devices such as sensors and actuators to generate solutions tailored to the needs of the productive sector. The purpose of this project was to explore the application of the Internet of Things in different sectors of the El Salvadorian economy. A monitoring opportunity of the equipment rooms of COCESNA was identified in coordination with the association. It has enabled these rooms to maintain environmental parameters within the tolerances defined by COCESNA or by the manufacturer, such as temperature and humidity, through continuous monitoring and recording. It also provides timely alerts or notifications through e-mails. In the event of possible overheating that may impair the availability of the equipment's service, the risk to its operational stability has been reduced, and actions can be taken accordingly.

Data Availability

The data used to support the findings of this study are included in the article.

Conflicts of Interest

The authors declare that they do not have any conflicts of interest regarding the publication of this paper.

References

[1] B. J. Black, *Workshop Processes, Practices and Materials*, Routledge, England, UK, 5th edition, 2015.

[2] D. Moure, P. Torres, B. Casas et al., "Use of low-cost acquisition systems with an embedded Linux device forvolcanic monitoring," *Sensors*, vol. 15, pp. 20436–20462, 2015.

[3] F. Salfner, M. Lenk, and M. Malek, "A survey of online failure prediction methods," *ACM Computing Surveys*, vol. 42, no. 3, pp. 1–42, 2010.

[4] G. Casale, N. Mi, and E. Smirni, "Model-driven system capacity planning under workload burstiness," *IEEE Transactions on Computers*, vol. 59, no. 1, pp. 66–80, 2010.

[5] J. Liu, Y. Li, M. Chen, W. Dong, and D. Jin, "Software-defined internet of things for smart urban sensing," *IEEE Communications Magazine*, vol. 53, no. 9, pp. 55–63, 2015.

[6] M. Ambrož, "Raspberry Pi as a low-cost data acquisition system for human powered vehicles," *Measurement*, vol. 100, pp. 7–18, 2017.

[7] M. V. S. Babu1, A. Rama Krishna, and K. N. S. Suman, "Review of journal bearing materials and current trends," *American Journal of Materials Engineering and Technology*, vol. 4, pp. 72–83, 2015.

[8] N. Janevski and K. Goseva-Popstojanova, "Session reliability of web systems under heavy-tailed workloads: an approach based on the design and analysisof experiments," *IEEE Transactions on Software Engineering*, vol. 99, pp. 1–22, 2013.

Hindawi
Journal of Engineering
Volume 2022, Article ID 6903695, 5 pages
https://doi.org/10.1155/2022/6903695

Research Article

Improving the Security of Video Embedding Using the CFP-SPE Method

Karthick Panneerselvam,[1] K. Rajalakshmi,[2] V. L. Helen Josephine,[3] Dhivya Rajan,[4] L. Visalatchi,[5] K. Mahesh,[1] and Meroda Tesfaye[6]

[1]*Department of Computer Applications, Alagappa University, Karaikudi, India*
[2]*Department of Computer Science, Montfort College, Bengaluru, India*
[3]*Business Analytics, School of Business Management, Christ University, Bengaluru, India*
[4]*Department of MCA, CMR Institute of Technology, Bengaluru, India*
[5]*Department of IT, Dr. Umayal Ramanathan College for Women, Karaikudi, India*
[6]*Addis Ababa Science and Technology University, Addis Ababa, Ethiopia*

Correspondence should be addressed to Meroda Tesfaye; meroda.tesfaye@aastu.edu.et

Received 14 June 2022; Accepted 5 July 2022; Published 30 July 2022

Academic Editor: Karthikeyan Sathasivam

With the amount of data being transferred on a daily basis, it is becoming increasingly dangerous to save data on the Internet in the face of intruders or hackers. This study paper is one of the most effective ways to transmit information in a secure and confidential manner. The authors previously disclosed a way for embedding a secret video inside a cover video in their prior work. The writers have implemented a number of techniques to incorporate the secret video. The current work improves on the existing approach by including encryption and decryption concepts into the video embedding process. The secret data for either a large or little amount of information is put on the cover video utilising the embedding technique. Our proposed method combines compression, encryption, decryption, and secret information embedding to provide a more secure data transfer.

1. Introduction

Video embedding is a new field of study that aims to provide secure data transmission. Frames from the video file were used to hide data in the process of video data concealing [1]. Large amounts of data can readily be embedded behind the frames of a file due to the use of frames. The goal of the secure video data hiding approach is to insert hidden information in multiple bits of pixels. In the discrete wavelet transform domain of the cover video, the concealing approach is applied. Effective decryption is the key issue that arises during the video encryption process. Quantization employing cosine transformations or wavelet transformations may not be able to restore the encrypted input video frame more successfully during the compression process. Pixel information was lost when employing transforms [2]. The pixel information was adequately kept during the encoding process; however the encryption efficiency was not increased. As a result of the existing methods, the video frame size was initially lowered by combining the current and prior pixels [3]. The encryption procedure is based on the pixel grouping and substituting the relevant and recurrent pixels with the message information, and the problem was solved using effective block code creation. The size of the resultant image is approximately half that of the input image [4] (see Table 1).

2. Literature Review

The survey suggests that there are benefits and drawbacks to the current video security methods. However, most methods have significant drawbacks when it comes to embedding videos, such as:

Table 1: Literature review.

Author and year	Technique	Observation
Alhaj (2016)	Multilayer image stegnaography	According to video steganography, six bits of the secret message can be used to decipher the hidden message.
Manimegalai (2014)	Peak-shaped technique	For the purposes of spatial demonstration, multiple steganography algorithms for JPEG images were thoroughly analyzed.
Mstafa et al. (2017)	(MOT) algorithm and error correcting codes (ECC)	Algorithms for video steganography have been developed in the DCT and DWT domains, respectively. Hamming and bose, chaudhuri, and hocquenghem (BCH) codes were used to encrypt the secret data in the communication.

(i) Unreliable compression ratio

(ii) It is less time-efficient, less secure, and requires more effort.

(iii) Memory complexity is another drawback.

The goal of this research is to create a novel method for video embedding in order to solve these problems.

2.1. Advantages of Steganography Over Watermarking. The types of video embedding techniques are watermarking and steganography. Using wavelet coefficients for information concealment, watermarking is an effective technique that is mostly utilized in the field of image authentication and protection. The following are some of the disadvantages of watermarking in comparison to steganography:

(i) Extensive complexity

(ii) The efficiency must be increased using a rate distortion-optimized rate control.

(iii) High sensitivity to document skewing; poor immunity to manipulation; image quality may be reduced as opposed to watermarking, steganography has the following advantages:

(iv) The embedded video is more sophisticated, making it harder for an attacker to abuse it, and the video stream is used as a cover file in this method, which maximises protection against attackers.

(v) Additionally, it reduces the payload and additional strain.

(vi) Offers both high-quality images and videos.

Thus, the goal of this work was to use steganography to conduct video embedding. When processing video as a series of frames, it conceals the information to provide great security. Additionally, it removes redundant data while enhancing security.

3. Proposed Work

The input and secret video are pre-processed by the supple rectification method and contaminated in the pixel grouping in the proposed method. In this work, the video's white Gaussian noise is removed using preprocessing. The shade picture element (SPE) algorithm is used to process the embedded segment. The code is made up of the results of each patch [5]. Decrypted images can be retrieved by performing a similar operation on the receiver side. Because it is completely reversible, the technology can be utilized to transmit sensitive information in extremely secure videos. The process' performance is assessed using the input and decompressed image's MSE, PSNR, capacity, BER, and SSIM picture quality analyses, and compression ratios. The new method outperforms the old one in terms of effectiveness [6]. Figure 1 shows the block diagram of proposed work.

In this method, following the major steps involved a complete process of information hiding in video sequences.

(1) Input the cover and Stego video

(2) Frame conversion

(3) Preprocessing

(4) Generate the embedding

(5) Encoding the process

(6) Decoding the process with reversible extraction.

(7) Measure the performances.

We have two distinct ways for video embedding:

(i) We can use the supple rectification algorithm to preprocess the video frames.

(ii) We can use the shade picture element algorithm to incorporate the video.

The MATLAB software is used to simulate and evaluate this strategy. The major steps in developing the embedding algorithm are listed below.

3.1. Embedding Part

(i) Read cover video and Stego video file

(ii) Divide the video into frames.

(iii) Using the supple rectification filtering algorithm, select the frames for preprocessing (SRF).

(iv) Initially, this SRF method is utilized to reduce noise in the cover and stego videos.

(v) Use the shade picture element (SPE) approach to group pixels after preprocessing.

(vi) The precompiled cover image pixel is combined with the precompiled secret picture pixel to conduct the embedding procedure.

(vii) For video encoding, the cipher frame pattern (CFP) is used after the embedding procedure.

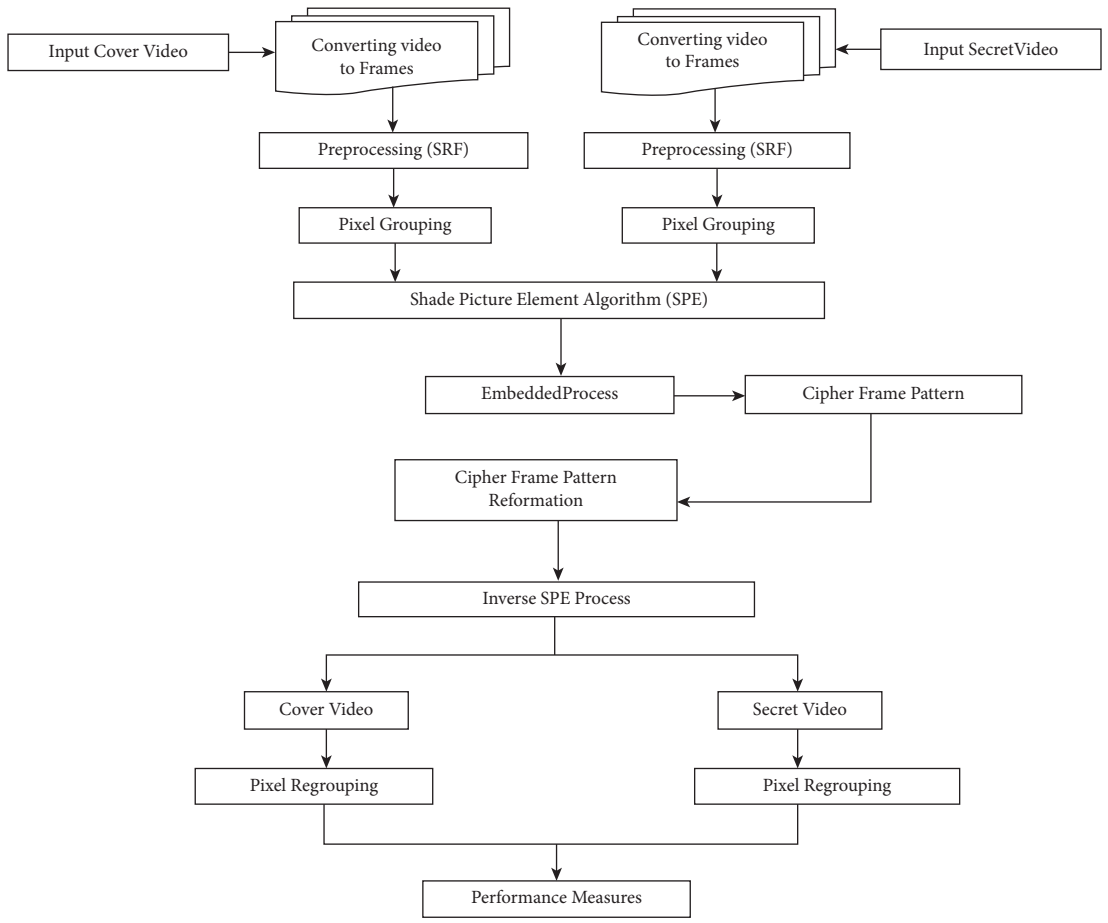

Figure 1: Block diagram of proposed work.

3.2. Extraction Part

(i) Using the reverse technique, extract the hidden video from the stego video.

(ii) To extract cover and stego video, use reversible CFP.

(iii) Using the SPE algorithm's reverse process, regroup the pixels.

(iv) Using the reverse procedure, decode the encrypted video and obtain the original video

4. Experimental Results

This proposed method was used to make common video sequences like news, container, mobile, Akiyo, etc. Here are the results:

Figure 2 depicts a screenshot of a selected video file that is used as a cover video, while Figures 3 and 4 depict a screenshot of a selected video file that is used as a stego video. After then, when the video is delivered to the target receiver, the secret video is embedded using the SPE algorithm, and the video is then reconstructed after the cover and stego video is extracted [7]. A screenshot of the reconstructed video is shown in Figure 5. The reverse methods of picture embedding and pixel grouping are used at this level. In this case, reverse encoding is used to extract the embedded frame from the compressed video sequence. The video is finally

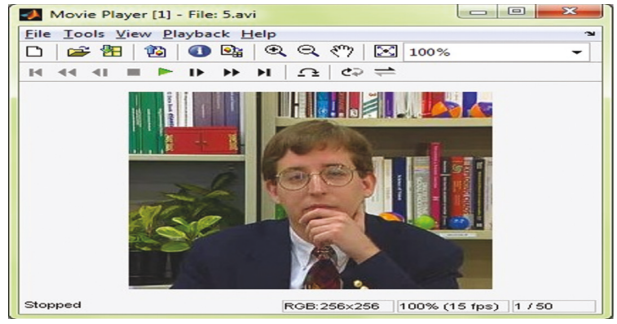

Figure 2: Cover video.

rebuilt by mixing the message frame and cover frame with the least amount of pixel loss possible. There are additional video clips available for the experimental outcomes. As an illustration, we included one sample in a paper. However, we tested a total of 20 samples.

4.1. Performance Analysis. In the first step of testing, video data is taken and hidden using the proposed method. To check the influence of data hiding in the quality of the stego frames [8], performance measurements such as the peak signal-to-noise ratio (PSNR) and mean squared error (MSE) are utilized.

Figure 3: Stego video.

Figure 4: Embedded video.

Figure 5: Reconstructed video.

4.1.1. Peak Signal-To-Noise Ratio (PSNR). Peak signal-to-noise ratio (PSNR) is a common metric used to compare encoded and unencoded video quality. The decibel (db) scale is used to characterize it, as seen in the following [9].

R is the maximum allowable pixel value in the image, and MSE is the mean squared error.

4.1.2. Mean Squared Error (MSE). The MSE is the difference between some of the encoded video's pixel value and the uncompressed video's pixel value.

Table 2: Performance analysis of proposed techniques.

Video sequences	PSNR (dB)	MSE
News	58.42	0.09
Bus	48.56	0.91

Table 3: PSNR value of both existing and proposed techniques.

Video sequences	PSNR original frame	PSNR of reconstructed frame	
		Shamir's (t, n) with DCT	Proposed result
News	37.74	37.19	37.5
Bus	36.47	35.62	36.11

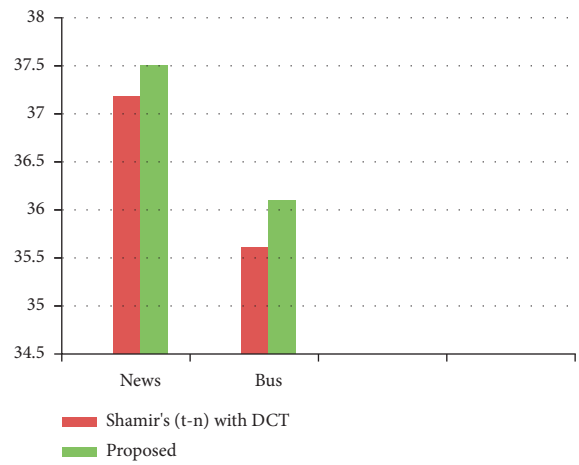

Figure 6: PSNR value comparison.

The MSE is estimated by applying Eq. to arrive at the PSNR (2). HSI band image rows and columns are R and C, respectively [10]. Based on the metrics of time and memory usage during the steganography process, the complexity of the proposed job is validated. By taking into account how long pixel grouping and frame fusion take, the work's time complexity is calculated.

Table 2 illustrates the results of the proposed strategies' performance evaluations. When compared to other video sequences, the news and bus footage has a higher PSNR value and lower MSE value.

Several characteristics, such as PSNR and MSE, are shown in Table 3 to compare the proposed CFP-performance SPE's to that of the existing Shamir's (t, n) with the DCT technique. This study's findings show that the CFP-SPE algorithm, as presented, delivers improved embedding results with great visual quality and great robustness [11]. The results show that the suggested technique produces the best outcomes for all of the video sequences. Therefore, the suggested technique is better suited for various video samples. The PSNR and MSE of each and every video can then differ, and this is entirely dependent on the type of video. As a result, the PSNR and MSE serve as the foundation for the video embedding system's performance rate. Figure 6 shows the PSNR value comparison.

4.2. Features of Our Advanced Video Embedding

(i) Highly secure
(ii) Accuracy
(iii) Improves capacity
(iv) Less Impressibility
(v) Video error correction
(vi) More privacy

5. Conclusions

A video embedding method was proposed in this study to address the challenges that come during the data concealment process. The problem of lossy information is solved by including pixel grouping as well as preprocessing into the embedding process. Optimization and SRF analysis employing varying boundary coefficients of cover and secret video frames are the preprocessing techniques used in the supple correction algorithm approach. The SPE algorithm is used to blend the secret message's pixel information with the necessary pixel information from the cover frame. Last but not least, the video encoding process, also referred to as the suggested method, accomplishes security using the CFP algorithm.

Data Availability

The data used to support the findings of this study are included in the article.

Conflicts of Interest

The authors declare that they have no conflicts of interest.

Acknowledgments

This work was performed as a part of the employment of institutions.

References

[1] S. Alzhair and A. Borici, "An innovative lossless compression method for discrete- color images," *IEEE Transactions on Image Processing*, vol. 21, no. 1, 2015.
[2] S. khosla and P. Kaur, "Secure data hiding technique using video steganography and watermarking—a review," *International Journal of Computer Applications*, vol. 95, 2014.
[3] B. A. Usha, N. K. Srinath, and N. K. Cauvery, "Analysis of video steganalysis techniques to defend against statistical attacks—a survey," *International Journal of Engineering Research and Technology*, vol. 1, 2021.
[4] B. RaviKumar and P. R. K. Murti, "Data security and authentication using stegnaography," *International Journal of Computer Science and Information Technologies*, vol. 2, no. 4, pp. 1453–1456, 2011.
[5] S. Sonali, S. Ekhande, P. Sonavane, and P. J. Kulkarni, "Universal steganalysis using feature selection strategy higher-order video," *Statistics and Information*, vol. 1, p. 19, 2013.
[6] K. Rajalakshmi and K. Mahesh, "A review on video compression and embedding techniques," *International Journal of Computer Applications*, vol. 141, p. 12, 2016.
[7] S. Khosla and P. Kaur, "Secure data hiding technique using video steganography and watermarking," *International Journal of Computer Application*, vol. 95, no. 20, pp. 7–12, 2014.
[8] T. M. Thomas, ""Efficient video watermarking with SWT and empirical PCA based decoding" IOSR," *Journal of Computer Engineering (IOSRJCE) ISSN*, vol. 16, no. 5, 2014.
[9] K. Wong, K. Tanaka, K. Takagi, and Y. Nakajima, "Complete video quality-preserving data hiding," *IEEE Transactions on Circuits and Systems for Video Technology*, vol. 19, no. 10, pp. 1499–1512, 2009.
[10] P. Roy and A. Nath, "New Steganography approach using encrypted secret message inside Audio and Video media," *International Journal of Advance Research in Computer Science and Management Studies*, vol. 2, pp. 46–59, 2014.
[11] D. Xu, R. Wang, and Y. Q. Shi, "Data hiding in encrypted H.264/AVC video streams by codeword substitution," *IEEE Transactions on Information Forensics and Security*, vol. 9, no. 4, pp. 596–606, 2014.

Hindawi
Journal of Engineering
Volume 2022, Article ID 2933444, 4 pages
https://doi.org/10.1155/2022/2933444

Research Article

CFD Simulation of Pressure and Velocity Drop on Y-Type Fuel Injectors

Tarun Kumar Kotteda,[1] **Sudheer Kumar Varma Namburi**,[1] **Prasada Raju Kantheti**,[1] **Ravi Varma Penmetsa**,[1] **and Velivela Lakshmikanth Chowdary**[2]

[1]*Department of Mechanical Engineering, Sagi Rama Krishnam Raju Engineering College, Bhimavaram 534204, India*
[2]*Department of Mechanical Engineering, International Associate, Wolaita Sodo University, Sodo, Ethiopia*

Correspondence should be addressed to Velivela Lakshmikanth Chowdary; lucky.19862@gmail.com

Received 27 May 2022; Revised 20 June 2022; Accepted 22 June 2022; Published 15 July 2022

Academic Editor: Karthikeyan Sathasivam

Hydrocarbon injection is an important stage in combustion, where the atomisation process is involved the atomisation process which consists of disintegrating the fuel into small droplets, through an injector to add more transfer area, the fuel, through an injector to add more transfer area. The size of droplet size generated by the injector must be less than 80 μm to ensure good combustion and avoid combustion and avoid pollutants such as CO and NOx. This research worked with ethanol, a low-emission hydrocarbon, which has a high viscosity which makes it difficult to achieve the correct droplet diameter. This type of study needs to be both theoretical and experimental with simulation being a great tool to replace the latter. The finite element method included in the Flow Simulation package of the SolidWorks software was used in this research. The Flow Simulation package of the SolidWorks software was used, where a Y-type injector was sketched to be evaluated. The dynamic simulation helped to measure the velocity field, at the outlet of the air nozzle, a cavity with a diameter of 0.4 mm, which helps to increase the kinetic energy of the air. The kinetic energy of the fluid obtains the highest values of the Mach number in this area.

1. Introduction

Since the 19th century, mankind has been using oil as a fuel. However, this resource is becoming scarce on our planet. The new vision of sustainability demands that any process is in harmony with the environment, society, and the economy and needs new alternatives that address these three parameters [1]. We are currently talking about alternative fuels, which offer a very interesting alternative to diesel in terms of emissions, wear and tear cost, and availability. Injectors are responsible for the atomisation of the fuel for a combustion process in an engine or a furnace. Atomisation is a process characterised by the transformation of a mass of liquid into a spray or other physical dispersion of droplets in a gaseous atmosphere. This is accomplished by the kinetic energy carried by the fluid [2]. The study of injectors for alternative fuels such as biodiesel ethanol and pyrolytic oil is a very important line of research in recent years since its progress provides alternatives to industrial processes [3]. Y-type injectors are widely used in a steam generation used in steam generation, electric power generation, and furnaces where they serve the function of atomising small droplets of the liquid fuel to be fed into the combustion chamber. Most of the currently used fuels currently used, such as diesel, fuel oil, jet fuel, and petroleum, are alternatives that have caused a lot of damage to our planet. In view of the population being dependent on energy, new solutions have hydrocarbons such as methanol, hydrogen, propanol, and biodiesel which are alternatives to be able to continue to generate the necessary energy but without polluting [4]. These new alternatives require technological changes in the accessories that are part of the combustion process. In this work, we do not focus on the atomisation in the injector, for which it will be necessary to study the main parameters that influence this process. One of these renewable fuels is ethanol, which can be produced from a large number of fuels. Bioethanol has the

same characteristics and chemical composition as ethanol as it is the same compound. Bioethanol has to be obtained from biomass and cannot be obtained from petroleum. These studies require a theoretical and experimental and experimental analysis of the different variables involved in the atomisation process. The works cited above compare numerical results with experimental data of injection systems. The fundamentals of fluid mechanics can be applied to discover how much energy is needed to achieve the required velocities and adequate pressure to achieve adequate atomisation. The flow in an injector was analyzed which used a computer model and the CFD program model, and the CFD program FIRE, to find the flow rate.

2. Material and Methods

The present study shows a graphical analysis using computational fluid dynamics (CFD) which is one of the branches of fluid mechanics that uses numerical methods and algorithms to solve and analyse fluid flow problems. This work requires a computer which will be used to perform millions of calculations required to simulate the interaction of ethanol and air inside the injector cavities. It should be noted that even with simplified equations and with a suitable high-performance computer, only approximate results for most iterations were obtained. SolidWorks helps mechatronic systems be developed from beginning to end. In its initial stage, the software is used for planning, conceptualizing, visualizing, modeling, assessing feasibility, prototyping, and managing projects. As a result, mechanical, electrical, and software elements are designed and constructed via the software. The method consists of discretising a region of space by creating a spatial grid, by dividing a region of space into small control volumes. It is solved in each of them, and the discretised conservation equations are then solved in each so that in effect, an algebraic matrix is an algebraic matrix in each cell iteratively until the residual is sufficiently small [5].

The equations for continuity, momentum, energy, turbulent kinetic energy, and energy by turbulent dissipation are given in equations (1)–(5).

Continuity

$$\frac{\partial}{\partial x_i}\left(\rho u_i\right) = 0. \tag{1}$$

Momentum

$$\frac{\partial}{\partial x_i}\left(\rho u_i u_k\right) = \frac{\partial}{\partial x_i}\left(\mu \frac{\partial u_k}{\partial x_i}\right) - \frac{\partial P}{\rho x_i}. \tag{2}$$

Energy

$$\frac{\partial}{\partial x_i}\left(\rho u_i t\right) = \frac{\partial}{\partial x_i}\left(\frac{\partial t}{\partial x_i}\frac{k}{c_P}\right). \tag{3}$$

Turbulent kinetic energy

$$\frac{\partial}{\partial x_i}\left(\rho u_i k\right) + \frac{\partial \rho k}{\partial t} = \frac{\partial}{\partial x_i}\left(\left(\mu + \frac{u_t}{\sigma_k}\right)\frac{\partial}{\partial x_i}\right) + S_k. \tag{4}$$

Energy by turbulent dissipation:

$$\frac{\partial}{\partial x_i}\left(\rho u_i \varepsilon\right) + \frac{\partial \rho \varepsilon}{\partial t} = \frac{\partial}{\partial x_i}\left(\left(\mu + \frac{u_t}{\sigma \varepsilon}\right)\frac{\partial \varepsilon}{\partial x_i}\right) + S_\varepsilon. \tag{5}$$

Here, P_B represents the generation turbulent due to the forces off low at and can be written as

$$P_B = -\frac{g_i}{\sigma_B}\frac{1}{\rho}\frac{\partial \rho}{x_i}, \tag{6}$$

where "g_i" is the component of gravitational acceleration in the direction x_i, the constant $\sigma_B = 0.9$, and the constant C_B is defined as $C_B = 1$ when $P_B > 0$, or otherwise 0

$$f_1 = 1 + \left(\frac{0.05}{f_\mu}\right)^3,$$
$$f_2 = 1 - \exp\left(-R_T^2\right). \tag{7}$$

The constants C_μ, $C_{\varepsilon 1}$, $C_{\varepsilon 2}$, C_ε, and C_k are empirically defined. In AppFlow Simulation, the typical values used are as follows:

$$C_\mu = 0.09,$$
$$C_\varepsilon = 1.3,$$
$$C_{\varepsilon 2} = 1.92, \tag{8}$$
$$C_{\varepsilon 1} = 1.44,$$
$$C_k = 0.$$

The evaluation of the mean mass requires a formula already developed by Wigg (1959), who analyzed the mechanism of atomisation with air jets, emphasising the importance of the kinetic energy of the atomising air, and indicated that the energy difference between the air jet in the inlet and the emerging spray is a dominant factor affecting the mean droplet diameter. In 1964, using experimental data from other researchers on the atomisation of viscous liquids and air in Y-type injectors, Wigg succeeded in deriving a dimensionless expression which allows to evaluate the mass median diameter of the spray droplets [5]:

$$D_{\mathrm{MMD}} = \frac{200V^{0.5}m_F^{0.1}\left(1 + m_F/m_A\right)0.5h^{0.1}\sigma^{0.2}}{\rho A T^{0.3}\Delta U}, \tag{9}$$

where D_{MMD} = mass mean diameter of the spray drops (μm), V = kinematic viscosity of ethanol (cSt), m_{f} = mass flow of ethanol (g/s), m_{A} = air mass flow (g/s), h = chamber diameter mixture (cm), σ = surface tension of ethanol(dynes/cm), ρAT = air density (g/cm^3), and ΔU = air speed of atomization (m/s).

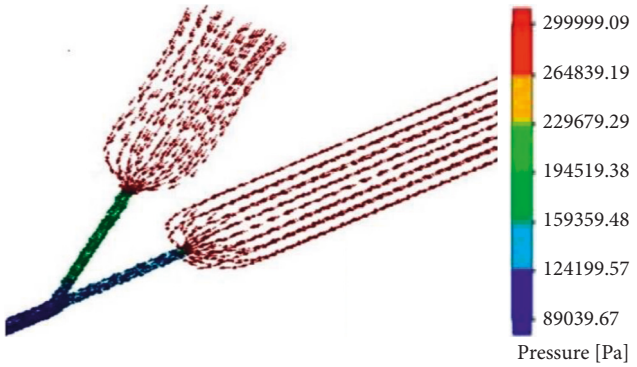

Figure 1: Isometric view of air at 300 kPa with the flow of fuel of 0.18 g/s. The values needed to evaluate the Wigg equation were taken from the tables predetermined by the software V 1.451423 (cSt). m_F: 0.20 (g/s); h: 0.040 (cm); σ: 22.3 (dynes/cm).

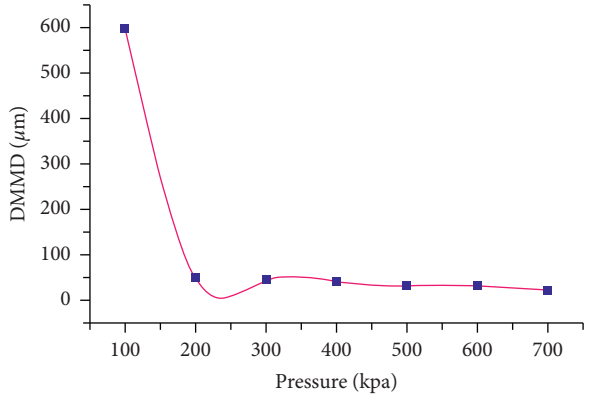

Figure 2: Dependence of the mass mean diameter and the stagnation pressure of the air.

3. Results and Discussion

The Y-type fuel injector in use was dimensioned in such a way that it operates at a power to operate at a thermal power of 10 kW and an ethanol mass flow rate of 0.20 g/s. The nozzle of the air and ethanol injector nozzle is 0.4 mm in diameter. The mixing chamber where the flows converge has a diameter of 0.40 mm and a length of 1.5 mm [6]. First of all, the injector was sketched out was first sketched with the measurements mentioned in the programme, and then the boundary conditions were on the thickness covering the fluid inlet were introduced [7]. For the ethanol, the boundary conditions were set to 0.20 g/s introduced for the ethanol lid, while for the air the stagnation pressures were varied in order to appreciate their influence on GLR, D_{MMD}, and velocity [8]. The diameter of a droplet can be measured using several different methods. As industrial methods for measuring spray droplet size, immersion sampling and laser analyzers are used. The values needed to evaluate the Wigg equation were taken from the default tables predetermined by the software [9]. An isometric view of air at 300 kPa with a flow of fuel of 0.18 g/s is shown in Figure 1.

Figure 2 shows the dependence of the mass mean diameter and the stagnation pressure of the air. In this study, it

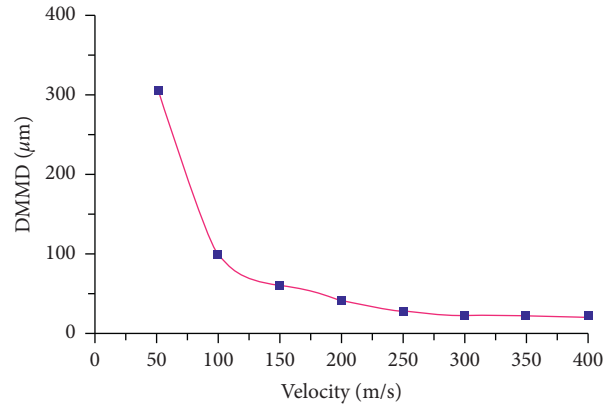

Figure 3: Dependence of the mass mean diameter and the speed of entry into the chamber.

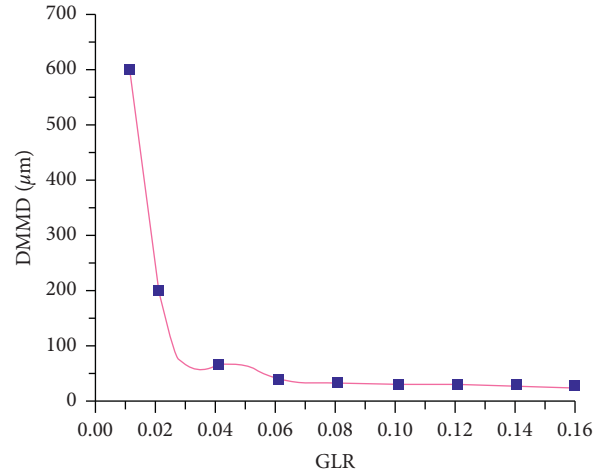

Figure 4: Dependence of the mass mean diameter and the GLR.

was found that for air stagnation pressures higher than 200 kPa, the droplet diameter is optimal and that for pressures approaching atmospheric conditions, such as pressures less than 180 kPa, the results are technically inefficient to achieve good atomisation.

Figure 3 shows the dependence of the mass mean diameter and the speed of entry into the chamber. The results show the velocity at the nozzle outlet of the nozzle exit achieves a better atomisation diameter when closer to the sonic regime obtaining values of around 15 μm.

Figure 4 shows the dependence of the mass mean diameter and the GLR. It was confirmed that values should be within the 0.10–0.20 GLR range. However, the range proposed in this study is much wider for ethanol with high atomisation performance in the range of 0.040–0.20 of GLR. [10].

4. Conclusions

The simulations carried out by the software Flow Simulation for a type Y injector with thermal power of 10 kW and a constant mass flow rate of 0.20 g/s obtained three important graphs for the characterisation of this type of injector using

ethanol as fuel. In this study, it was found that for air stagnation pressures higher than 200 kPa. the droplet diameter is optimal and for pressures approaching atmospheric conditions, such as pressures less than 180 kPa, the results are technically inefficient to achieve good atomisation. The results show the velocity at the nozzle outlet of the nozzle exit achieves a better atomisation diameter when closer to the sonic regime obtaining values of around 15 μm. In addition, it was confirmed that values should be within the 0.10–0.20 GLR range. However, the range proposed in this study is much wider for ethanol with high atomisation performance in the range of 0.040–0.20 of GLR.

Data Availability

The data used to support the findings of this study are included in the article.

Conflicts of Interest

The authors declare that they do not have any conflicts of interest regarding the publication of this paper.

References

[1] P. Belardini, C. Bertoli, C. Beatrice, A. D'Anna, and N. Del Giacomo, "Application of a reduced kinetic model for soot formation and burnout in three-dimensional diesel combustion computations," *Symposium (International) on Combustion*, vol. 26, no. 2, pp. 2517–2524, 1996.

[2] S. Donald, "Particulate carbon formation during combustion," 1981, https://www.springer.com/gp/book/9781475761399.

[3] R. M. Harrison and J. Yin, "Particulate matter in the atmosphere: which particle properties are important for its effects on health?" *Science of the Total Environment*, vol. 249, pp. 85–101, 2000.

[4] H. Hiroyasu, T. Kadota, and M. Arai, "Development and use of a spray combustion modeling to predict diesel engine efficiency and pollutant emissions: Part 1 combustion modeling," *Bulletin of JSME*, vol. 26, no. 214, pp. 569–575, 1983.

[5] S. Rojas, D. Mariños, M. Huaraz, and R. Chucuya, "CFD simulation on the influence of pressure and velocity, on the mean mass diameter of the drop on the Y type injectors," *SCIÉNDO*, vol. 19, no. 2, pp. 67–71, 2016.

[6] K. Kalaimurugan, S. Karthikeyan, M. Periyasamy, G. Mahendran, and T. Dharmaprabhakaran, "Experimental studies on the influence of copper oxide nanoparticle on biodiesel-diesel fuel blend in CI engine," *Energy Sources, Part A: Recovery, Utilization, and Environmental Effects*, 2019.

[7] C. S. Lee, S. W. Park, and S. Kwon, "An experimental study on the atomization and combustion characteristics of biodiesel-blended fuels," *Energy & Fuels*, vol. 19, pp. 2201–2208, 2015.

[8] R. Surakasi, Y. S. Ratnakar, V. V. Prasanna Kumar, and M. Sairam, "Performance evaluation and emission characteristics of organic sunflower oil biodiesel using additives," 2021, http://thedesignengineering.com/index.php/DE/article/view/5439.

[9] R. P. Lindstedt and S. A. Louloudi, "Joint-scalar transported PDF modeling of soot formation and oxidation," *Proceedings of the Combustion Institute*, vol. 30, no. 1, pp. 775–783, 2005.

[10] R. Surakasi, M. Y. Khan, A. S. Sener et al., "Analysis of environmental emission neat diesel-biodiesel-algae oil-nanometal additives in compression ignition engines," *Journal of Nanomaterials*, vol. 2022, Article ID 3660233, 7 pages, 2022.

Hindawi
Journal of Engineering
Volume 2022, Article ID 3473356, 6 pages
https://doi.org/10.1155/2022/3473356

Research Article

Optimization of the Process of Metal NanoCalcium Oxide Based Biodiesel Production through Simulation Using SuperPro Designer

Raviteja Surakasi,[1] **Balakrishna Gogulamudi**,[2] **Alla Naveen Krishna**,[3] **Raja Ambethkar M**,[4] **Pravin P. Patil**,[5] **and Pradeep Jayappa**[6]

[1]*Department of Mechanical Engineering, Lendi Institute of Engineering and Technology, Jonnada, Vizianagaram, Andhra Pradesh, India*
[2]*Department of Mechanical Engineering, PVP Siddhartha Institute of Technology, Kanuru, Vijayawada, Andhra Pradesh, India*
[3]*Department of Mechanical Engineering, Institute of Aeronautical Engineering, Hyderabad, Telangana, India*
[4]*Department of Engineering English, College of Engineering, Koneru Lakshmaiah Education Foundation, Vaddeswaram, Andhra Pradesh, India*
[5]*Mechanical Engineering Department, Graphic Era Deemed to Be University, Dehradun, Uttarakhand, India*
[6]*Department of Chemical Engineering, College of Engineering and Technology, Bulehora University, Oromia, Ethiopia*

Correspondence should be addressed to Pradeep Jayappa; pradeep.jayappa@gmail.com

Received 28 May 2022; Revised 20 June 2022; Accepted 23 June 2022; Published 7 July 2022

Academic Editor: Karthikeyan Sathasivam

This study evaluates improvements made to a biodiesel production process from Chlorella sp. micro algae in a locomotive pilot plant using simulation. Energy and the main variables of the operation such as temperature, reaction time, alcohol molar concentration, vegetable oil, and use of homogeneous and heterogeneous catalysts and their concentration, mixing intensity, and moisture control were collected from operational data, and mass balances were tested in the SuperPro Designer retail package v.9.5. The result was an increase in the efficiency of the process of obtaining company biodiesel from 86% to 92% by volume, the same that were scaled taking into account the species' production locality, and the results obtained showed that 26% was met by obtaining 10 MM (millions) of liters of biodiesel from the scaled plant.

1. Introduction

In recent years, the world's population growth has prompted a search for alternatives to meet the rising demand for energy consumption. Even now, fossil fuels have been the primary source of energy in most daily processes, and they have been directly responsible for environmental damage, such as climate change. The recent research has shifted its focus away from adaptation to circumstances and strategies for mitigating the problems that society faces due to environmental factors, such as the United Nations Conference on Climate Change. Around 78% of energy comes from fossil fuels, while the remaining 24% comes from various sources. Biodiesel is promoted as a viable alternative to fossil fuels and is touted as a valuable energy source because it can be made from agricultural, forestry, or municipal waste. Animal, vegetable, or recycled fats can be converted into biodiesel via a transesterification process, which has better environmental characteristics than petroleum-based diesel. Vegetable oils are used to make 84% of biodiesel, and using various raw materials such as pinion, biomass, cooking oil, and animal fat is expected to decrease. If sustainability criteria are met, biodiesel should replace fossil fuels shortly. However, no appropriate technological development has occurred. The progress is dependent on various investor resolutions and research spending to meet regional goals. The market price of biodiesel today cannot compete with crude oil prices. Still, it is expected that the price of

petroleum derivatives, particularly fuels, will rise by 8% from the date, resulting in a 52% increase in biodiesel demand for automotive consumption, creating job opportunities and growing the local economy. Biodiesel stimulates agricultural activity which also provides environmental benefits such as reduced greenhouse gas emissions such as CO, CO_2, and NOx, and because it contains almost no sulfur, no SO2 is produced. However, using fuels with a composition of 96% conventional diesel and 6% biodiesel results in a reduction in greenhouse gas emissions [1].

The transesterification reaction of oils or fats (which is a reaction between your triglycerides) and methanol, which produces glycerin and methyl esters, can be used to make biodiesel. In the presence of a catalyst, triglycerides are found in Chlorella sp. micro algae oil reacts with low molecular weight alcohol (methanol, ethanol, etc.) to form glycerin, a mixture of fatty esters. The catalyst's performance and the control of optimal reaction conditions are essential considerations in reaction transesterification. The reaction represented in Figure 1 is a reversible reaction in which the ROH serves as a catalyst. The strings of fatty acids associated with the oil or fat used in the reaction, usually acid palmitic, stearic, oleic, and linoleic, are represented by R', R', and R''. The transesterification of fatty acids SuperPro Designer was used to simulate Chlorella sp. micro algae Biodiesel. The proportion, chain length of carbons, and degree of unsaturation of biodiesel are all determined by fatty acid methyl esters. Viscosity kinematics, density, cetane number, iodine number, acid number, and enthalpy of combustion are some of the physicochemical characteristics used to determine biodiesel quality, as defined by ASTM D6751 in the United States and EN 14214 in Europe. Biodiesel from oils rich in fatty acids unsaturated like oleic and linoleic provides characteristics suitable for internal combustion engines' correct performance since their density and viscosity are similar to diesel. It has been discovered that the presence of monounsaturated fatty acid esters improves biodiesel ignition quality and engine flow. The genus Chlorella sp. micro algae belongs to the Euphorbiaceous family, and Latin America is a hotbed of diversity and endemism, with roughly 22% of its species found there. The Chlorella sp. micro algae species, also known as pinion or piloncillo, have toxic and nontoxic varieties. Due to its oil content of 32% to 42% and the composition chemistry, which is close to 22% saturated fatty acids and 78% unsaturated fatty acids, several studies characterize it as a species with a large capacity for the production of biodiesel [2]. Based on biomass yield, lipid content, as well as quality of lipids, Chlorella Vulgaris is considered an ideal candidate for biodiesel production. For mass cultivation of microalgae on low-cost substrates, there is a need to develop more work so that the price of biomass output can be decreased.

2. Materials and Methods

The current process of producing biodiesel from Chlorella sp. micro algae oil. The plant has an 84% production capacity and a daily output of 4 L. Table 1 shows the detail of the plant stream flows pilot used for the base simulation [3]. Figure 2

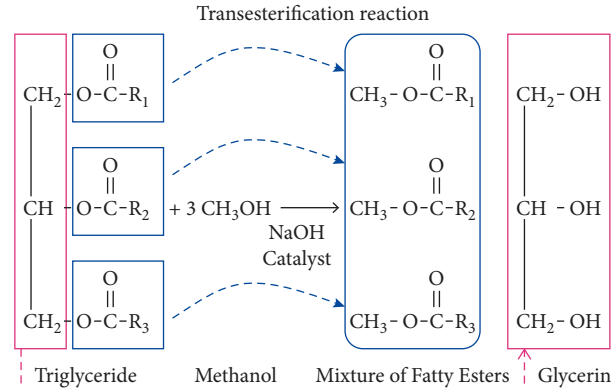

Figure 1: Transesterification reaction of Chlorella sp. micro algae Biodiesel.

shows the photo view of Chlorella sp. micro algae. The pilot plant and simulation consist of four processes: a reactor R-101, two centrifuges DC-101 and DC 102, and a mixer of M-101, which are the same as those in the biodiesel production process shown in Figure 3 and are briefly explained below. The catalysis stream, which contains a 74% solution of methanol with 26% sodium hydroxide, forming the compound sodium methoxide (NaOCH3), is mixed with the methanol stream, forming the stream C-101, which feeds the reactor R-101 through the cap, while Chlorella sp. micro algae oil feeds the reactor through the middle part. Methanol reacts with Chlorella sp. micro algae oil in the transesterification reaction is shown in Figure 4, yielding stream C-102, which contains biodiesel, glycerol, and traces of reactants. The reactor has a one-hour residence time, resulting in a conversion rate of 83 to 86%. The C-102 stream is passed through the DC-101 centrifuge, which separates fats and oils from glycerol to produce as much as crude biodiesel (C-103) as possible (C-104). To achieve biodiesel separation from glycerol, the centrifugation processes used properties suggested by the SuperPro Designer software V9.5 for this type of equipment, such as the solvent type and separator particle size, while only changing the percentages in the mass balance [4]. The crude biodiesel stream C-103 is washed with acidified water (C-105) with a pH of 4.5 in the mixer M-101, with HCl in a 1 percent w/w ratio to oil neutralize catalysis to prevent soap formation. After that, the mixture (C-106) is sent to the second centrifuge (DC 102) to separate the aqueous phase and extract the biodiesel and glycerol residues [5]. Temperature, reaction time, alcohol: oil molar ratio plant, type of alcohol, humidity, and catalyst concentration are all factors that can influence the transesterification process. The biodiesel stream product should not contain more than 0.05% water by weight. High water content can slow down the reaction rate because water reacts with catalysts to form soaps [6]. The stoichiometric ratio for transesterification is 3 : 1 alcohol: oil, but an excess of methanol up to a 6 : 1 ratio is usually chosen for higher conversion. However, a higher alcohol ratio at 6 : 1 may affect glycerine separation by an increased solubility, which causes the reaction to revert to the left, reducing the esters' yield. [7].

Table 1: Details of plant stream flow pilot used for the base simulation.

Current	Components flow	(kg/day)
	Reactor 1/R-101	
C-101	Methanol catalysis	0.43
Chlorella sp. microalgae oil	Chlorella sp. microalgae oil	4.00
	Centrifuge 2/DC-102	
	Biodiesel	3,8000
	Glycerol	0.4038
C-102	Chlorella sp. microalgae oil	0.1171
	Sodium methoxide	0.0125
	Water	0.0160
	Biodiesel	3,8100
C-103	Chlorella sp. microalgae oil	0.1116
	Sodium methoxide	0.0125
	Water	0.0160
C-104	Glycerol	0.4038
	Mixer/R-103	
C-105	HCl- water	0.1570
C-106	Biodiesel	3.8306
	Glycerol 0.0403	0.0403
	HCl	0.0152
	Chlorella sp. microalgae oil	0.1171
	Methanol	0.0055
	Sodium methoxide	0.0031
	Sodium chloride	0.0101
	Water	0.0160
	Centrifuge 2/DC-104	
Biodiesel	Biodiesel	3,8508
C-107	Glycerol	0.0400

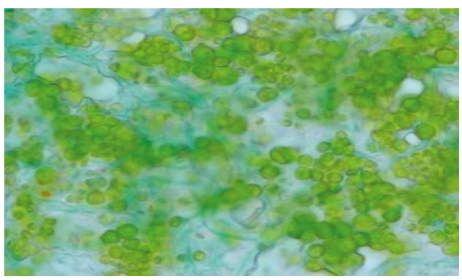

Figure 2: The photo view of Chlorella sp. micro algae.

3. Results

SuperPro Designer Software v.9.5 data was used to generate the various physical properties of compounds used in this simulation. The Production of biological products is analyzed and assessed by using the SuperPro Designer. This analysis looks at the production of citric acid, an organic acid used heavily in the beverage industry. The first commercial product of modern biotechnology is recombinant human insulin, which is manufactured by bacteria. The following operating conditions are recommended in biodiesel pilot plants: a continuously stirred reactor with a reaction temperature of 60°C and a pressure of 1 atm, with a residence time of 60 minutes. Because of the oil of Chlorella sp. Micro Algae oil from Ecuador contains only 1.27% free fatty acids,

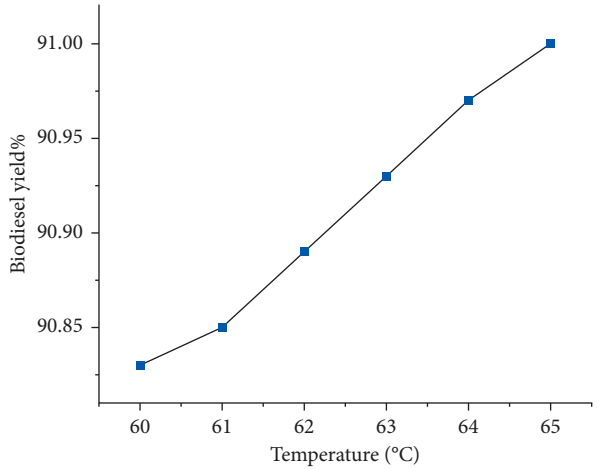

Figure 3: Biodiesel yield as a function of temperature variation.

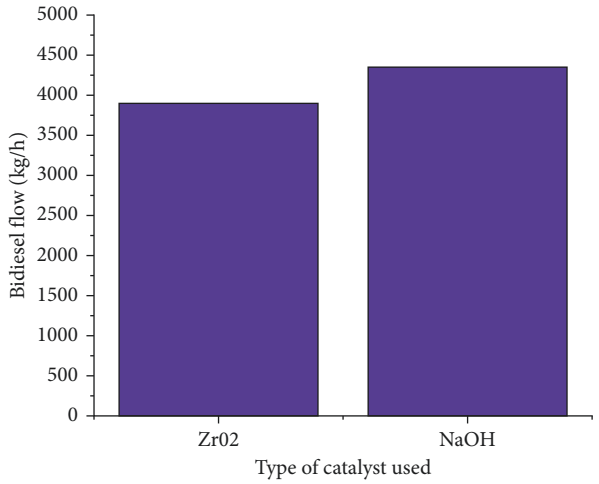

Figure 4: Biodiesel production concerning the type of catalyst used for the transesterification.

the transesterification stage. Because of its advantages, such as cost and reaction speed, NaOH was used as a catalyst; the catalyst concentration was 1%, and the alcohol: oil molar ratio was 3 : 1. The results obtained in the biodiesel pilot plant of the locomotive company studied before the realization of the simulation were 84%, based only on the volume of the product at the end of the process, which represents approximately 2.5 kg/day of biodiesel [8]. When analyzing the different operating variables mentioned in the methodology and ensuring maximum conversions, a time of 90 minutes residence in the reactor, time with the that is being worked on in some plants to obtain biodiesel in India, yielding results of 3.9 kg of biodiesel, corresponding to 92% conversion to the previous process in the base simulation, which was 86% obtaining results of 3.8 kg of biodiesel, corresponding to 92% conversion to the previous process in the base [9].

3.1. Proposal. Deescalation of 10 MM of *L*/year When analyzing the current situation in Ecuador and before the

Table 2: Identified variables and specific operation values.

Variables	Values bibliographic of operation
Reaction temperature	60°C
Molar alcohol ratio : vegetable oil	3 : 1
Alcohol type	Methanol
Catalyst type	NaOH
Concentration of catalyst	1% w/w
Reaction time	90 min
Mixing intensity	450 rpm
Humidity	0.05%

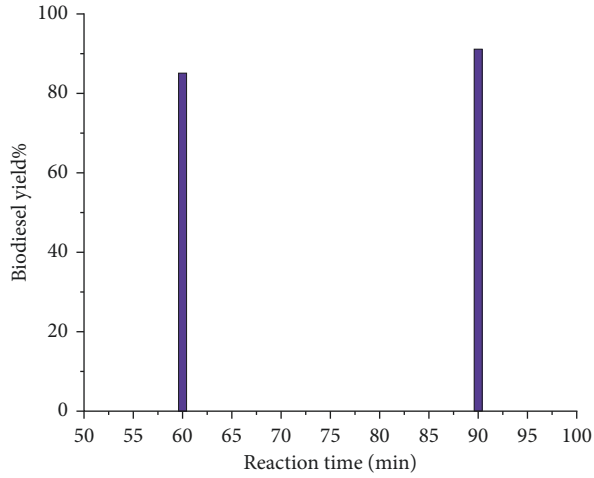

Figure 5: Biodiesel yield as a function of reaction time.

requirement of the change of the energy matrix, arranged to design by simulation, of a plant of greater capacity. For the simulation of the new plant, the information collected from various studies on the variables involved in the biodiesel process and the inclusion of a process for treating the glycerin produced using the software, as shown in Table 2. The proposed scaling of the biodiesel production process is depicted in Figure 3. The proposal's principles are based on the simulation used in the company's biodiesel procurement process [10]. Figure 5 describes the two stages of the simulation: reaction and two additional steps for glycerin purification. They are described in the following paragraphs.

The proposed scaling of the biodiesel production process is depicted in Figure 4. The principles of the proposal are based on the simulation used in the company's biodiesel acquisition process. Figure 5 describes the two stages of the simulation: reaction and two additional steps for glycerin purification. They are described in the following paragraphs: Although transesterification of Chlorella sp. micro algae can occur at temperatures as low as 25°C, it is recommended that temperatures be kept between 60 and 65°C, due to the alcohol. Oil concentration ratio of 3 : 1. Table 3 shows that the water content in the steam stream is 98.5%, while the water content in the stream by the part lower than biodiesel is 98.5%, indicating that water and biodiesel have been separated [11]. The streams from the three centrifuges enter the

Table 3: Flash distiller/V-101 results.

	Components	kg/h	% Time
Vapour	Biodiesel	0.0019	0.0022
	Glycerol	0.0963	0.1092
	Chlorella sp. microalgae oil	0.0963	0.1092
	Methanol	0.8014	0.9078
	NaOCH3	0.1573	0.1782
	Water	87.1017	98.6934
Biodiesel	Biodiesel	4269.958	98,5342
	Glycerol	40.4833	0,9342
	Chlorella sp. microalgae oil	6.0642	0,1399
	Methanol	0.3895	0,0090
	NaOCH3	0.1874	0,0043
	Water	15.4422	0,0356

Table 4: Flash/V-101 distiller result.

		kg/hr	Time
Vapour	Biodiesel	0.0059	0.0064
	Glycerol	0.1058	0.1141
	Chlorella sp. microalgae oil	0.1472	0.1588
	Methanol	1.5813	1.7059
	Oxide zirconium	0.2798	0.3018
	Water	90.5761	97.7130
Biodiesel	Biodiesel	3742.099	98,0683
	Glycerol	45.1496	1,1832
	Chlorella sp. microalgae oil	7.1045	0,1862
	Methanol	0.8423	0,0221
	Oxide zirconium	10.1584	0,2662
	Water	10.4569	0,2740

mixer M-201 to be acidified with HCl 38% to separate the soaps and neutralize the NaOH residue contained in them in the glycerin purification process. Although increasing the temperature to 60°C improves performance and reduces reaction time, the operating variables used in the scaling proposal from Table 3 should be considered. It is recommended that the temperature not exceed 64.7°C, the boiling point of methanol, because it will vaporize, forming bubbles that will limit the reaction in the alcohol/oil/biodiesel phases. To achieve the goal of 10 MM L/year, the operating time of the locomotive pilot plant is used as a guide, which is 9-hours per day for 240 days. Consider the various inputs to the process over a year, which equals 10279 tons/year, and the output at the end of the process, which equals 9354 tons/year, for a yield of 91% w/w. The prices of the materials were calculated using a bibliography and marketing studies conducted in Ecuador [12].

The type of catalyst used to make biodiesel is one of the modified variables. The following are the results of a scaling plant simulation using a heterogeneous catalyst such as oxide zirconium (ZrO_2) and the values of the variables in Table 3: The rate of raw material input into the process is 4759 kg per hour [13]. In comparison, the process output is 3909 kg/h, resulting from the steam currents and biodiesel from Table 4, with an 83% w/w conversion using ZrO_2. These figures are supported by experimental results using ZrO_2 as a catalyst, in which yields of 87to 90% conversion were obtained, with a conversion of 92%, or 4334 kg/*h*, at

the scaling plant in the Flash V-101 still using NaOH as a catalyst, as shown in Figure 3. Homogeneous catalysts, such as NaOH outperform heterogeneous catalysts in terms of price and performance. As shown in Figure 5, maintaining a 60°C range is advantageous to reaction rate, and studies conducted in India suggest that the reaction temperature is directly related to the alcohol: oil molar ratio and reaction time variables. Although it is specified that excess alcohol can be used up to a 6 : 1 concentration to ensure high conversions, this specification prevents the simulation from being developed in the SuperPro Designer v.9.5 programs because of the transesterification reaction in its database is designed to operate with alcohol: oil. When working on the scaled plant simulation with a 60-minute residence time in reactors, a product output of 4045 was obtained, corresponding to an 86% conversion; however, when using a residence time of 90 minutes in both reactors, a parameter with which we work in different plants in India, a value of 4759 kg was obtained. There was no evidence of a performance improvement, which would have resulted in a cost increase [14]. Following the acquisition of biodiesel, it must be characterized to ensure that it meets international standards such as ASTM D6751 in the United States. Biodiesel must be characterized after it is obtained to ensure that it meets international standards such as ASTM D6751 in the United States and EN 14214 in Europe. Biodiesel must be characterized after it is obtained to ensure that it meets the requirements of international standards [15, 16].

4. Conclusions

Using the oil of Chlorella sp. micro algae as a raw material, the opportunities for improvement found with the implementation of production processes allowed determining appropriate raw material quantities to achieve a 92% efficiency. The proposed design, with the values of the variables of 65°C temperature, alcohol methanol molar ratio: 3 : 1 oil, 1% catalyst concentration (NaOH) w/w, reaction time 90 min, and an intensity of 450 rpm mixing, resulted in a production of 10248 tons of lit biodiesel obtained from oil of Chlorella sp. micro algae. According to the economic analysis, the project results are profitable because of the internal rate of return (7.42%) is higher than that of the interest rate paid by a national bank (5%). Similarly, it was demonstrated that achieving a positive NPV should take at least 5 years, representing the investment's payback time, when working at a 9-hour per-day rate for 242 Table days.

Data Availability

The data used to support the findings of this study are included in the article.

Conflicts of Interest

The authors declare that they have no conflicts of interest regarding the publication of this paper.

References

[1] G. Vaidya, P. P. Patil, A. S. Sener et al., "Chlorella prototheocoides algae oil and its mixes with lower and higher alcohols and Al2O3 metal nanoadditives for reduction of pollution in a CI engine," *Journal of Nanomaterials*, vol. 2022, pp. 1–6, Article ID 9658212, 2022.

[2] M. E. M. Soudagar, N. N. Nik-Ghazali, M. Abul Kalam et al., "The effect of nano-additives in diesel-biodiesel fuel blends: a comprehensive review on stability, engine performance and emission characteristics," *Energy Conversion and Management*, vol. 178, pp. 146–177, 2018.

[3] M. J. Haas, A. J. McAloon, W. C. Yee, and T. A. Foglia, "A process model to estimate biodiesel production costs," *Bioresource Technology*, vol. 97, pp. 671–678, 2006.

[4] X. Zhao, G. Yao, and W. E. Tyner, "Quantifying breakeven price distributions in stochastictechno-economic analysis techno-economic analysis," *Applied Energy*, vol. 183, pp. 318–326, 2016.

[5] M. R. Osaki and P. Seleghim, "Bioethanol and power from integrated second generation biomass: a monte carlo simulation," *Energy Conversion and Management*, vol. 141, pp. 274–284, 2017.

[6] C. A. Salman, E. Thorin, and J. Yan, "Uncertainty and Influence of input parameters and assumptions on the design and analysis of thermochemical waste conversion processes: astochastic approach," *Energy Conversion and Management*, vol. 214, Article ID 112867, 2020.

[7] R. Surakasi, Y. S. Ratnakar, V. V. Prasanna Kumar, and M. Sairam, "Performance evaluation and emission characteristics of organic sunflower oil biodiesel using additives," *Design Engineering*, vol. 2012, pp. 4968–4983, 2021.

[8] R. Ganesan, S. Manigandan, M. S. Samuel et al., "A review on prospective production of biofuel from microalgae," *Biotechnology Reports*, vol. 27, Article ID e00509, 2020.

[9] J. Arunprasad, A. N. Krishna, D. Radha, M. Singh, R. Surakasi, and T. D. Gidebo, "Nanometal-based magnesium oxide nanoparticle with *C. vulgaris* algae biodiesel in diesel engine," *Journal of Nanomaterials*, vol. 2022, pp. 1–9, Article ID 1688505, 2022.

[10] O. Ogunkunle and N. A. Ahmed, "Response surface analysis for optimisation of reaction parameters of biodiesel production from alcoholysis of Parinari polyandra seed oil," *International Journal of Sustainable Energy*, vol. 38, no. 7, pp. 630–648, 2019b.

[11] S. Bari, S. N. Hossain, and I. Saad, "A review on improving airflow characteristics inside the combustion chamber of CI engines to improve the performance with higher viscous biofuels," *Fuel*, vol. 264, Article ID 116769, 2020.

[12] R. Surakasi, M. Y. Khan, A. S. Sener et al., "Analysis of environmental emission neat diesel-biodiesel-algae oil-nanometal additives in compression ignition engines," *Journal of Nanomaterials*, vol. 2022, pp. 1–7, Article ID 3660233, 2022.

[13] M. A. Fayad and H. A. Dhahad, "Effects of adding aluminum oxide nanoparticles to butanol-diesel blends on performance, particulate matter, and emission characteristics of diesel engine," *Fuel*, vol. 286, Article ID 119363, 2021.

[14] M. Subramaniam, J. M. Solomon, V. Nadanakumar, S. Anaimuthu, and R. Sathyamurthy, "Experimental investigation on performance, combustion and emission characteristics of DI diesel engine using algae as a biodiesel," *Energy Reports*, vol. 6, pp. 1382–1392, 2020.

[15] R. Surakasi and V. V. Prasanna Kumar, "Performance and emission characteristics of sunflower oil bio diesel on four stroke diesel engine," *International Journal of Advanced Research in Engineering and Technology*, vol. 12, pp. 204–216, 2021.

[16] R. Surakasi, C. H. Polayya, D. Appanna, V. V. Prasanna Kumar, and B. Ranjan, "Combustion characteristics of waste cooking oil bio diesel on four stroke diesel engine using additives," *Turkish Journal of Computer and Mathematics Education (TURCOMAT)*, vol. 12, no. 13, 2021.

Hindawi
Journal of Engineering
Volume 2022, Article ID 7441659, 7 pages
https://doi.org/10.1155/2022/7441659

Research Article

Performance and Emission Analysis of Common Rail Diesel Engine with Microalgae Biodiesel

Yenda Srinivasa Rao [1] **and Tsegaye Getachew Alenka** [2]

[1]*Department of Mechanical Engineering, Swamy Vivekananda Engineering College, Bobbili, Andhra Pradesh, India*
[2]*Department of Mechanical Engineering, Wolaita Sodo University, Sodo, Ethiopia*

Correspondence should be addressed to Tsegaye Getachew Alenka; tsegaye.getachew@wsu.edu.et

Received 20 May 2022; Revised 7 June 2022; Accepted 11 June 2022; Published 4 July 2022

Academic Editor: Karthikeyan Sathasivam

Modern common rail diesel engines are normally optimized with commercial diesel. As a result, the engine control unit's calibration is established to achieve the best compromise between performances and exhaust pollutants. Biodiesel has a faster combustion rate and higher combustion chamber temperature than commercial diesel, which necessitates the injection of higher fuel volumes to compensate for the lower calorific value of biodiesel compared to regular diesel. This study showed that by adjusting the mapping of the engine control unit according to the fuel utilised, it is possible to improve the emissions and performance of a common rail diesel engine running on pure *Botryococcus braunii* algae oil biodiesel or a blend of biodiesel and commercial diesel.

1. Introduction

While each country bears varying degrees of responsibility for the emission of climate-changing gases into the atmosphere [1]. It is also true that regardless of their culpability, every country today faces the severe problem of climate change's repercussions. This planetary nature of the problem implies that universally approved international policies for gradual reductions in emissions into the atmosphere, as well as common support in anticipation of the large costs required to protect entire populations from the effects of climate change, are required [2]. The necessity to invest in alternative energy such as biofuels derived from crops such as sunflower, soybean, and rapeseed is thus emphasized, especially given the role they may play in achieving the reduction of greenhouse gas emissions. Agriculture's contribution helps us achieve the Kyoto Protocol's goals while lowering pollution levels [3]. A million tonnes of biodiesel produced from domestic crops reduces hydrocarbon and polycyclic aromatic emissions by 80% and particulate matter and fine dust by 50%, respectively. The IPCC identified CO_2 as one of the gases responsible for the greenhouse effect and human activity as one of the reasons in its first report in 1990. That human activity is behind the acceleration of the heating process and that only by drastically reducing greenhouse gas emissions in the atmosphere will it be possible to avoid exceeding the critical, dangerous thresholds even for the maintenance of life on Earth has evolved [4]. The recent oil crisis, as well as public interest in environmental issues, has prompted further research into all renewable energy options. More and more sustainable energy sources, including biomass, are gaining popularity in the community. The latest official document presented by the EPA is intended to provide information to interested parties who want to evaluate the possibility of using biodiesel as a substitute for commercial automotive diesel [5]. Analysis of data available from the EPA on regulated engine emissions heavy duty can be summarized, which shows the percentage of biodiesel mixed with diesel and the variation of emissions NOx, PM, CO, and HC compared to commercial diesel. The reported results are in the most general form possible and summarize a fact known in the literature. As the percentage of biodiesel in a blend with the diesel fuel, HC, CO, and PM emissions decrease while NOx increases to

a maximum of 10% for pure biodiesel [6]. The increase in NOx emissions with increasing concentration of biodiesel could be a deterrent to the use of biodiesel. The analysis of the averages of the results of the experimental tests available led the EPA to affirm that measurements on blends with 20% of biodiesel show a decrease in NOx emissions. Further analysis by the EPA aimed at understanding the phenomenon in which many aspects have been taken into account such as the origin of oil of biodiesel and the type of plant and test condition. The analysis of this pollutant was conducted also according to the type of biodiesel used. This research does not deal with issues such as air quality, production, or distribution costs of biodiesel. It is mainly focused on the environmental impact of biodiesel as a fuel for land traction. All available public data on biodiesel were collected first, and then an in-depth analysis to correlate all the data was performed [7]. The results were presented on the influence of biodiesel on regulated emissions.

2. Description of the MultiJet Injection System

The engine on which the testing activity was carried out is the Simpson XRDF model. It is a modern second-hand common rail direct injection diesel generation equipped with a 1910 cm^3 MultiJet injection system of displacement double overhead camshaft distribution and four valves per cylinder. The engine is equipped with a MultiJet injection system. Multiple injections represent a strong technological evolution of the now well-known common rail system [8]. The research center has developed a management system for the combustion process through the use of injections multiple. This MultiJet system allows a strong reduction of emissions of NOx and particulates without a significant penalty in terms of costs. The raising of the maximum diesel pressure from 1600–1700 bar, for the improvement of the flue gas post-treatment systems. The first-generation common rail systems have a small injection pilot which is implemented a few milliseconds before the main injection. The concept behind multiple injections is to divide the injection main into a sequence of three close injections such as Pre-Main-After [9]. The preinjection allows controlling the combustion speed of the phase premixed, further reducing the combustion noise compared to the common rail of first-generation. The preinjection behaves in a similar way to the pilot injection while guaranteeing containment of particulate matter (soot) and CO. The engine specification shown in Tables 1 and 2 shows the uncertainty analysis of all the parameters. Figure 1 shows the engine setup with a common rail injection system.

Table 1: Engine specification.

Engine	Diesel cycle, 4 strokes, 4 cylinders, bore 92 mm
Stroke	90.4 mm
Total displacement	1910 cm^3
Relationship of compression	17.5 : 1
Maximum power	150 hp (110 kW) at 4000 rpm
Maximum torque	305 Nm at 2000 rpm
Distribution	4 valves per cylinder
Diet	Common rail MultiJet direct injection
Alternator	85 A, 14 V
Battery	60 Ah, 12 V

Table 2: Uncertainty error analysis.

Parameter	Resolution	Accuracy	Range
CO	1 ppm	±20 ppm (for <400 ppm CO)	0–10000 ppm
Nitrogen dioxide (NO_x)	1 ppm	±5 ppm (for <100 ppm NO_2)	0–1000 ppm
Operating temperature −10 to 45°C			
Warm-up time 3 min			
Response time T90 30 sec			
Operating humidity 5–95% noncondensing			

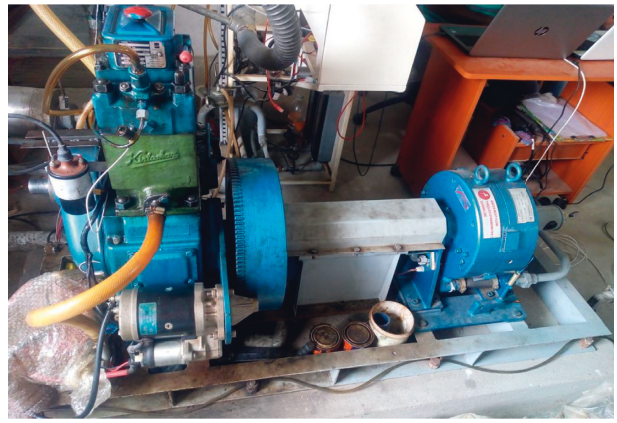

Figure 1: Engine setup with common rail injection system.

3. Characteristics of Algae Biodiesel

Biodiesel is a renewable fuel that may be made from a variety of sources, including a wide range of algae oils [10]. The transesterification method provides for the production of biodiesel appropriate for diesel engines. Biodiesel is typically made from a blend of several transesterified oils, both to account for market availability and to produce a final product that meets the requirements set forth by the numerous directives in place today. Algae oils differ greatly in their properties, partly according to the quantity of fatty acids they contain. It is noted that a considerable content of unsaturated fatty acids improves combustion at low temperatures and that the number of cetanes is strictly dependent on the distribution of fatty acids. Algae oils have various proportions of unsaturated fatty acids, which are blended during biodiesel manufacturing [11]. Table 3 shows the characteristics of biodiesel in this research work. Figure 2 shows a photo view of *Botryococcus braunii* algae.

4. Calibration Optimizations

The engine was run on 100% pure biodiesel (B100) and a mixture of 50% biodiesel and 50% commercial diesel during the tests (B50) and this same volume procedure was followed by B20. The results were compared to experiments using commercial diesel oil and comparing emissions and performance

Table 3: Characteristics of biodiesel.

Properties	Diesel	AME	B50	B20
Cetane number	48	52	51	51
C/H/O (molar ratio)	16 : 30 : 0	19 : 34 : 2	20 : 33 : 1	21 : 33 : 2
Density, g/cm^3 (15 C)	0.83	0.89	0.90	0.91
Kinematic viscosity, cSt (37.8 C)	3.3	4.5	4.8	4.9
Net calorific value kJ/kg	43000	36000	42000	44000
Clod point (C)	>4	>4	>4	>4
Carbon content (wt %)	86.5	77.4	74.2	72.1
Hydrogen content H (wt %)	13.4	12	12.2	12.3
Oxygen content O (wt %)	—	10.5	11.1	11.2
Sulfur content S (wt %)	0.05	<0.01	<0.01	<0.01
Stoichiometric ratio A/F	14.5	12.6	12.4	12.5
Iodine number, g I2/100 g	—	118	119	119
Distillation curve				
10% EV	181	332	352	354
50% EV	255	340	345	347
90% EV	337	350	354	355
F.B.P.	372	353	359	360
Carbon residue (wt %)	0.01	0.05	0.06	0.06
Biodegradability	No	Yes	Yes	Yes

Figure 2: A photo view of *Botryococcus braunii* algae.

[12]. The research's objective was to optimize engine control parameters based on the fuel used, to achieve the optimal balance between engine performance and emissions levels once the fuel was known. For this, software was utilised that allows the engine settings regulated by the control unit motor to be changed in real-time and during engine operation. The performance and emissions of the engine fueled with biodiesel and the biodiesel-diesel blend were measured, and mapping was sought that would allow the engine fueled with biodiesel and the biodiesel-diesel blend to run like when it was driven by diesel.

5. Result and Discussion

5.1. Performance. The performance depicts the maximum performance of the biodiesel-powered engine. It is focused on finding engine characteristics that permitted a biodiesel-fueled engine to generate the same torque and maximum power as a diesel engine. Polluting pollutants from engine exhaust were not taken into consideration during this period

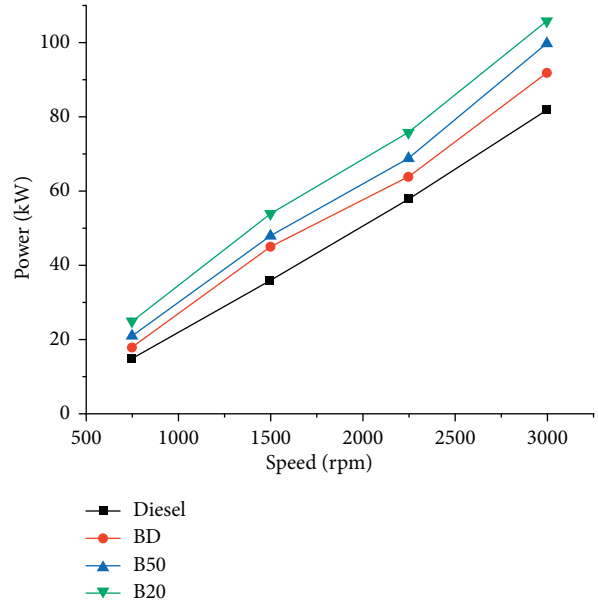

Figure 3: Power vs speed.

[13]. Figures 3 and 4 show the torque and the maximum power relative to three different blends. The torque required by the control system, which governs the amount of fuel injected per cycle, injection timing, and boosts pressure, was the control unit parameter on which the major action was performed. Due to the various characteristics of the fuel used, the performance of the engine when fueled by diesel is significantly lower [14]. The mass of fuel injected and the injection advance fails to account for biodiesel's increased calorific value and heat release rate, which differs from diesel fuel. To achieve the same performance as a diesel engine, it was essential to increase the mass of fuel injected per cycle.

5.2. Pollutant Emissions. In particular, the improvements that can be obtained for CO and NOx emissions will be analyzed by modifying some engine parameters. In this

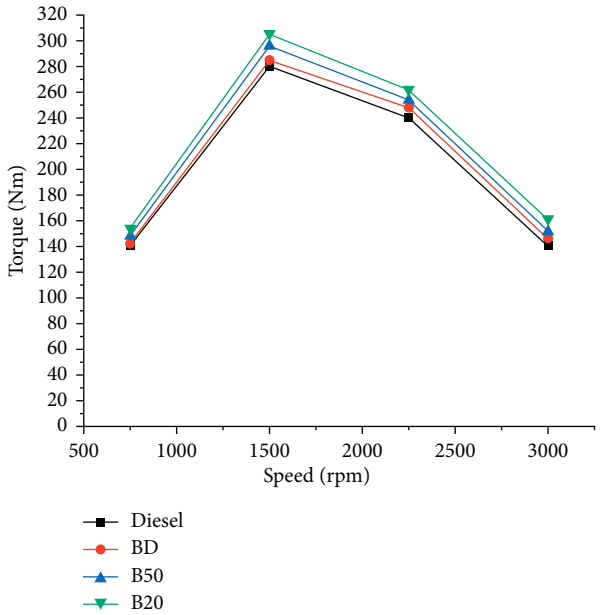

Figure 4: Torque vs speed.

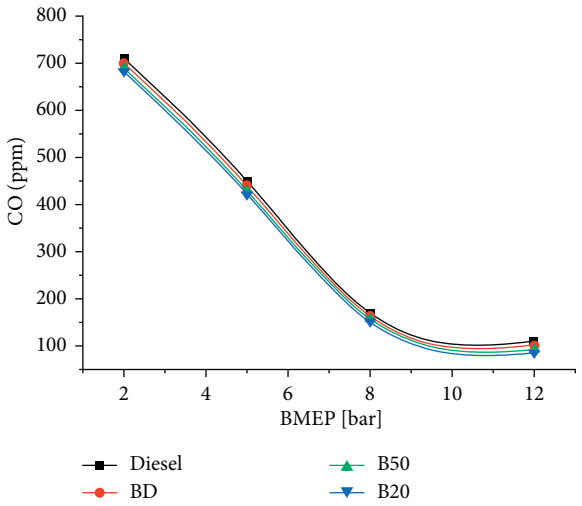

Figure 5: CO emission with bmep @ 1500 rpm.

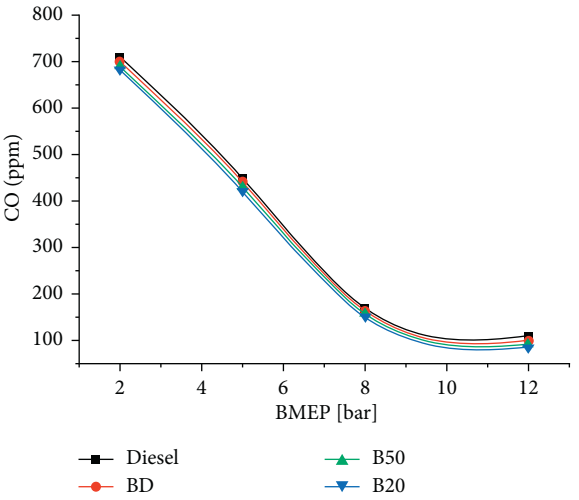

Figure 6: CO emission with bmep @ 2000 rpm.

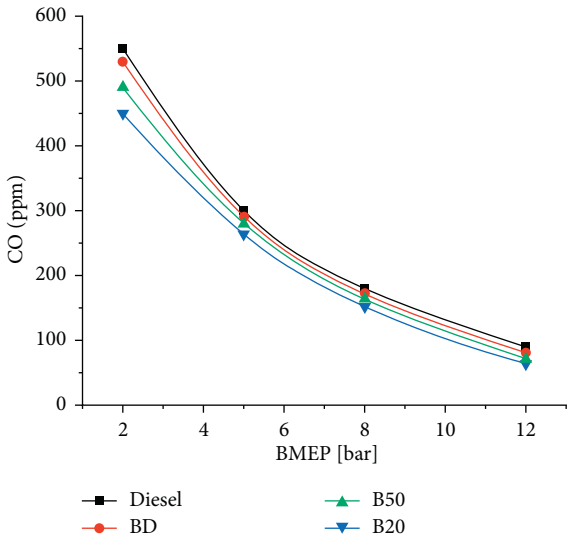

Figure 7: CO emission with bmep @ 3000 rpm.

research, the trends of carbon monoxide emissions will be shown (CO) and nitrogen oxides (NOx) for two different fuels [15]. The results will be compared with the emissions measured by fueling the engine with commercial diesel fuel. Furthermore, it is specified that the emissions of nitrogen oxides for all the fuels analyzed were not corrected with the air humidity in aspiration. However, the results shown are congruent with each other. In this experimental activity, no particulate matter (PM) measurements were made due to its low concentration which does not allow a reliable measurement with a smoke meter conventional [16].

Figures 5–10 show the trend of the exhaust emissions in the case in which the engine was fueled with a blend of 20% and 50% biodiesel with diesel commercial for automotive (percentages by volume). The experimental results highlight a fairly similar behavior for the B20 mixture and diesel fuel [17]. However, there is from observing that even at 20% (B20) the NOx emissions are slightly higher and those CO lower, compared to a diesel with the standard calibration of the engine control unit as already observed for the case of pure biodiesel [18]. NOx emissions increase while those of CO decrease. The explanation of these results is to be found in the different chemical/physical characteristics of the fuels, in particular, in the different curves of distillation and the presence of an oxygen molecule in the chemical structure of the biodiesel [19]. These properties result in faster burning and local peaks of higher temperatures than diesel. To take advantage of lower CO emissions and better combustion of biodiesel, the standard calibration of the engine ECU has been modified to improve the level of NOx emissions [20].

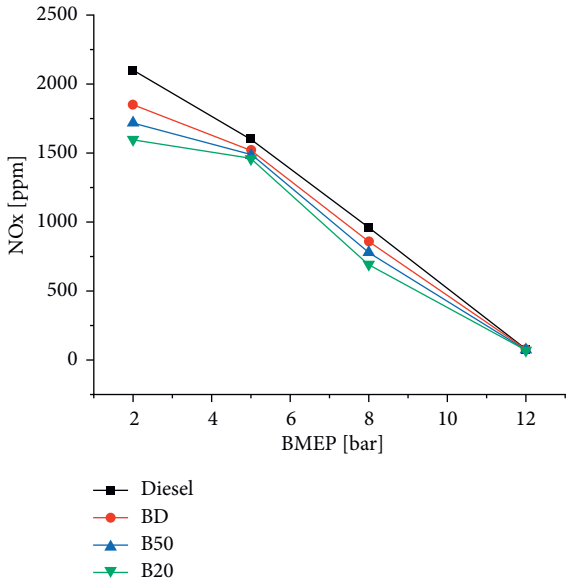

Figure 8: NOx emission with bmep @ 1500 rpm.

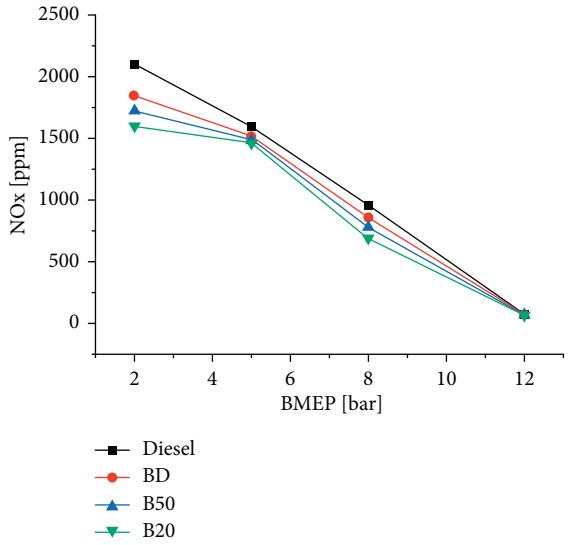

Figure 9: NOx emission with bmep @ 2000 rpm.

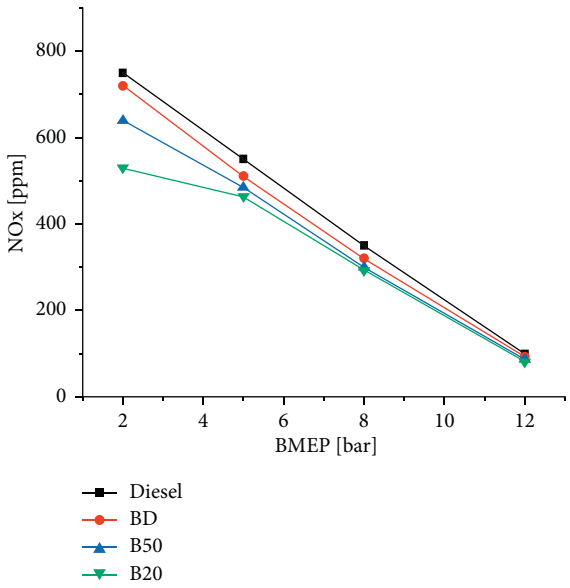

Figure 10: NOx emission with bmep @ 3000 rpm.

6. Conclusion

In recent years, biodiesel has aroused a lot of interest thanks to its biodegradability and the absence of sulfur, and its low environmental impact in terms of global warming due to carbon dioxide emissions. In this research work, we analyzed the state of the art of biodiesel and its applicability as a fuel in modern fast diesel engines. It has analyzed the performance and emissions of the latest common rail diesel engine generation fueled with pure biodiesel and with a blend of biodiesel and diesel then compared them with diesel to verify their applicability. The activity was then conducted on the optimization of the engine parameters managed by the engine control unit to improve the behavior of the engine which varies with the fuel used. Typically, a modern diesel engine is powered by biodiesel without any modification to the engine calibration. The emissions of nitrogen oxides increase as the concentration of carbon monoxide in the exhaust gas decreases. These results are due to the chemical characteristics of the biodiesel (presence of an oxygen molecule in the chemical structure) that make combustion faster but with very high local temperature peaks.

Abbreviations

CO: Carbon monoxide
EPA: Economics of biofuels
HC: Hydrocarbon
IPCC: International Panel on Climate Change
NOx: Nitrogen oxides
PM: Particulate matter.

Data Availability

The data used to support the findings of this study are included in the article.

Conflicts of Interest

The authors declare that they have no conflicts of interest.

References

[1] K. Velmurugan and A. Sathiyagnanam, "Impact of antioxidants on NOX emissions from a mango seed biodiesel-powered di diesel engine," *Alexandria Engineering Journal*, vol. 55, no. 1, pp. 715–722, 2016.

[2] V. Perumal and M. Ilangkumaran, "Experimental analysis of operating characteristics of a direct injection diesel engine fuelled with cleome viscosa biodiesel," *Fuel*, vol. 224, pp. 379–387, 2018.

[3] A. Purandaradas, T. Silambarasan, K. Murugan et al., "Development and quantification of biodiesel production from chicken feather meal as a cost-effective feedstock by using green technology," *Biochemistry and Biophysics Reports*, vol. 14, pp. 133–139, 2018.

[4] G. Vaidya, P. P. Patil, S. Arif Senol et al., "Chlorella protothecoides algae oil and its mixes with lower and higher alcohols and Al_2O_3 metal nanoadditives for reduction of pollution in a CI engine," *Journal of Nanomaterials*, vol. 2022, Article ID 9658212, 6 pages, 2022.

[5] P. Zhang, Y. Su, C. Yi et al., "Spray, atomization and combustion characteristics of oxygenated fuels in a constant volume bomb: a review," *Journal of Traffic and Transportation Engineering*, vol. 7, no. 3, pp. 282–297, 2020.

[6] K. A. Tripathi S& Subramanian and K. Subramanian, "Experimental investigation of utilization of soya soap stock-based acid oil biodiesel in an automotive compression ignition engine," *Applied Energy*, vol. 198, pp. 332–346, 2017.

[7] R. Surakasi, Y. S. Ratnakar, V. V. Prasanna Kumar, and M. Sairam, "Performance evaluation and emission characteristics of organic sunflower oil biodiesel using additives," *Design Engineering*, vol. 8, pp. 4968–4983, 2021.

[8] H. Saleh and M. Y. E. Selim, "Improving the performance and emission characteristics of a diesel engine fueled by jojoba methyl ester-diesel-ethanol ternary blends," *Fuel*, vol. 207, pp. 690–701, 2017.

[9] N. Acharya, N. Nanda, S. Panda, and S. Acharya, "Analysis of properties and estimation of optimum blending ratio of blended mahua biodiesel," *Engineering Science and Technology, An International Journal*, vol. 20, no. 2, pp. 511–517, 2017.

[10] A. K. Agarwal, A. Dhar, J. G. Gupta et al., "Effect of fuel injection pressure and injection timing of karanja biodiesel blends on fuel spray, engine performance, emissions and combustion characteristics," *Energy Conversion and Management*, vol. 91, pp. 302–314, 2015.

[11] J. Arunprasad, A. N. Krishna, D. Radha, M. Singh, R. Surakasi, and T. D. Gidebo, "Nanometal-based magnesium oxide nanoparticle with *C. vulgaris* algae biodiesel in diesel engine," *Journal of Nanomaterials*, vol. 2022, Article ID 1688505, 9 pages, 2022.

[12] A. K. Agarwal, A. Shrivastava, and R. K. Prasad, "Evaluation of toxic potential of particulates emitted from jatropha biodiesel fuelled engine," *Renewable Energy*, vol. 99, pp. 564–572, 2016.

[13] S. Al-lwayzy and T. Yusaf, "Diesel engine performance and exhaust gas emissions using microalgae chlorella protothecoides biodiesel," *Renewable Energy*, vol. 101, pp. 690–701, 2017.

[14] H. Chen, J. He, and X. Zhong, "Engine combustion and emission fuelled with natural gas: a review," *Journal of the Energy Institute*, vol. 92, no. 4, pp. 1123–1136, 2019.

[15] R. Surakasi, T. Choudhary, S. Bhattacharya et al., "Analysis of environmental emission neat diesel-biodiesel-algae oil-nanometal additives in compression ignition engines," *Journal of Nanomaterials*, vol. 2022, Article ID 3660233, 7 pages, 2022.

[16] Y. Guo, S. Stevanovic, P. Verma et al., "An experimental study of the role of biodiesel on the performance of diesel particulate filters," *Fuel*, vol. 247, pp. 67–76, 2019.

[17] A. Wierzbicka, P. T. Nilsson, J. Rissler et al., "Detailed diesel exhaust characteristics including particle surface area and lung deposited dose for better understanding of health effects in human chamber exposure studies," *Atmospheric Environment*, vol. 86, pp. 212–219, 2014.

[18] T. Xu-Guang, S. Hai-Lang, Q. Tao, F. Zhi-Qiang, and Y. Wen-Hui, "The impact of common rail system's control parameters on the performance of high-power diesel," *Energy Procedia*, vol. 16, pp. 2067–2072, 2012.

[19] S. Natarajan, K. A. Trasy, N. Srihari, and S. Raja, "Effects of injection timing on CI engine fuelled with algae oil blend with taguchi technique," *Energy Procedia*, vol. 105, pp. 1043–1050, 2017.

[20] B. Ashok, K. Nanthagopal, R. Thundil Karuppa Raj, J. Pradeep Bhasker, and D. Sakthi Vignesh, "Influence of injection timing and exhaust gas recirculation of a calophylluminophyllum methyl ester fuelled CI engine," *Fuel Processing Technology*, vol. 167, pp. 18–30, 2017.

Hindawi
Journal of Engineering
Volume 2022, Article ID 1293310, 5 pages
https://doi.org/10.1155/2022/1293310

Research Article

Liquid Fuels Derived from Microalgae: Physicochemical Analysis

Surakasi Raviteja[1] **and Velivela Lakshmikanth Chowdary**[2]

[1]*Department of Mechanical Engineering, Lendi Institute of Engineering and Technology, Jonnada, Vizianagaram, Andhra Pradesh, India*
[2]*Department of Mechanical Engineering, International Associate, Wolaita Sodo University, Sodo, Ethiopia*

Correspondence should be addressed to Velivela Lakshmikanth Chowdary; lucky.19862@gmail.com

Received 9 May 2022; Revised 29 May 2022; Accepted 31 May 2022; Published 14 June 2022

Academic Editor: Karthikeyan Sathasivam

In the analysis of the fuel like the liquid fuels obtained from the transesterification process of Spirulina microalgae biomass, the physicochemical characteristics correspond to fractions of gasoline, paraffin, and diesel, and to determine the environmental sustainability of its use, combustion tests were carried out on a diesel test engine (1000, 2000, and 3000 rpm) to establish a comparison with commercial neat diesel. The results obtained prove, based on the analysis of emissions and combustion, that this fuel can be a direct replacement for diesel.

1. Introduction

The environmental impact caused by waste cannot be easily recycled, making them unusable waste. Inadequate final disposal has a negative influence on environmental quality and human health. This planetary nature of the problem implies that universally approved international policies for gradual reductions in emissions into the atmosphere, as well as common support in anticipation of the large costs required to protect entire populations from the effects of climate change, are required [1]. The necessity to invest in alternative energy such as biofuels derived from crops such as sunflower, soybean, and rapeseed is thus emphasized, especially given the role they may play in achieving the reduction of greenhouse gas emissions. Agriculture's contribution helps us achieve the Kyoto Protocol's goals while lowering pollution levels. A million tonnes of biodiesel produced from domestic crops reduces hydrocarbon and polycyclic aromatic emissions by 80% and particulate matter and fine dust by 50%, respectively [2]. The IPCC (International Panel on Climate Change) identified CO_2 as one of the gases responsible for the greenhouse effect and human activity as one of the reasons in its first report in 1990. That human activity is behind the acceleration of the heating process and that only by drastically reducing greenhouse gas emissions in the atmosphere will it be possible to avoid exceeding the critical, dangerous thresholds even for the maintenance of life on earth has evolved [3]. The recent oil crisis, as well as public interest in environmental issues, has prompted further research into all renewable energy options. More and more sustainable energy sources, including biomass, are gaining popularity in the community. The latest official document presented by the EPA (Environmental Protection Agency) is intended to provide information to interested parties who want to evaluate the possibility of using biodiesel as a substitute for commercial automotive diesel. EPA is an agency of the United States federal government whose mission is to protect human and environmental health. The density of a substance is determined by its mass divided by its volume. When this index is higher, fuel will be more able to generate energy. The density of biodiesel fuel is greater than that of petroleum diesel, so it generates more power [4]. In the same way that gasoline's octane number specifies gasoline's combustibility and ignition characteristics, diesel fuel's cetane number (CN) shows diesel's [5]. The higher the cetane number, the better the combustion, and there is a correlation between it and ignition delay time [6]. Compounds are structurally defined by their cetane number. It is generally the case that the cetane

number increases as the chain length and unsaturation decrease in fatty acid esters.

2. Fuel Characterisation

The characterization of fuel consists of identifying its physical and chemical properties through various laboratory tests. It is important to know these parameters because the design of automotive fuel tanks, pumps, and lines is based on the physical and chemical properties of the fuel to be used, to avoid wear, evaporation losses, and pressure drops.

3. Combustion Test

The main combustion tests that an engine undergoes include exhaust emission and combustion process failures. Flue gas analysis consists of measuring the amount of pollutant gases emitted by the engine into the atmosphere. The following gases are typically analysed: emissions of nitrogen oxides (NOx and NO), carbon monoxide (CO), particulate matter, and opacity. The most important of which is the air emission standard from fixed combustion sources, which establishes the maximum permissible levels of gas emissions from the exhaust of internal combustion motorbikes [7]. Failures in the combustion process are necessary for the reliable and safe operation of machinery; the risk of faults and the time an engine is out of service can be reduced only if potential problems are anticipated and avoided. Therefore, one of the tools available for the analysis of failures in the combustion process is the analysis of the engine's performance.

4. Results and Discussion

4.1. Optimization of the Fuel. To establish the factors influencing the performance of the liquid fuel production process, the data given in Table 1 are checked for normal behaviour, which is a necessary condition for the application of the completely randomised design. For the use of this model, temperature is considered as an input factor and liquid volume is an output factor, and the result is a p value of 0.011, which is a value lower than 0.06 with a confidence level of 96%, which shows that the temperature variable has a significant influence on the experiment. Considering the pressure variable with FE, a p value of 0.69 is obtained, and with the residence time FE, the p value = 0.61; as can be seen, the values are greater than 0.05, which shows that they are not statistically significant and are therefore discarded from the experiment. In addition, polynomial regression is performed with the data given in Table 2 to identify the maximum point of the curve (Figure 1), and the optimum temperature (x-axis) is determined to obtain the highest liquid volume (y-axis). Based on fourth-degree polynomial regression, the following equation is obtained:

$$y = -1E - 2.8 + 0.0003 - 0.1356 + 14.9x - 1207. \quad (1)$$

Considering this equation, the maximum critical temperature point is calculated to be 377°C, which produces the highest volume of liquid fuel.

Table 1: Liquid fuel production process tests.

Temperature (°C)	Pressure (Psi)	Holding time (min)	Liquid volume (cm^3)
350	56	10	4.5
	16	10	4.7
	56	20	4.5
	16	20	4.8
460	56	10	4.2
	16	10	4.1
	56	20	4.4
	16	20	4.2

Table 2: Tests to determine greater fuel efficiency.

Temperature (°C)	Liquid volume (cm^3)
290	5.01
320	5.74
350	6.27
380	6.94
410	6.03

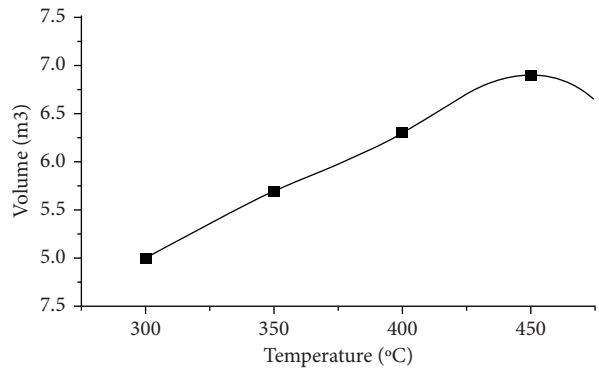

Figure 1: Temperature calibration curve.

4.2. Physicochemical Characterization. The physicochemical analysis of the liquid fuel obtained determined that it has characteristics typical of petroleum-based fuels. Table 3 provides the physicochemical properties of the algae fuel with ASTM standard. The algae fuel has the characteristic color and smell of petroleum products; the density and API gravity correspond to medium crude oil [8].

4.3. Characterisation of Polycyclic Aromatic Hydrocarbons. The gas chromatograph analysis shows that of the six PAHs analysed, the concentration results of which are given in Table 4, fluoranthene and benzo (a) pyrene are those found in the highest proportion in the chemical composition of the algae fuel; the volume percentage of the six PAHs analysed corresponds to 1.49% of the liquid fuel [9].

5. Comparison of the Combustion Process

The emissions of nitrogen oxides (NOx and NO), carbon monoxide (CO), particulate matter, and opacity are analysed, and to establish the failures in the combustion process,

Table 3: Physicochemical characteristics of the fuel obtained.

Parameter	Value
Density (g/cm^3)	0.88
Viscosity (centipoise)	1.11
Flashpoint (°C)	20.5
Freezing point (°C)	−39.3
Cetane number	46.7
Distillation temperature of 90% (°C)	320

Table 4: The concentration of PAHs in the fuel.

PAHs	Concentration	
	ppm	%
Fluoranthene	6090	0.62
Benzo (b) fluoranthene	442	0.05
Benzo (k) fluoranthene	0	0
Benzo (a) pyrene	4893	0.50
Indene pyrene	2100	0.22
Benzo perylene	1377	0.14
Total	14 902	1.5

noise and vibrations are analysed; this comparison is established at 00 rpm and 2000 rpm of the engine.

5.1. NOx, NO, and CO Gas Emissions. The test data at 1000 rpm show that commercial diesel emits 94% more NOx than algae fuel and 110% more NOx. The algae fuel emits 255% more CO than commercial diesel, as shown in Figure 2. With the data obtained from the measurements shown in Figure 2, we proceeded to transform them into units of the reference standard; the value obtained for NOx is 120 mg/m^3, which is less than the value established in the standard (2200 mg/m^3), and as for CO and NO emissions, there is no standard application. In the 2000 rpm test (Figure 2), the process fuel emits 98% more nitrogen oxide (NOx), 98% more nitrogen monoxide (NO), and 276% more carbon monoxide (CO) than commercial diesel [10]. With the data obtained from the measurements shown in Figure 2, we proceeded to transform them into the units of the reference standard; the value obtained for NOx is 120 mg/m^3, which is less than the value established in the standard (2350 mg/m^3), and as for CO and NO emissions, there is no standard application.

5.2. Particulate Matter Emission. For the particulate emission test, a comparison is made with commercial diesel at 1000 rpm and 2000 rpm, taking the measurements with the diesel exhaust gas tester [11]. Figure 3 shows the particulate concentration at 1000 rpm, and it is observed that the particulate emission of the algae fuel is 58.4% higher than that of diesel. Algae fuel compared to diesel at 2000 rpm, as shown in Figure 3, has a higher percentage of 46.3% than commercial diesel. According to the analysis of the fixed combustion sources in the maximum permissible limits of emissions to air for internal combustion engines, the fuel of the process at 1000 rpm is within the limits established for new sources, and at 2000 rpm, it exceeds the established value by 91.3%.

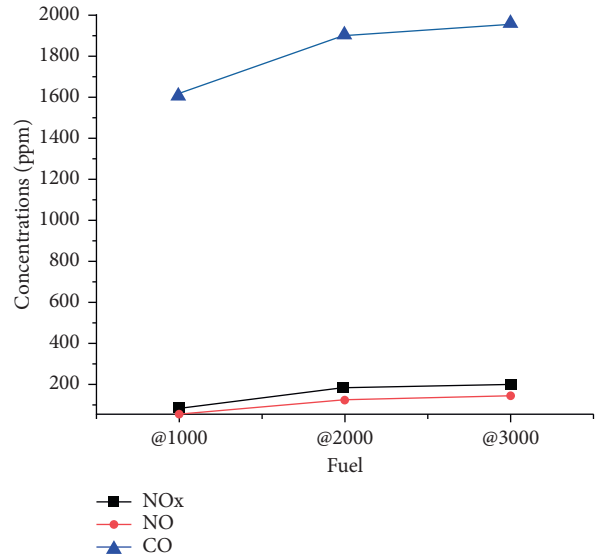

Figure 2: NOx, NO, and CO gas emissions.

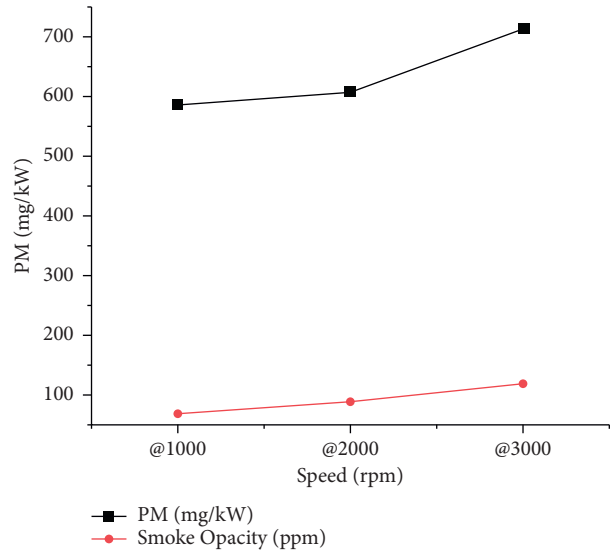

Figure 3: PM and smoke gas emissions.

In the results for smoke opacity, where diesel and algae fuel are compared, both are within the limits established by the ASTM standard. In the 1000 rpm tests, the opacity of the fuel obtained is 538% higher than the opacity of the diesel, as shown in Figure 3. For the 2000 rpm tests, the opacity of the fuel obtained is 2589% higher than the opacity of the diesel, as shown in Figure 3. For the opacity analyses, a diesel exhaust gas tester was used, which determines that the k-factor of the algae fuel is 0.13, equivalent to 1.4% opacity, which represents a higher index compared to the k-factor of diesel which is 0.022, equivalent to 0.3% opacity, for the data obtained at 1000 rpm. Likewise, for 2000 rpm, the k-factor is 3.77, which is equivalent to 37.7% opacity; therefore, it is a higher index compared to the diesel k-factor of 0.15 corresponding to 1.5% opacity [12].

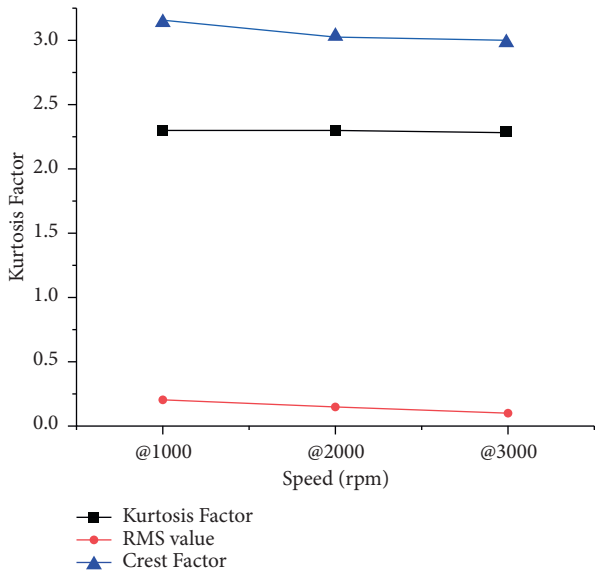

Figure 4: Combustion noise.

5.3. Combustion Noise. Figure 4 shows the kurtosis and crest factor values of the algae fuel, which are higher than those of diesel, thus leading to variations in the noise amplitude, while the RMS value showing the noise concentration at 1000 rpm is higher than those of diesel, which leads to variations in the noise amplitude, while the RMS value showing the noise concentration at 1000 rpm is higher than those of diesel [13]. In this case, the kurtosis factor and the crest factor of the algae fuel are lower than the diesel values, which means that there is no considerable variation in the noise amplitude, while the RMS value is higher for the fuel obtained, which means more energy contained in the noise and therefore more noise [14, 15], as shown in Figure 4.

6. Conclusions

After carrying out the gas and particle emissions tests, it was determined that the diesel had better combustion results, showing values well below the emissions of the algae fuel, which also shows an excessive generation of white smoke, a symptom of early combustion in the chamber. When comparing the combustion of algae fuel, it is established that in idling conditions at1000 rpm, the two fuels are within the maximum permissible limits of the Ecuadorian regulations for stationary combustion sources in the emission of NOx and particulates. In the combustion process, acceleration emissions at 3000 engine rpm are determined to be below the maximum permissible limits. The results of the failure of the combustion process are determined using noise and vibration analysis. In the tests at 1000 rpm, 2000 rpm, and 3000 rpm, it is determined that the engine presents more difficulties in the combustion process of the algae fuel in comparison with commercial diesel, finding greater noise and vibrations that generate high wear in the engine parts. Once the results have been analysed, it is shown that the sustainability of the transesterification process does not constitute a methodology for the management through the analysis of the combustion test in the diesel engine because the fuel obtained from the process has higher emissions of pollutants (CO, NO, NOx, particulates, and opacity) and combustion failures affecting the engine.

Data Availability

The data used to support the findings of this study are included within the article.

Conflicts of Interest

The authors declare that they have no conflicts of interest.

References

[1] P. R. Ganesh, K. H. Reddy, J. M. Babu, and M. S. Chandra, "Experimental investigation of performance, emission and combustion characteristics of a di-diesel engine fuelled with aqueous cerium oxide and aqueous aluminium oxide nanoparticle additives," in *Recent Trends in Mechanical Engineering*Springer, Berlin, Germany, 2021.

[2] G. Vaidya, P. P. Patil, S. E. N. E. R. Arif Senol et al., "Chlorella protothecoides algae oil and its mixes with lower and higher alcohols and Al2O3 metal nanoadditives for reduction of pollution in a CI engine," *Journal of Nanomaterials*, vol. 2022, Article ID 9658212, 6 pages, 2022.

[3] S. Manigandan, R. Sarweswaran, P. Booma Devi et al., "Comparative study of nanoadditives TiO2, CNT, Al2O3, CuO and CeO2 on reduction of diesel engine emission operating on hydrogen fuel blends," *Fuel*, vol. 262, Article ID 116336, 2020.

[4] C. V. P. Pascoal, A. L. L. Oliveira, D. D. Figueiredo, and J. C. C. Assunção, "Optimization and kinetic study of ultrasonic-mediated in situ transesterification for biodiesel production from the almonds of Syagrus cearensis," *Renewable Energy*, vol. 147, no. 1, pp. 1815–1824, 2020.

[5] M. R. Miladinović, D. N. Veljovi, J. B. Krsti, I. B. Bankovi, V. B. Veljkovi, and O. S. Stamenkovic, "Valorization of walnut shell ash as a catalyst for biodiesel production," *Renewable Energy*, vol. 147, no. 1, pp. 1033–1043, 2020.

[6] M. Sarno and E. Ponticorvo, "A new nanohybrid for electrocatalytic biodiesel production from waste Amalfi coast lemon seed oil," *Fuel*, vol. 267, no. 1, Article ID 117178, 2020.

[7] R. Surakasi, Y. S. Ratnakar, V. V. Prasanna Kumar, and M. Sairam, "Performance evaluation and emission characteristics of organic sunflower oil biodiesel using additives," *Design Engineering*, vol. 8, 2021.

[8] V. D. Raju, H. Venu, L. Subramani, and S. R. Reddy, "Comparative assessment of various nanoadditives on the characteristic diesel engine powered by novel tamarind seed-methyl ester blend," in *Recent Technologies for Enhancing Performance and Reducing Emissions in Diesel Engines*, pp. 138–158, IGI Global, 2020.

[9] S. Rathinam, J. B. Sajin, G. Subbiah, A. Rajeev, and S. Prakash, "Assessment of the emission characteristics of the diesel engine with nano-particle in neem biodiesel," *Energy Sources, Part A: Recovery, Utilization, and Environmental Effects*, vol. 42, no. 21, pp. 2623–2631, 2020.

[10] J. Arunprasad, A. N. Krishna, D. Radha, M. Singh, R. Surakasi, and T. D. Gidebo, "Nanometal-based magnesium oxide nanoparticle with *C. vulgaris* algae biodiesel in diesel engine,"

Journal of Nanomaterials, vol. 2022, Article ID 1688505, 9 pages, 2022.

[11] S. Vellaiyan, "Enhancement in combustion, performance, and emission characteristics of a biodiesel-fueled diesel engine by using water emulsion and nanoadditive," *Renewable Energy*, vol. 145, pp. 2108–2120, 2020.

[12] R. Surakasi, T. Choudhary, S. Bhattacharya et al., "Analysis of environmental emission neat diesel-biodiesel–algae oil-nanometal additives in compression ignition engines," *Journal of Nanomaterials*, vol. 2022, Article ID 3660233, 7 pages, 2022.

[13] M. Ramalingam, V. Ramasamy, S. Palanisamy, M. Subramaniam, and K. Muthusamy, "Experimental investigation on performance, combustion, and emission characteristics of diesel doped with green synthesized nano cerium oxide," *Environmental Progress and Sustainable Energy*, vol. 40, no. 2, 2020.

[14] P. Appavu and M. Venkata Ramanan, "Study of emission characteristics of a diesel engine using cerium oxide nanoparticle blended Pongamia methyl ester," *International Journal of Ambient Energy*, vol. 41, no. 5, pp. 524–527, 2020.

[15] Dr Raviteja and Vv Prasanna Kumar, "Performance and emission characteristics of sunflower oil bio diesel on four stroke diesel engine," *International Journal of Advanced Research in Engineering and Technology*, vol. 12, pp. 204–216, 2021.